

Model-scale Parametric Investigation of the Effects of Propeller Boss Cap Fins on the Hub Vortex and Open Water Efficiency in addition to a Controllable Pitch Propeller Study and a Full-scale Comparison.

Patricia Dam, Mikkel Jørgensen

AAU Energy, TEPE4-1000, 2023-6



Copyright © Aalborg University 2023

List of the main software used in this project:

InkScape:	For drawings and illustrations.
L ^A T _E X:	For typesetting the report, utilising the official template of Aalborg University.
MATLAB [®] :	For the making of plots and graph of the computational fluid dynamics attained.
STAR-CCM+:	For setting up, visualising and solving the computational fluid dynamics simulations.



AALBORG UNIVERSITY
STUDENT REPORT

AAU Energy
Aalborg University
Pontoppidanstræde 111
<http://www.aau.dk>

Title:

Model-scale Parametric Investigation of the Effects of Propeller Boss Cap Fins on the Hub Vortex and Open Water Efficiency in addition to a Controllable Pitch Propeller Study and a Full-scale Comparison.

Project Type:

Master's thesis

Project Period:

Spring Semester 2023

Project Group:

TEPE4-1000

Participants:

Patricia Dam
Mikkel Jørgensen

Supervisors:

Chungen Yin

Page Numbers: 92

Date of Completion:

June 2, 2023

Abstract:

In the transition to a carbon neutral future the reduction of CO_2 -emissions within the shipping industry is important as this industry accounts for $\approx 3\%$. One such way is through energy saving devices such as the propeller boss cap fins (PBCF), which in this report is numerically investigated with RANS simulations in open water and rudder conditions. The Q-criterion was used to visualise the PBCF's effect on the hub vortex.

A parametric model-scale study with the four PBCF parameters, chord length, height, pitch and rake was conducted based on a validated, grid independent simulation, which resulted in an 0.76 p.p. open water efficiency gain for the best case with a chord length of 9% propeller diameter.

The best case PBCF was used to explore the correlation with a controllable pitch propeller, that found gain in efficiency for a pitch-diameter ratio above 0.9.

The best case PBCF was also used for exploring the scaling effects between model- and full-scale simulations, which found a 1.71 p.p. gain in comparison with the model-scale simulation with an inclusion of the same PBCF.

The content of this report is freely available, but publication (with reference) may only be pursued due to agreement with the author.

Preface

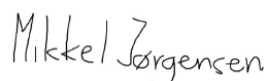
This report is the master's thesis written by Patricia Dam and Mikkel Jørgensen from the Thermal Energy and Process Engineering specialisation on the Energy Engineering masters study within the Faculty of Engineering and Science at Aalborg University with the collaboration of MAN Energy Solutions Frederikshavn. References throughout the report are cited using the Harvard format [author (s), year] and each source can be found in the Bibliography with the following order for citation: [Author(s)], [Title], [Publisher], [Edition], [Year], [Pages], [ISBN], [DOI], [URL], [date of access]. It is worth noting that some sources do not follow this format, as the information was not available. Equations, figures and tables are numbered in relation to the chapter which it appears in and the number of which it appears (chapter number, (Number of equation, figure or table in the chapter)). In the beginning of each chapter a small introduction to inform of the content is written. The report is meant to be read on a digital unit so that the reader can zoom on figures and tables to better visualise and understand results.

The authors thank MAN Energy Solutions for providing the opportunity, resources and guidance. Without the provided resources a report of this scope would be infeasible. A thank you is also extended to Chungeng Yin for sparing and support.

Aalborg University, June 2, 2023



Patricia Dam
<Patricia@familiendam.dk>



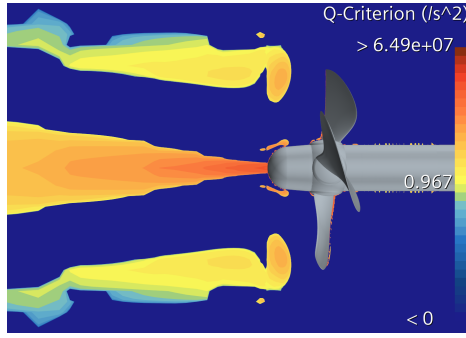
Mikkel Jørgensen
<mikkel.joergensen1997@hotmail.com>

Executive Summary

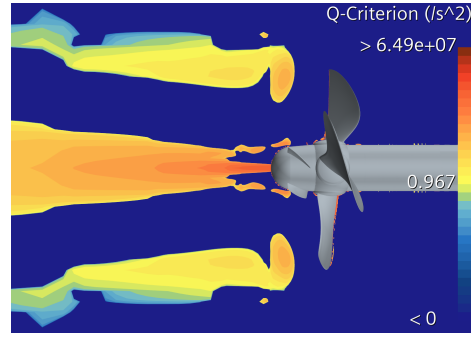
A literature study of Propeller Boss Cap Fins (PBCF) is conducted from which the presented theory is based upon. A total of three 3D steady-state RANS simulation models are constructed, where two are scale models of the propeller and the propeller with rudder-attachment, and the last is a full-scale simulation of the propeller. A quarter of the domain is computed in the case of the propeller simulations as periodic symmetry is applicable, which in turn is not applicable with the rudder-attachment. The models are deemed mesh independent and are validated against tank test data before investigations are commenced, to ensure valid results. The validations are done for both the γ - and γ - $Re_{\theta t}$ -transitions models where a performance difference between the two is noted in the rudder-attachment simulations.

Before the installation of PBCF a new hub is designed to make a larger continuous mounting surface, which also increases the open water efficiency marginally by 0.1-0.2 percentage points (p.p.) in model-scale.

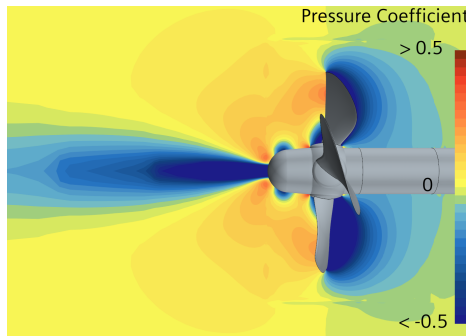
Single-parameter investigations are conducted for 4 PBCF variables: Pitch, rake, chord length and height whereafter 'Best Parameter values' PBCF is constructed based on the optimal individual parameters. The 'Best Parameter values' PBCF was found to perform worse than the optimal chord length ($9\% c/D_p$), with 0.65 and 0.76 p.p. respective gain in open water, and 0.51 and 0.60 p.p. gain respectively in the rudder implementation, suggesting adverse cross-combination effects within the parameters. Besides from the open water efficiency gain visual representations of the hub vortex are provided, using the Q-criterion, in effort to qualitatively state the individual parameters' diffusing effect on the hub vortex. Examples of such is presented in the figures below for a propeller with and without the best PBCF, where it is shown that the hub-vortex is narrower directly behind the hub and more diffused farther away downstream. Plots of the pressure distribution are also included to relate the hub vortex to the pressure distribution which determines the thrust and thus efficiency.



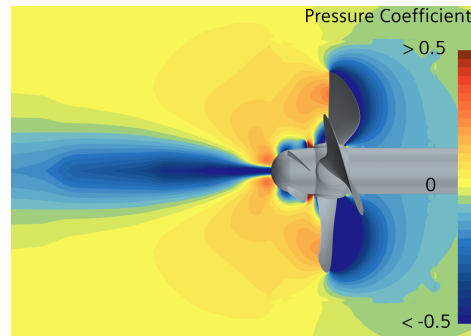
Q-criterion plot of propeller without PBCF in open water conditions.



Q-criterion plot of propeller with the best PBCF (9% c/D_p) in open water conditions.



Pressure coefficient scalar plot without PBCF in open water conditions.



Pressure coefficient scalar plot with the best PBCF (9% c/D_p) in open water conditions.

Afterwards, new investigations are conducted to examine the open water efficiency gain in the case of a controllable pitch propeller (CPP) as this information is of importance to designers and customers of CPPs. The optimum PBCF from the parameter study is used (i.e. a chord length of 9% c/D_p). The CPP-case is simulated for the actual range of the given propeller but also for a larger virtual range to enhance understanding and find the 'break even' points with respect to propeller pitch. It can be concluded that the PBCF are gaining efficiency across the operational range of the propeller and the virtual lower 'break even' pitch is between 0.8 and 0.9 P/D and no higher limit was found.

Finally, full-scale investigations of the propeller with and without the optimal PBCF are conducted to investigate the effect of model- vs. full-scale when it comes to the open water efficiency, the efficiency of a PBCF in full-scale and to highlight the scaling effects in general. It was found that the full-scale without PBCF accounted for an increase of 1.45 p.p. and the full-scale with PBCF was 1.32 times more efficient. Four effects of scaling were found in the full-scale visual representation using the Q-criterion. Those being a more narrow and less intense hub vortex, orderly layered tip vortices downstream, vortices above the tip of the propeller blades and less pronounced satellite vortices.

Nomenclature

Symbols	Description	Unit
c	Chord	[m]
D	Diameter	[m]
F	Force	[N]
h	Characteristic cell size	[m]
i	Rake	[°]
J	Advance ratio	[-]
K	Coefficient	[-]
k	Turbulent kinetic energy	[m ² /s ²]
N	Number of	[-]
n	Angular Velocity	[rps]
p	Pressure	[Pa]
P	Pitch	[m]
P	Apparent Order of Convergence	[-]
Q	Torque	[Nm]
R	Radius	[m]
r	Radius	[m]
rr	Refinement ratio	[-]
Re	Reynolds Number	[-]
s	Numerical Sign	[-]
T	Thrust	[N]
U/u	Velocity	[m/s]
V	Speed	[m/s]
V	Volume	[m ³]
Z	Number of propeller blades	[-]

Greek symbols	Description	Unit
α	Pitch angle	[°]
γ	Intermittency	[-]
ϵ	Solution difference	[-]
ε	Dissipation of Kinetic Energy	[m ² /s ³]
η	Efficiency	[-]
θ	Angle	[°]
κ	Camber	[m]
λ	Scaling factor	[-]
ϕ	'Parameter of interest'	
ρ	Density	[kg/m ³]
τ	Shear Stress	[Pa]
Ω	Vortex Tensor	[-]
ω	Specific Dissipation Rate	[s ⁻¹]

Subscripts	Description
A	Average on propeller plane
c	Coarse
cells	Cells
D	Drag
domain	of the domain
f	Fine
G	Generator
i	Current iteration
i-1	Previous iteration
L	Lift
M	Model-scale
m	Medium
nt	Chord and x-axis
Q	Torque
rms	Root Mean Square
S	Full-scale
s	Skew
T	Thrust
0	Open Water
θt	Momentum Thickness
∞	Surrounding
τ	Shear Friction

Superscripts	Description
<i>(a)</i>	Approximate
<i>(ext)</i>	Extrapolated

Acronyms	Description
CFD	Computational Fluid Dynamics
CPP	Controlable Pitch Propeller
EEDI	Energy Efficiency Design Index
ESD	Energy Saving Device
FPP	Fixed Pitch Propeller
GCI	Grid Convergence Index
IMO	International Maritime Organisation
PBCF	Propeller Boss Cap Fins
RANS	Reynolds-Averaged Navier-Stokes
SST	Shear Stress Transport

Contents

Preface	v
Executive Summary	vii
Nomenclature	ix
1 Introduction	1
1.1 Report Structure & Methods	1
1.2 Motivation	2
1.3 Literature Study	2
1.4 Current Market	6
1.5 Problem Statement	7
2 Theory	9
2.1 Construction of Ships	9
2.2 Propeller Geometry and Physics	10
2.3 Numerical Methodology	14
2.4 Vorticity, Drag & Lift	20
2.5 Meshing of the Computational Domain	23
3 Grid Independence Study	31

3.1	Grid Convergence Index	31
3.2	Mesh Generation	32
3.3	Grid Convergence Index Results	35
4	Validation	37
4.1	Open Water Simulations	37
4.2	Rudder Simulations	39
5	Pre Parametric Study	41
5.1	Hub-Alteration	41
5.2	Propeller Boss Cap Fins Mesh Refinement	45
5.3	Analysis of Computational Resources	47
5.4	Computational Domain	49
6	Parametric Study	53
6.1	Parameter-Simulation Variables	53
6.2	Workflow of the Parametric Study	55
6.3	General Simulation Setup	56
6.4	Efficiency Gain and Vorticity Results	57
6.5	Best Performing Propeller Boss Cap Fins	69
6.6	Inflow Analysis of Propeller Boss Cap Fins	72
7	Controllable Pitch Propeller Study	73
7.1	Propeller Pitch	73
8	Full-scale Studies	79
8.1	Simulation Flow & Mesh Parameters	79
8.2	Full-scale Efficiency Gain	81

Contents	xv
8.3 Full-scale Observations and Effects	82
9 Discussion	85
10 Conclusion	89
11 Future Work	91
Bibliography	93
A Mesh & Residuals Analysis	97
A.1 Open Water	97
A.2 With Rudder	103
B PBCF geometry	109

Chapter 1

Introduction

1.1 Report Structure & Methods

This report strive to complete three main tasks, a parametric investigation of a PBCF, influence on the PBCF when the propeller pitches and scaling effects between model- and full-scale simulations. To do this the report begins with a motivation and literature study to set the foundation of why this is relevant and what previous studies have found in terms of PBCF geometries and the best testing methods for these. From this the problem statement is stated based on the knowledge gained. Following is an in-depth explanation of propeller theory and the applied numerical methods. Then an investigation of the mesh is presented followed by a grid independence study. To validate the simulation results they were compared to tank model scale data from MAN Energy Solutions Frederikshavn for both an open water and rudder test. This also included an investigation regarding the transition models γ - and γ - $Re_{\theta t}$. Following the validation four smaller studies regarding the hub geometry, PBCF refinement, computational resources and the computational domain for the open water simulation are conducted to make the foundation for the parametric study. The parametric study is a single parameter study that focus on four variations in the geometry of a PBCF. These variations are the chord length, height of the PBCF, pitch and rake. The study concluded with a most efficient PBCF being identified through efficiency gains and the effects on vorticity from the Q-criterion plots. The most efficient PBCF is then utilised for a variable propeller pitch study that evaluated the PBCF at the propeller operational points, with varied pitch and ships speed and a constant ships speed with varied pitch. Subsequently, a full-scale simulation based on the model-scale simulation is

made to evaluate the changes between model- and full-scale in regards to the hub alteration and most efficient PBCF. Lastly, the results are discussed and concluded upon and suggested future studies based on this report are presented.

1.2 Motivation

As the world moves towards a carbon neutral future, improvements to major existing industries are crucial. One of such industries is the transport industry that supply goods across the globe, placing it as one of the corner stones in the green transition. Within transport, shipping amounts to around 90% of the transport goods and is responsible of approximately 3% of the worlds CO₂-emissions,(International Marine Organisation). Therefore, the International Maritime Organisation (IMO), responsible for regulating security and safety within the international shipping trade, introduced the Energy Efficiency Design Index (EEDI). The EEDI is a calculation method for which the overall energy efficiency of the vessel can be estimated. Limiters to the EEDI are set in place by the IMO to ensure that vessels move towards lower fuel consumption and emissions. The limiters are set to be tightened every 5 years, the most recent outlining a 30% reduction of emissions from the 2000-2010 average, for vessels above a gross tonnage of 400.

As the EEDI is binding within international waters, the application of energy saving devices (ESD) are of high interest world wide. ESD are usually located around the propeller region where they are used to reduce drag, increase thrust or shape the flow going into or leaving the propeller, thereby increasing the propulsive efficiency. (Dang et al., 2012).

1.3 Literature Study

In 1988 one of the first in a series of papers about the PBCF was published by Ouchi et al. (1988). The paper investigated the influence of the PBCF geometry on the open water efficiency, through experimental data and visual representations. Experiments were conducted using the reverse open water method, proposed in the paper. This method took the well-established open water test and reversed it. By placing the propeller behind the hull, the hub vortex and the inflow to the propeller were realistic. From the visualisations of the experiments, the PBCF showed a direct dampening effect on the vortex and thereby increased the efficiency. The investigated PBCF parameters were the height and installation angle for different advance ratios. It found that if the radius of the PBCF was larger than 33% or

smaller than 15% of the propeller, the implementation reduced the overall efficiency. The installation angle, similarly to the height, should not be below -20° or above 30° in relation to the shaft. In a following paper by Ouchi et al. (1989) a summation of the forces that act on the propeller and the interactions with the PBCF was explained, together with cavitation and scaling evaluations. The paper found that the torque and thrust coefficients could be decomposed into specific propeller coefficients and PBCF coefficients, summarised becoming the total coefficient. The calculation for the coefficients was as follows, together with the open water efficiency and advance ratio formulation:

$$K_T = \frac{T}{\rho n^2 D^4} \quad (1.1)$$

$$K_Q = \frac{Q}{\rho n^2 D^5} \quad (1.2)$$

$$\eta_0 = \frac{J}{2\pi} \frac{K_T}{K_Q} \quad (1.3)$$

$$J = \frac{V_A}{nD} \quad (1.4)$$

From experimental tests, the paper Ouchi et al. (1989) found that the PBCF decreased the hub vortex and eliminated the cavitation associated with it. Lastly, it discussed real test performance of the PBCF and the scaling effects that should to be accounted for. Here it also noted that the conditions for the PBCF heavily influenced the performance, with the efficiency gain on one ship ranging from 1.2% to 4.5%. Scaling was said to be difficult as boundary layers and the local velocities do not scale uniformly. The paper also estimates that model efficiency gain can be multiplied by 2-3 to find the full-scale gain. In both Ouchi et al. (1988) and Ouchi et al. (1989) the results were based on model tank test data, using both the reverse open water and the self-propulsion test.

These methods of testing were utilised in Nojiri et al. (2011) together with a computational fluid dynamics (CFD) study. The paper tested three sets of PBCF, each set having a different number of fins, 4, 5 and 6, but the same geometric variations. The individual sets were the tested with a propeller that had blade numbers corresponding to the number of fins. It found that for a 5-bladed propeller PBCF pair, either rectangular shaped or a trailing edge cut type saw the largest efficiency gain. The torque had decreased and thrust increased. Increased PBCF height introduced additional thrust and torque, making it only slightly better than the control. For the computational part, it focused on the 5-bladed propeller where clear improvements to the hub vortex was found. These simulations used the SST $k-\omega$ model turbulence model which, according to Nojiri et al. (2011), is a commonly

used model for dealing with wing profiles with flow-separation.

Kawamura et al. (2013) also used this CFD method to investigate the results achieved in Ouchi et al. (1988) against a sea trial from Hansen et al. (2011). From the CFD simulations, efficiency increases between 1.48 and 2.05 % were found, which did not correspond with the sea trial results of the Hansen et al. (2011) of 4%. The report also investigated the effects of scaling that showed a smaller efficiency gain in model-scale than full-scale, as discussed in Ouchi et al. (1988). Furthermore, it concluded that the model-scale overestimates the fin drag while underestimating the hub drag reduction. Mizzi et al. (2017) utilised two rounds of optimisation algorithms for 120 iterations and CFD in model- and full-scale to optimise the PBCF parameters height, chord length, thickness and pitch, resulting in an efficiency gain of 1.3 %. For the CFD, SST $k-\omega$ and Reynolds-averaged Navier-Stokes (RANS) were used for a cylindrical domain with approximately 10 million cells. Lim et al. (2014) did a 3D parametric study on the PBCF parameters suggested by Ouchi et al. (1988): height, installation and inclination angle. The study was done on a 6 bladed propeller, for a 6,000 TEU (twenty-foot equivalent unit) container ship. By using RANS, SST $k-\omega$, a cylindrical domain, and analysis of variance (ANOVA) the report concluded that height and installation angle had the largest impact on the efficiency, whereas the inclination angle was almost irrelevant. The report also investigated a diverging hub against a converging hub, which is the most common, and found that the diverging hub performed worse. Cai et al. (2013) used another optimisation algorithm, to optimise a PBCF for a propeller that already had a PBCF implemented so that performance data was available. By using the algorithm the paper's PBCF achieved a larger efficiency gain than the already installed PBCF and concludes that optimisation algorithms are well suited for PBCF designing.

Another parametric study was conducted by Rosenvinge and Sandland (2021), which looked into the height, installation angle, chord length, rake angle, circumference and axial position, camber, camber position and thickness in addition to the number of fins. The optimal number of fins was found to match that of the propeller and was simulated for a rectangular NACA-profile. A deviation from the study from Ouchi et al. (1988) was that the height of the fin did not find an optimum around 20-25% relative radius of the propeller but at 30%. Axial and circumferential position showed the largest impact with gains of 0.5% and 1% respectively, whereas camber position, chord length, rake angle and thickness gained less than 0.2%. Building on this study, by utilising the optimum values, was Dam and Jørgensen (2022) that did a multi-variable parametric study of the shape, skew and pitch. It found that backwards skew has a large negative influence on the efficiency, the pitch should match that of the propeller at the hub and the shape should be more rectangular, which was in line with what was found in (Nojiri

et al., 2011). Another way of testing a propeller is through a self-propulsion test, this test includes the wake from the hull and in (Dang et al., 2012) concluded that the PBCF gave a 2.13% increase. To create an overview of the findings in the literature study the following two tables in regard to CFD practices and geometry investigations are presented.

Table 1.1: Parameters from the literature study relating to the CFD. Blank spaces indicate no available information. **Nothing more was specified.*

	Turbulence model	N_{cells}	Wall treatment	Vol. before propeller	Vol. after propeller	Domain	Radius	y^+
Dam and Jørgensen (2022)	SST k- ω	$17 \cdot 10^6$	all y^+	$3D_P$	$6D_P$	Cylinder	$4D_P$	0.013-4.7
Kawamura et al. (2013)	SST k- ω	$13 \cdot 10^5$				Single blade		
Lim et al. (2014)	SST*			$2D_P$	$4D_P$	Cylinder		
Mizzi et al. (2017)	SST k- ω	$10 \cdot 10^6$	all y^+	$2D_P$	$5D_P$	Cylinder	$3D_P$	Model scale 0-5.5 Full scale 0-160
Nojiri et al. (2011)	SST k- ω	$40 \cdot 10^4$						
Rosenvinge and Sandland (2021)	SST k- ω	$17 \cdot 10^6$	all y^+	$3D_P$	$6D_P$	Cylinder	$4D_P$	0-1.5

Table 1.2: Parameters from the literature study relating to the PBCF. Blank spaces indicate no available information.

	Z	Mean pitch [°]	r/R_P	Thickness	Length [m]	Inclination [°]
Cai et al. (2013)	3	46-49	0.28			
Dam and Jørgensen (2022)	4	48-58	0.3			
Dang et al. (2012)	4					
Kawamura et al. (2013)	5					
Lim et al. (2014)		61.5-71.5	0.28-0.31			± 10
Mizzi et al. (2017)		34-38	0.183-0.226	$0.0005D_P$ - $0.01D_P$	$0.0525D_P$ - $0.105D_P$	
Nojiri et al. (2011)	3-5					
Ouchi et al. (1988)	4	55-66	0.22-0.25			
Rosenvinge and Sandland (2021)	4	42-64		$0.025D_P$		30

	Circumferential installation distance	Installation distance x-axis	Chord length	Camber	Efficiency gain [%]
Cai et al. (2013)					2.9-4.1
Dam and Jørgensen (2022)	$0.0417D_P$	$0.0375D_P$	$0.09 D_P$		0.4-1.71
Dang et al. (2012)					2.13-6.03
Kawamura et al. (2013)					1.48-1.73
Lim et al. (2014)					2.1
Mizzi et al. (2017)				1.3	
Nojiri et al. (2011)					1.5
Ouchi et al. (1988)	$0.045D_P$ - $0.05D_P$	$0.0045D_P$ - $0.032D_P$			2-2.5
Rosenvinge and Sandland (2021)	$0.0417D_P$	$0.0375D_P$	$0.125D_P$	$0.017D_P$	1.043

1.4 Current Market

In the literature study, the PBCF show great promise backed by both simulation and trial data. It is therefore of interest to see how this translates to the commercial sector. In the following table, some of the most renowned producers are mentioned:

Table 1.3: Collection of PBCF's on the market with stated efficiency increases due to fuels saving, propeller type which it is designed for and the blade type. Blank spaces indicate no available information. *Fixed Pitch Propeller (FPP) and Controllable Pitch Propeller (CPP).

Manufacturer	Model Name	Stated Efficiency Improvement	Propeller Type	PBCF Blade Type
DMPC				
Fountom	PBCF	$\approx 5\%$		Small propeller blade design.
MOL Techno-Trade, Ltd	PBCF	Up to 5%		Round, flat and symmetrical.
Nakashima				
Tongzhou		3%-8%		
Wärtsilä	EnergoproFin	Up to 5%	FPP+CPP*	

As a caveat it is worth noting that efficiency gains stated by the companies do not explicitly state how they were calculated.

1.5 Problem Statement

Through the knowledge procured in the literature study in section 1.3 a direction for the study could be set. From the knowledge it was evident that there are areas within propeller and PBCF development which could benefit from more research, in order to make more educated design choices.

The first area identified concerns the PBCF and its parameters' influence on efficiency based namely on the thrust and torque which do not focus on the hub vortex that is the phenomena found in the literature study as being a main contributor to lower efficiencies.

The second area is the sole focus on FPPs which naturally does not look into the performance span of PBCF on CPPs.

Finally, the third area identified is the lack of full-scale simulations as it is uncertain which information is lost and to what degree it is lost in model-scale.

The problem statement based on these areas are given as follows:

Quantify and if possible qualitatively identify the influence of the four PBCF parameters chord length, height, pitch and rake on the hub vortex through Q-criterion representations and open water efficiency calculations. Utilising the most efficient PBCF elaborate on the open water efficiency effect of introducing a PBCF on a CPP. Lastly, evaluate the difference between model- and full-scale CFD simulations with and without PBCF, focusing on efficiency gains and vortex structures.

The PBCF are constructed as real propeller blades in comparison to the literature which commonly investigate rectangular NACA-profiles.

Chapter 2

Theory

In this chapter relevant theory is presented. At first an introduction to the general construction of a ship is given followed by an explanation of propeller geometries and the physics. Numerical methodologies with offset in the methods presented in the literature study are then presented whereafter physical parameters are presented in the form of vorticity, drag and lift. Finally, the meshing of the computational domain is presented with guidelines and the generation and evaluation of a mesh.

2.1 Construction of Ships

Ships and their designs vary greatly depending on the type and application. As eluded to in the motivation, the focus of this study is on transport vessels and more specific the transport of cargo in containers. A brief description of a 'general' container ship is thus presented, (Dam and Jørgensen, 2022). The main sections and components of a container ship are the:

- Hull
- Superstructure with the Bridge
- Stern & stem
- Motor, gearbox, shaft
- Propeller & rudder
- Bulbous bow
- Foredeck & -castle
- Exhaust piping

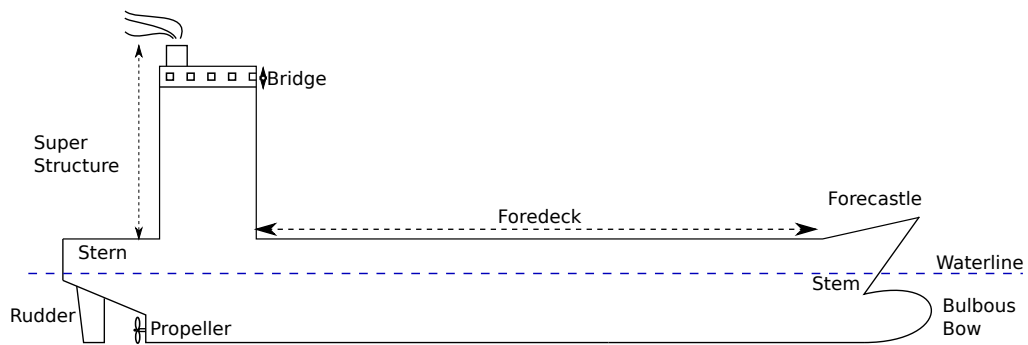


Figure 2.1: Illustration of container ship and it's main sections and components.(Dam and Jørgensen, 2022).

The hull of the ship is the outer shell containing the internal components shielding them from the surrounding elements and essentially keeping the ship afloat. The technical terms for the back and front end are stern and stem, respectively. At the stem the forecastle is situated and directly beneath the bulbous bow is found which' purpose is to increase the hydrodynamic performance. The superstructure, housing the bridge from where the view is optimal for navigation, is typically situated near the stern, but the position may vary from ship to ship. Between the superstructure and the forecastle the foredeck spans and this is where the majority of the cargo will be stacked. Finally, the propeller(s) driven by the engine(s) through gearing propels the ship with the aid of a rudder directing the thrust for manoeuvrability.

2.2 Propeller Geometry and Physics

The propeller is the final part in the drive train that propels the vessel. A propeller typically consist of 3-5 propeller blades that are either moulded together with the shaft or mounted on the latter part of the shaft in the hub region in front of the concluding hub-cap, also called the Boss cap, illustrated in figure 2.2. The individual blades are mounted to the shaft at the blade-foot where a flange ensures a stable mounting with the use of bolts. From the foot, the blade protrudes radially and is essentially made from infinitely many curved 2D-aerofoils stacked upon each other to construct the complex 3D-geometry. The pitch of the blades vary as the radius increases to maintain an optimum angle of attack as the local blade speed increases with increasing radial position, giving the blade the distinctive 'twisted' appearance.

On the upstream side of the blade, the water accelerates to greater velocity than on the downstream side giving a static pressure differential acting on the blade-area thus producing thrust. The upstream side is referred to as the suction side and downstream side is referred to as the pressure side alluding to the lower and higher pressure coefficients, respectively.

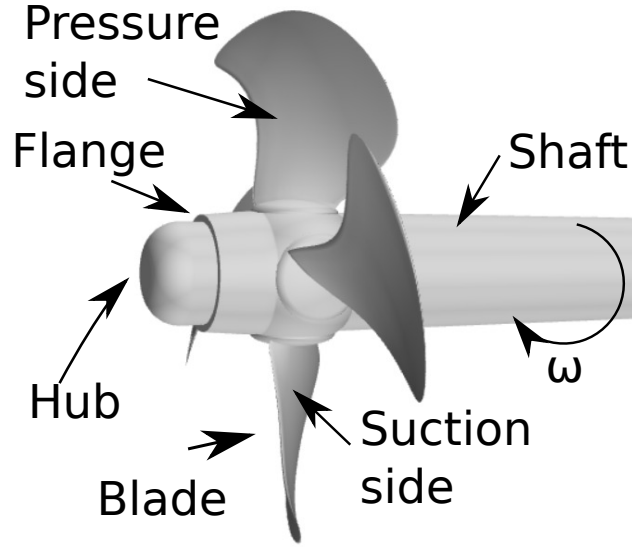


Figure 2.2: Illustration of a propeller and its components.

Aside from pitch, other important blade parameters include camber, skew and rake, and these are commonly expressed as functions of the dimensionless radial position $x = r/R$ and nominal values are often provided for $x = 0.7$.

A brief explanation of the 4 parameters is given beneath:

- **Pitch** describes the advance of the propeller in the course of a full revolution and is the angle between the x-axis (parallel to the shaft) and the chord of the profile. In this case the pitch refers to the mean pitch of the propeller. The formulation of pitch as a function of radius is presented below in equation (2.1) and visually represented in figure 2.3.

$$\alpha(r) = \tan^{-1} \left(\frac{P}{2\pi r} \right) \quad (2.1)$$

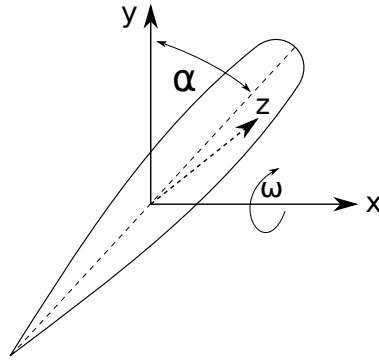


Figure 2.3: Illustration of pitch-angle α .

- **Camber** essentially describes the curvature of the profile and is often expressed as the ratio of the maximum normal distance between the camber and chord to the length of chord. In figure 2.4 the camber is distance denoted by the Greek letter kappa κ .

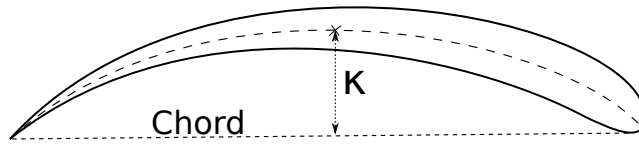


Figure 2.4: Illustration of camber κ .

The camber-chord ratio can now be defined:

$$\kappa_{\text{ratio}} = \frac{\kappa}{c} \quad (2.2)$$

- **Skew** is the distance from the mid-chord to the directrix at any given non-dimensional radial distance x . The directrix is the line perpendicular to the x -axis going through the mid-chord of the blade-foot. Skew is often given as the skew-angle θ_s , and an example of this is given in figure 2.5 for $x=1$. In general, skew can be balanced or biased where a balanced skew indicates that the distribution of the mid-chord is evenly forwards and backwards of the directrix and a biased skew indicates that the mid-chord is predominately forwards or backwards of the directrix. The skew illustrated in figure 2.5 is biased backwards skew i.e. the blade is said to be 'skewed back'. It should be noted the terms balanced and biased are loosely defined and are only descriptive. The skew distribution enables designers to effectively shorten/lengthen the local chord seen by the flow to increase/decrease the specific loading. Balanced skew is illustrated in figure 2.6.

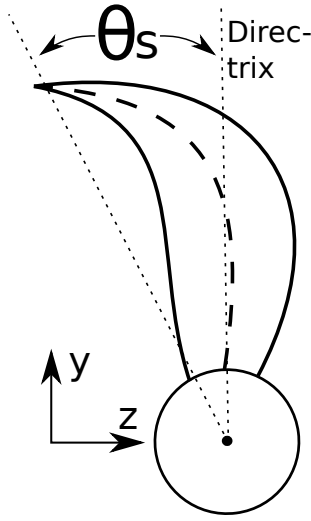


Figure 2.5: Illustration of biased backwards skew for the distance between the mid-chord line and the directrix at $x=1$ expressed by the skew-angle θ_s .

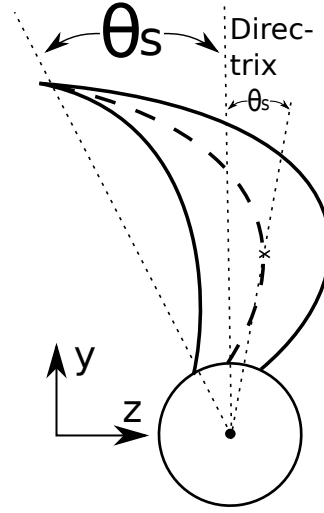


Figure 2.6: Illustration of balanced skew. Now two skew angles appear - one in front of the directrix at $x \approx 0.5$ and one behind at $x=1$, resulting in an even distribution.

- **Rake** is situated on the x - z plane projected by the shaft and the directrix and is comprised of two components - skew-induced and generator line rake.

$$i_{tot}(r) = i_s(r) + i_G(r) \quad (2.3)$$

Generator line rake is the distance, parallel to the x -axis, from the directrix to the generator line at a certain radius r . The generator line is the interception point between the pitch and x - z -plane which is projected by the directrix and x -axis. Skew-induced rake is then the additional distance skew introduces to the rake, which is from the generator line to the mid-chord. Skew-induced rake is more prevalent than generator line rake as $r/R \rightarrow 1$, and is calculated as follows:

$$i_s = r\theta_s \tan(\theta_{nt}) \quad (2.4)$$

In the following figure 2.7 the two types of rake are illustrated on a blade.

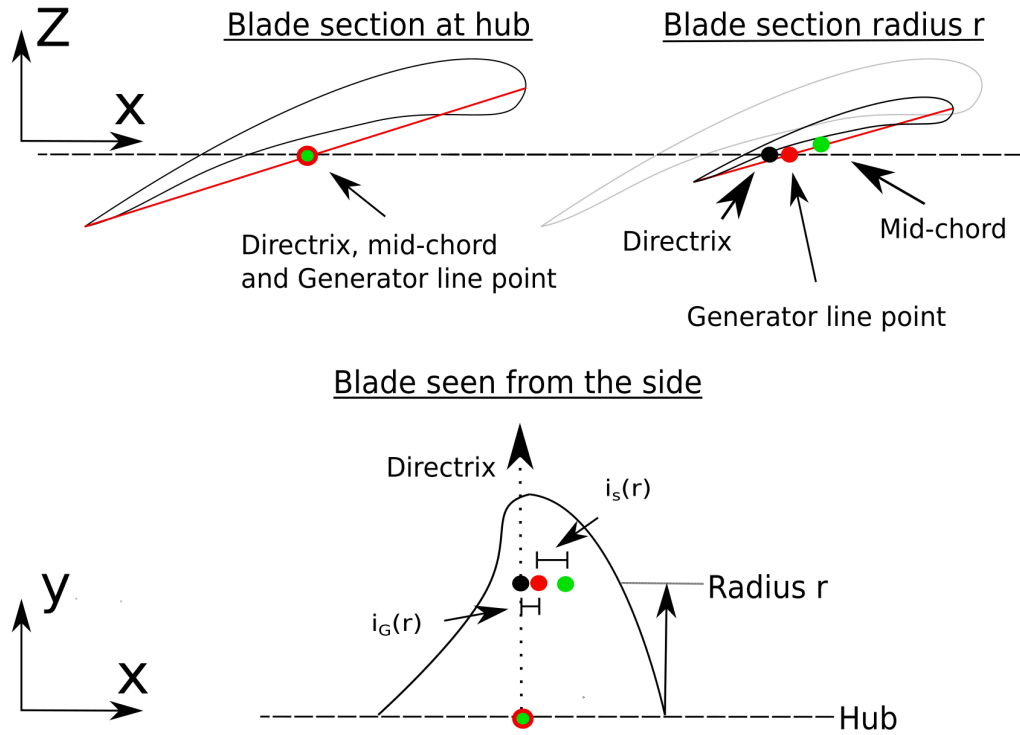


Figure 2.7: Rake illustration. The top two images are in the x - y -plane, and bottom image in the x - z -plane, where the x -axis is parallel to the shaft and the height of the blade is in the direction of the y -axis. The dotted line in the x -direction is the plane projected by the directrix and shaft axis. In the top left most image the directrix (black dot), mid-chord (green dot) and generator line point (red dot) all intersect at the same point on the projected plane. On the right most image however, as the blade section changed radius, only the directrix and generator line point intercept the projected plane. On the bottom image the propeller blade, sliced using the projected plane, is illustrated with the corresponding directrix, mid-chord and generator line points. Here the length of the generator rake ($i_G(r)$) and skew induced rake ($i_s(r)$) are also included.

2.3 Numerical Methodology

Based on the findings in the literature study in section 1.3 the main steps of the numerical methodology will be presented, with focus on the RANS equations together with the SST (Menter) k - ω turbulence model which is the predominant combination in the found literature. Finally, the choice of solvers and the ensuring of converged solutions is touched upon.

2.3.1 Navier-Stokes Equations

The Navier-Stokes equations are a set of governing partial differential equations describing the relation between the pressure and velocity of a viscous fluid i.e. the flow. In equations (2.5) and (2.6) the set of equations are presented for an incompressible, isothermal and Newtonian fluid.

The continuity equation governs the conservation of mass:

$$\nabla \cdot \mathbf{U} = 0 \quad (2.5)$$

And the momentum equations relate the pressure and velocity-components of the fluid:

$$\frac{\partial \mathbf{U}}{\partial t} + \nabla \cdot (\mathbf{U} \otimes \mathbf{U}) = -\nabla \left(\frac{p}{\rho} \right) + \nabla \cdot \left(\nu \cdot \nabla (\mathbf{U}) \right) + \frac{\mathbf{S}}{\rho} \quad (2.6)$$

The vector \mathbf{U} is a 3-dimensional vector containing the velocity-components u , v and w and the vector \mathbf{S} contains the 3 source terms: s_x , s_y and s_z . The pressure is denoted with the scalar p and the fluid properties with scalars ρ and ν for the fluid density and kinematic viscosity, respectively. (Versteeg and Malalasekera, 2007).

2.3.2 Reynolds-averaged Navier-Stokes Equations

The Navier-Stokes equations presented in the subsection 2.3.1 above governs the instantaneous values and thus account for every turbulent flow. However, resolving the turbulence requires a considerable amount of algebra and computational power and is often not of importance in practical applications. Instead, the instantaneous velocity and pressure are subjected to Reynolds decomposition replacing the flow variables with the sum of a mean and fluctuating component, to investigate the fluctuations' effect on the mean flow. The Reynolds decomposition of the flow variables are shown in equation (2.7) where the capital letter denotes the mean component and the apostrophe denotes the fluctuating component. (Versteeg and Malalasekera, 2007).

$$\mathbf{u} = \mathbf{U} + \mathbf{u}' \quad u = U + u' \quad v = V + v' \quad w = W + w' \quad p = P + p' \quad (2.7)$$

The continuity equation remain unchanged by the Reynolds decomposition evident from the commutative property:

$$\nabla \cdot \mathbf{U} = 0 \quad (2.8)$$

The momentum equations are changed evident from the fact that Reynolds stresses appear, exemplified in the x-momentum equation, in equation (2.9):

$$\frac{\partial U}{\partial t} + \nabla \cdot (U\mathbf{U}) = -\frac{1}{\rho} \frac{\partial P}{\partial x} + \nabla \cdot (\nu \cdot \nabla(U)) + \frac{1}{\rho} \nabla \cdot \underbrace{(-\rho \overline{u' \mathbf{u}'})}_{\text{Reynolds stresses}} + \frac{S_x}{\rho} \quad (2.9)$$

The Reynolds stresses are associated with the convective momentum transfer by turbulent eddies and involve products of fluctuating velocities. They can be expressed as proposed by Boussinesq, (Versteeg and Malalasekera, 2007):

$$\tau_{ij} = -\rho \overline{u'_i u'_j} = 2\mu_t S_{ij} - \frac{2}{3}\rho k \delta \quad \text{where:} \quad \delta = \begin{cases} 1 & \text{if } i = j \\ 0 & \text{if } i \neq j \end{cases} \quad (2.10)$$

with:

$$\mu_t = \rho \frac{k}{\omega} \quad (2.11)$$

The Reynolds stresses introduces new unknowns to the set of equation and thus two-equation turbulence models with transport equations for k and ω are necessary to introduce to close the system.

2.3.3 Menter Shear-Stress Transport k - ω Turbulence Model

The two-equation turbulence model of choice for simulations of PBCF is the Menter Shear-Stress Transport (SST) k - ω turbulence model in accordance to the literature study in section 1.3. The additional two transport equations compute the turbulent kinetic energy k and the specific dissipation rate ω used to close the system of equations.

In the paper Menter (1994), Menter developed the SST k - ω model on the basis that the previous available models had their 'shortcomings' in resolving the flow properly in both the near-wall region dominated by viscous forces and in the momentum-dominated free-stream. The underlying problem with the classic two-equations models is their inability to determine the onset and amount of separation in adverse gradient flows.

The k - ω is preferable in the near-wall region within the sub-layer and logarithmic region as it has no dependency on damping functions. This means it can simply be implemented with a Dirichlet boundary condition - the simplicity is superior in terms of numerical stability. A disadvantage of the k - ω model is the sensitivity to free-stream values of the specific dissipation rate ω_f , which also Kok states.

This disadvantage led Menter to include the k- ϵ model in the wake region and free-stream as it is insensitive to values of ω_f . Adding the Wilcox k- ω and a transformed k- ϵ model Menter (1994) proposed a Baseline model (BSL) where the two models are blended with a function F_1 .

The BSL reduces to the original k- ω for $F_1=1$ which is the case in the inner layers of the boundary layer. In the wake-region the two models are blended as $0 < F_1 < 1$, and outside the wake-region $F_1=0$ reducing the BSL to the transformed k- ϵ model. The transport equations of k and ω for the BSL are:

$$\frac{D(\rho k)}{Dt} = \tau_{ij} \frac{\partial u_i}{\partial x_j} - \beta^* \rho \omega k + \frac{\partial}{\partial x_j} \left((\mu + \mu_t \sigma_k) \frac{\partial k}{\partial x_j} \right) \quad (2.12)$$

$$\begin{aligned} \frac{D(\rho \omega)}{Dt} = & \frac{\gamma}{v_t} \tau_{ij} \frac{\partial u_i}{\partial x_j} - \beta \rho \omega^2 + \frac{\partial}{\partial x_j} \left((\mu + \mu_t \sigma_\omega) \frac{\partial \omega}{\partial x_j} \right) \\ & + 2(1 - F_1) \rho \sigma_{\omega 2} \frac{1}{\omega} \frac{\partial k}{\partial x_j} \frac{\partial \omega}{\partial x_j} \end{aligned} \quad (2.13)$$

The blending function F_1 is also used to blend the constants of the two models constituting the BSL:

$$\phi = F_1 \phi_1 + (1 - F_1) \phi_2 \quad (2.14)$$

The BSL overestimates the turbulent shear-stress τ and therefore a viscosity limiter is introduced giving the formulation of the Menter Shear-Stress Turbulence model when using equations (2.12) and (2.13) of the BSL, (Menter, 1994):

$$v_t = \frac{a_1 k}{\max(a_1 \omega, \Omega F_2)} \quad (2.15)$$

2.3.4 γ - & γ - $\text{Re}_{\theta t}$ Transition Models

A transition model with true predictability is a requirement in CFD-simulations of high quality as the transition from laminar to turbulent regime affects the overall solution. In this study two viable options were available in the simulation software: The γ - and γ - $\text{Re}_{\theta t}$ transition models.

The intermittency γ expresses the time-percentage a specific location is turbulent and the momentum thickness Reynolds number $\text{Re}_{\theta t}$ is used to predict the location/onset of the turbulence.

The transport equations for γ and $\text{Re}_{\theta t}$ are as follow:

$$\frac{d(\rho \gamma)}{dt} + \nabla \cdot \rho \gamma \bar{\mathbf{v}} = \nabla \cdot \left(\left(\mu + \frac{\mu_t}{\sigma_f} \right) \cdot \nabla \gamma \right) + P_\gamma - E_\gamma \quad (2.16)$$

$$\frac{d(\overline{\rho Re_{\theta t}})}{dt} + \nabla \cdot (\overline{\rho Re_{\theta t}} \bar{\mathbf{v}}) = \nabla \cdot (\sigma_{\theta t} (\mu + \mu_t) \cdot \nabla \overline{Re_{\theta t}}) + P_{\theta t} \quad (2.17)$$

The P- and E-terms are production and destruction terms respectively.

With the transition models it is possible to make accurate blending functions used in turbulence models e.g. the Menter SST $k-\omega$ turbulence model with good representation of the mean flow.

2.3.5 Numerical Flow Solvers

The Navier-Stokes equations and derivatives thereof, transport equations in general and associated models are partial differential equations which for complex 3D-geometries are practically impossible to solve analytically. The flow variables, e.g the velocity components of \mathbf{U} and the pressure p and so forth, must be solved numerically in an iterative process using known or assumed boundary conditions and a 'guesstimate' of initial conditions in the flow field.

Two steady state solvers are available in this study: The segregated flow solver and the coupled flow solver. The segregated flow solver uses a predictor-corrector method where the momentum and continuity equations are solved sequentially and the velocity field is pressure-corrected to fulfill the continuity equation. The solver uses the SIMPLE algorithm and can be of 1st or 2nd order.

The coupled flow solver solves the momentum and continuity equations simultaneously in a vector of equations, hence the coupling of the equations. The coupled equations can be solved using explicit or implicit time-integration schemes.

From simulations Rosenvinge and Sandland (2021) found that the 1st order segregated flow solver performed best in replicating the experimental data in these types of simulation of ship's propellers, whereas the coupled flow solver had poor convergence and needed considerably more iterations to settle resulting in longer simulation times, adversely affecting productivity.

2.3.6 Convergence

Convergence is paramount as the simulation results are products of numerical schemes and initial guesses.

Convergence is typically monitored from global values of the flow variable residuals and the physical values such as thrust, torque, drag and lift etc. The convergence is perfect when all flow variables' residuals have values of machine epsilon, this is however not realistic.

The global root mean square residual is determined by equation (2.18) and is typically plotted as a function of iterations for the flow variables such as the momentum, pressure, kinetic turbulent energy and specific dissipation rate, after a normalisation is performed.

$$R_{\text{rms}} = \sqrt{\frac{1}{N} \sum_{i=1}^N r_i^2} \quad (2.18)$$

The normalised residual that is presented is calculated:

$$R_{\text{pres}} = \frac{R_{\text{rms}}}{R_{\text{norm}}} \quad (2.19)$$

with the normalisation residual being the numerically greatest value of the first m iterations, with m being determined by the user. In this study the default value of $m=5$ is used for the number of iterations as this gives acceptable values for plotting.

$$R_{\text{norm}} = \mathbf{max} \{|R_1|, |R_2|, \dots, |R_m|\} \quad (2.20)$$

Once the change in the normalised global residuals have stabilised and settled around a constant value, preferably below $1 \cdot 10^{-3}$, the variable in question is considered converged.

The physical parameters must also converge to a stable value and are essentially more important than the residuals as these are not necessarily directly related to the physical parameters, as for instance the intermittency γ . An example of this where the simulation converges steadily for the physical parameters as in figures 2.8 and 2.9, and some of the residuals displayed in figure 2.10 still oscillate:

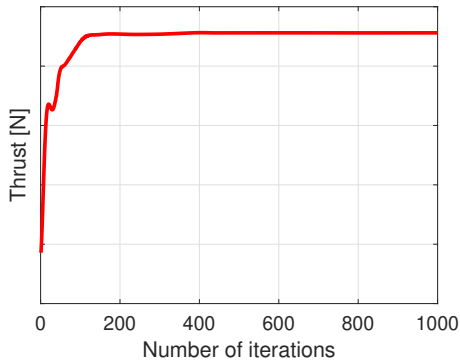


Figure 2.8: Thrust progression.

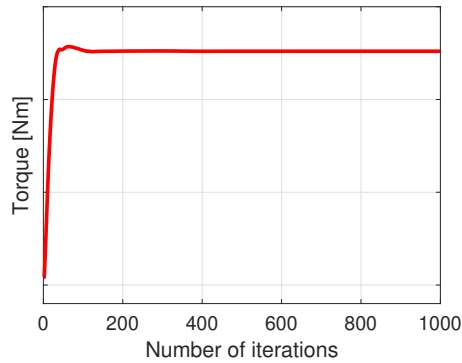


Figure 2.9: Torque progression.

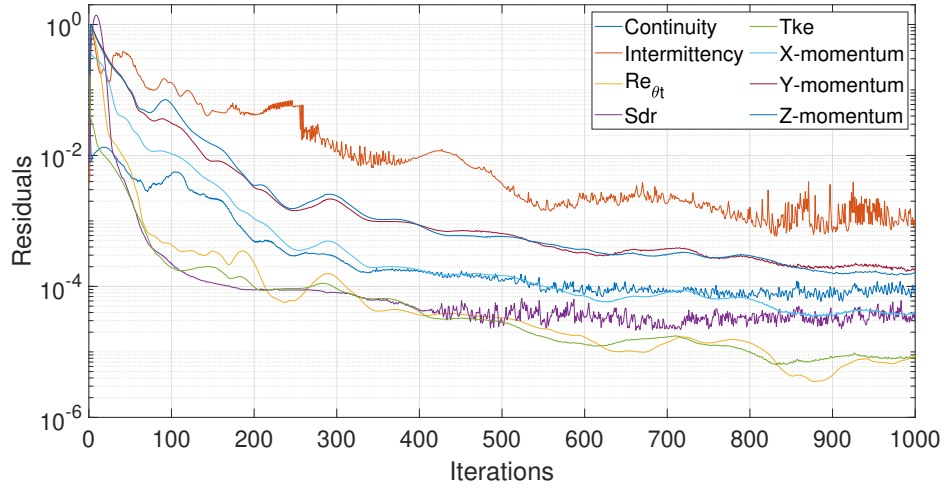


Figure 2.10: Residual plot for the X-, Y- and Z-momentum, continuity, intermittency, momentum thickness turbulent Reynolds number ($Re_{\theta t}$), specific dissipation rate (Sdr) and turbulent kinetic energy (Tke).

2.4 Vorticity, Drag & Lift

To assess the changes in the flow and performances of the PBCF the vorticity is a parameter of interest as this relates to the vortices. Furthermore, the effect of PBCF can be further investigated by looking into the combination of lift and drag to better understand the mechanism in play.

2.4.1 Vorticity - The Q-criterion

In order to visualise and quantify the flow in the vicinity of the propeller a way of determining the vorticity is needed. This enables direct comparison between different PBCF configurations with respect to their vortex-weakening effects and thus increase in open water propulsive efficiency.

A way of identifying and quantifying vorticity in CFD-simulations is to calculate the Q-criterion based on the velocity gradients and strain rates. It is formulated as follows with units of s^{-2} :

$$Q = \frac{1}{2} (||\Omega||^2 - ||S||^2) = -\frac{1}{2} \frac{\partial u_i}{\partial x_j} \frac{\partial u_j}{\partial x_i} \quad (2.21)$$

Where the anti-symmetric vortex tensor Ω and the symmetric strain rate tensor are as follows:

$$\Omega = \frac{1}{2} \left(\frac{\partial u_i}{\partial x_j} - \frac{\partial u_j}{\partial x_i} \right) \quad (2.22)$$

$$\mathbf{S} = \frac{1}{2} \left(\frac{\partial u_i}{\partial x_j} + \frac{\partial u_j}{\partial x_i} \right) \quad (2.23)$$

The velocity gradient tensor is defined:

$$\frac{\partial u_i}{\partial x_j} = \mathbf{S} + \Omega \quad (2.24)$$

A vortex exist if Q is of positive and non-zero value, otherwise conversely, as suggested by equation (2.21). The value of Q represents the strength of the vortex as it calculates the energy in unit quality and space making it a suitable parameter for investigation of flow of rotational nature or with re-circulation. As the range of Q is substantially large it should be presented in a logarithmic scale, (Gao et al., 2019). In the following figure 2.11 this graphical representation is presented.

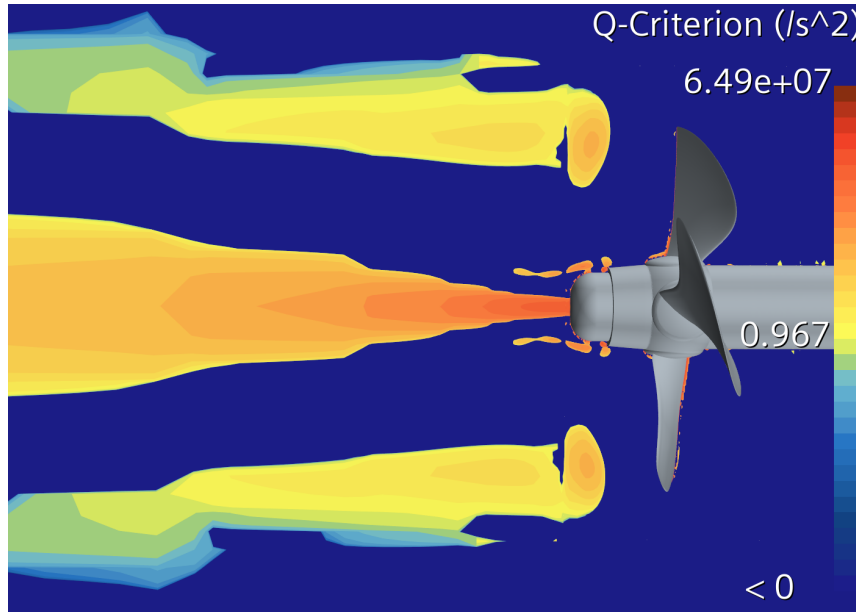


Figure 2.11: Logarithmic Q -criterion between 0 and $6.49 \cdot 10^7 \text{ s}^{-2}$.

2.4.2 Drag & Lift

As touched upon in section 2.2 propeller blades are analogous to aerofoils. Based on aerofoils a brief introduction to lift and drag is given.

The objective of an aerofoil is to produce lift by redirecting the incoming flow in two different path creating accelerated and decelerated flow on either side. The difference in velocity results in a pressure difference acting on the surface of the foil creating the lift-force. The lift comes with drag in form of pressure, shear and induced drag.

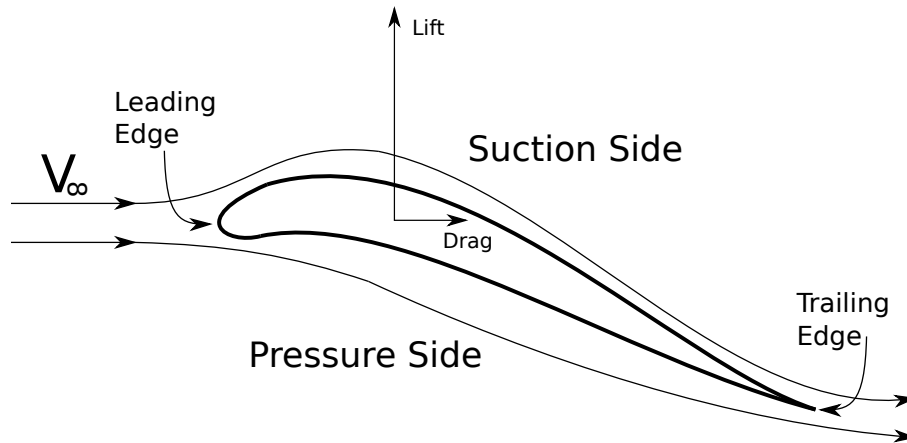


Figure 2.12: Illustration of the flow around an aerofoil.

Along a streamline the Bernoulli equation is valid meaning the sum of pressures is constant which is presented in equation (2.25) with the hydrostatic pressure term neglected.

$$c = p + \rho \frac{V^2}{2} \quad (2.25)$$

From this it is evident that the streamline with the greatest velocity has the lowest static pressure and vice versa given they originate from the same conditions. The lift and drag forces of aerofoils are proportional to the free-stream values of the fluid density, velocity and the planform area, (Cengel et al., 2016):

$$F_L \propto \frac{1}{2} \rho_{\infty} A_n V_{\infty}^2 \text{ and } F_D \propto \frac{1}{2} \rho_{\infty} A_n V_{\infty}^2 \quad (2.26)$$

Induced drag is associated with the loss of energy by the formation of vortices and fluctuations. At the tip a vortex is shed due to fluid spill-over from the high-pressure side to the low-pressure side and vortices are formed at the trailing edge where the two flows rejoin.

In the case of high-performance propellers the low pressure on the pressure side and the tip-vortex will to some extent produce vapour bobbles as the static pressure is locally lower than the vapour pressure of water. This inevitably leads to cavitation as the bobbles implode which is potentially damaging to the propeller and may cause noise issues.

2.5 Meshing of the Computational Domain

In order to implement the Navier-Stokes equations described in section 2.3 a computation domain surrounding the chosen geometry is required. As presented in the literature study this can be done in two ways using: a quarter domain or a full cylindrical domain. The quarter domain relies on periodical planes that reintroduce the flow into the other side of the domain utilising cell face values. The cylindrical domain encapsulates the entire propeller and a significant part of the down and up stream. The domain ranges from 2-3 propeller diameters upstream of the propeller reference line to 4-6 downstream with a radius of either 3 or 4. Separating the mesh into an outer and inner mesh allows for the utilisation of moving reference frame (MRF) or sliding mesh approach (SMA) to introduce rotation for the propeller. MRF numerically rotates the inner domain and creates a steady state solution, thereby making it less time consuming than the SMA which rotates both the mesh and geometry (Kellett et al., 2013). An investigation of the two domain types can be found in section 5.4. The size of the inner mesh, in contrast to the outer domain, is not well documented in literature. Examples of a cylindrical and quarter domain are illustrated on the following figures:

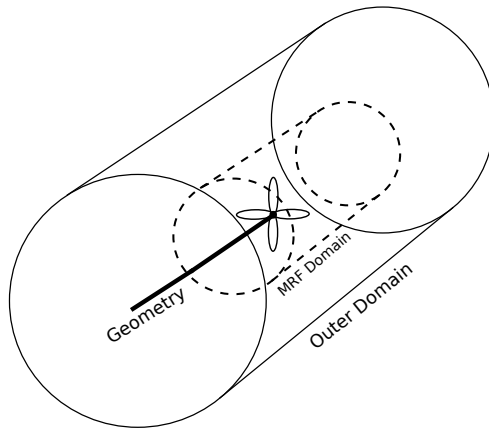


Figure 2.13: Illustration of a full cylindrical domain with an inner and outer region encapsulating a 4-bladed propeller and shaft.

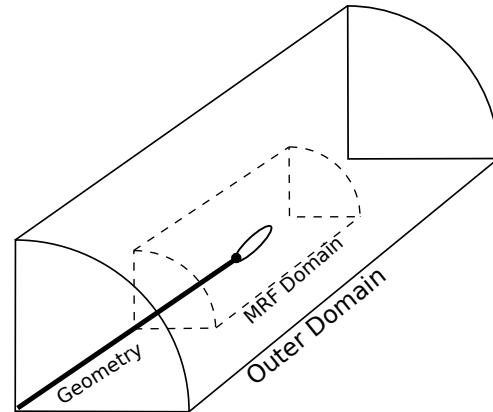


Figure 2.14: Illustration of a quarter cylindrical domain with an inner and outer region encapsulating a quarter of a 4-bladed propeller and shaft.

2.5.1 Quality Guidelines

To ensure that the simulation attain a satisfactory level of accuracy adhering to the established quality guidelines when creating a mesh is recommendable as they facilitate good retainment and transfer of information. Most guidelines focus on 2-dimensional meshes and are difficult to translate directly into 3D, some of those that are translatable are as follows:

- **Cell skewness angle**
- **Cell volume change**
- **Gridlines**

Cell skewness angle refer to the orthogonality of a mesh, in other words how similarly shaped two adjacent cell are. It is calculated as the angle between the normal to the centre point of the interlocked face and the vector connecting the centre point of the cells. This is illustrated in the figure 2.15 below. In a fully orthogonal mesh this value is 0 as the cells would be uniformly shaped and placed. If the skewness angle is above an 85° angle, it is considered a bad cell and would carry a larger risk of the quantities within becoming unbound. In the case of a skewness angle of 90° or greater, additional convergence issues arise.

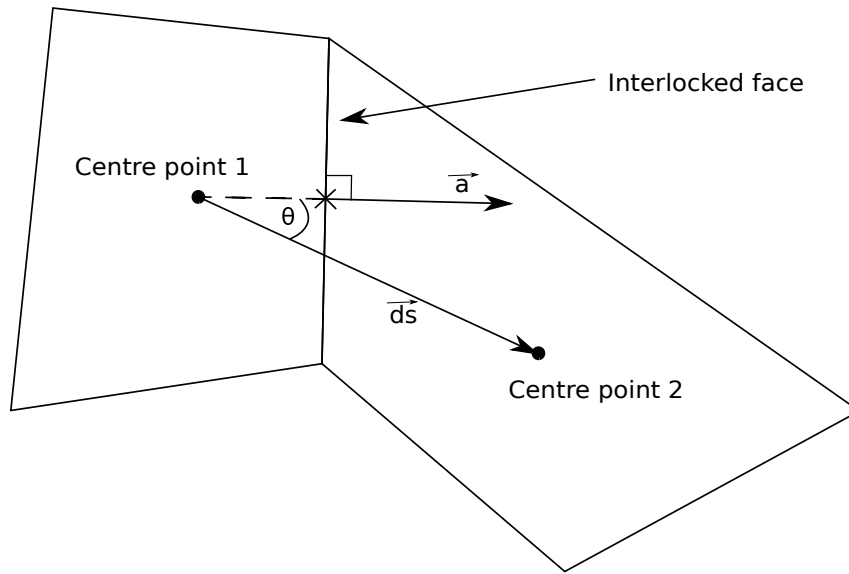


Figure 2.15: Illustration of the cell skewness angle θ .

Cell volume change is the volume ratio between adjacent cells. If adjacent cells have a value close or equal to 1, these cells are of similar or the same volume. Cells with a value of $1 \cdot 10^{-2}$ or below are bad cells and are likely to introduce additional inaccuracies and instability. Below is an example of both a good and bad cell in figures 2.16 and 2.17 respectively.

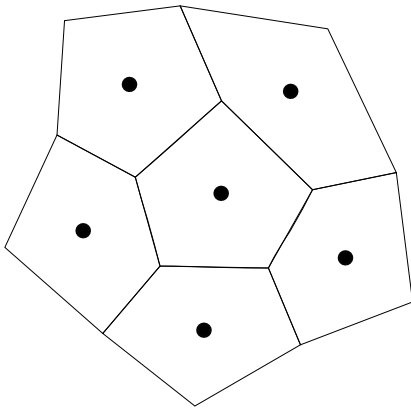


Figure 2.16: Illustration of good cell volume changes as the cells are of similar size.

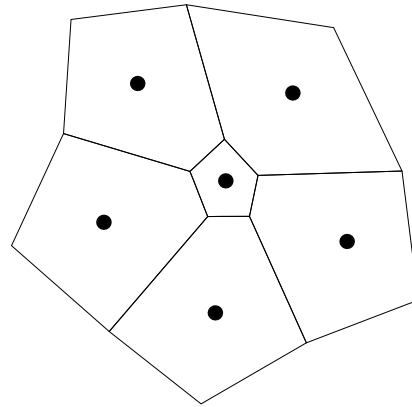


Figure 2.17: Illustration of bad cell volume changes as there is a large difference in cell volume. The drawing is not to scale.

Gridlines refer to the direction of the bulk flow and the orientation of the cells. By aligning the bulk flow and orientation false diffusion is less likely, and this alignment can be interpreted visually as in figures 2.18 and 2.19. However, this alignment can become difficult on the surface of geometries, so it is mostly general practise for the bulk flow. On the surface, thinner and longer cells are required to capture the boundary layer effects.

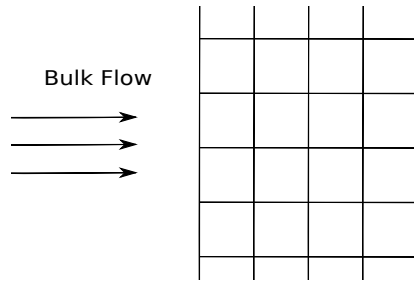


Figure 2.18: Gridlines aligned with the bulk flow.

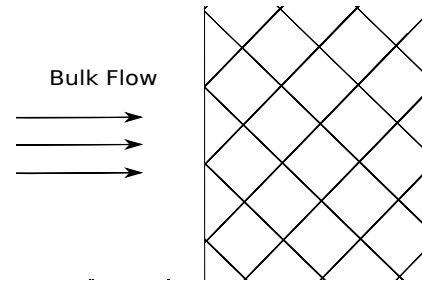


Figure 2.19: Gridlines not aligned with the bulk flow.

2.5.2 Meshing process

In Star-CCM+ two automatic meshing tools are available, the parts-based meshing and the region-based meshing. Parts-based meshing utilises geometry parts and curves to create additional refinement, whereas the Region-based meshing refines specified regions and boundaries in the mesh, independent of the geometry. Both methods refer to a base cell size, from which other levels of refinement are derived, and a set of meshing models. The meshing models apply to the entire domain with different base cell size differs. Commonly used models are the following:

- **Trimmed mesher**
- **Surface remesher**
- **Prism layer mesher**

The **trimmed mesher** lay the foundation of the mesh by dividing the domain into hexahedrals. The size of these hexahedrals depend on the chosen growth rate, base cell size and vicinity to the surface. Close to the surface the smallest cells are located to capture the boundary layer. Growth rate relates to the amount of cells in a refinement layer, of which the trimmed mesher in Star-CCM+ has four settings 1, 2, 4 or 8, these settings are as presented on figures 2.20, 2.21, 2.22 and

2.23 below. Cells adjacent to the wall are then trimmed, by creating polyhedras on the surface, to allow for a better representation of the surface. The mesh is therefor predominantly hexahedral yielding a low cell skewness and is independent of the surface refinement.

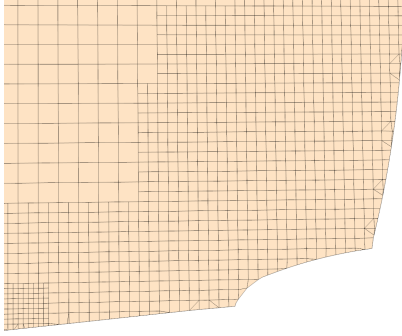


Figure 2.20: Illustration of a very slow growth rate with 8 cells per layer.

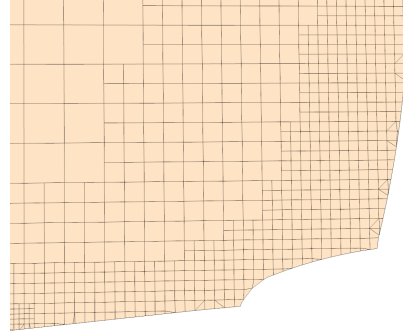


Figure 2.21: Illustration of a slow growth rate with 4 cells per layer.

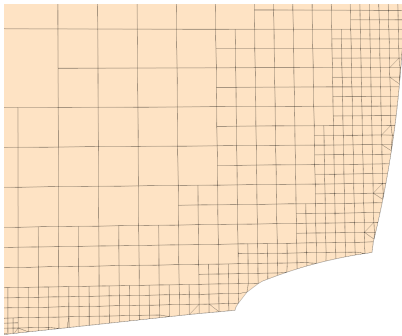


Figure 2.22: Illustration of a medium growth rate with 2 cells per layer.

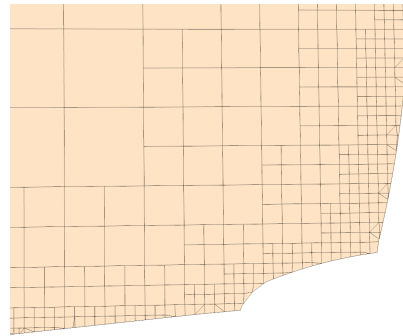


Figure 2.23: Illustration of a fast growth rate with 1 cell per layer.

Surface remesher, which is often recommended in combination with the trimmed mesher, re-triangulates the surface mesh in order to properly represent the geometry. The additional accuracy gained through this method depend on the chosen inputs and is particularly good at representing curvatures and edges. This is illustrated on figures 2.24 and 2.25.

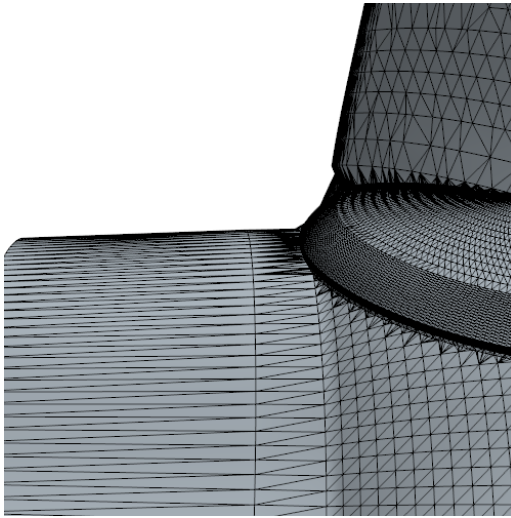


Figure 2.24: Original surface mesh.

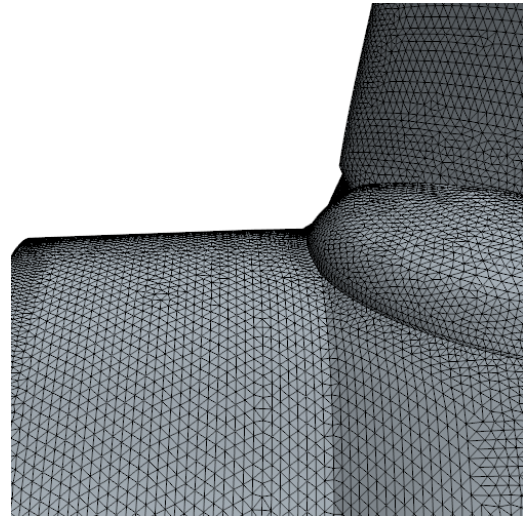


Figure 2.25: Remeshed surface mesh.

Lastly, the **prism layer mesher** restructures the volume cells situated closest to the surface. It creates orthogonal prismatic cell in order to capture the boundary layer effects, in particular that of the sub-layers. This prismatic layer is therefor defined by the thickness, growth rate and width of the cells. In figure 2.26 and 2.27 the difference between a mesh with and without the prism layer are displayed. A limitation of the mesher is that on the interface between the prismatic layer and regular trimmed mesh the cell growth is not bound potentially leading to large cell size changes and subsequent instabilities.

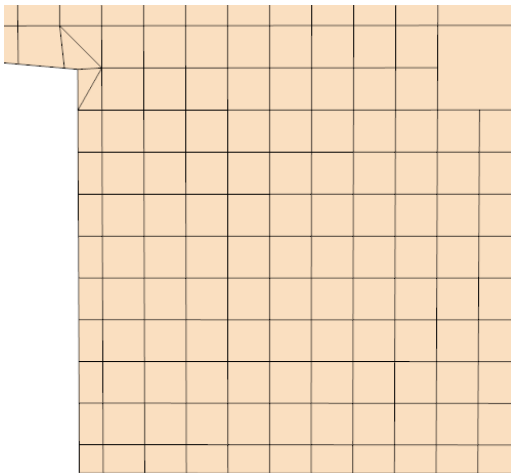


Figure 2.26: Volume mesh without a prism layer

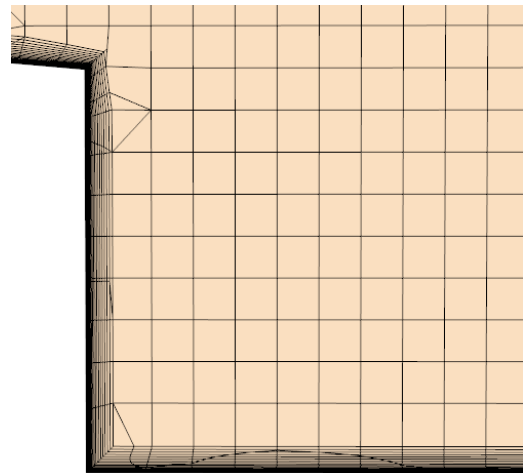


Figure 2.27: Volume mesh with a prism layer

In addition to the meshers, volumetric controls can be added in order to refine specific areas in the mesh. This is advantageous in places of high turbulence, both on the surface and within the volume mesh. Places which may benefit from this on a propeller include the propeller tips, as they create a significant amount of vortex shedding, and at the hub where the hub vortex occur.

2.5.3 Mesh Evaluation

To evaluate the quality in relation to simulation results the following parameters should be investigated:

- **Dimensionless wall distance, y^+**
- **Residuals**
- **Steadiness**

The **dimensionless wall distance, y^+** , is a tool utilised in CFD for near-surface meshing. In this area, also called the boundary layer, a steep velocity gradient arise from the non-slip condition and is defined between the wall and until 99% of the free-stream velocity. Within the boundary layer viscous forces are dominant, therefore the free stream parameter can not be used. The dimensionless velocity and wall distance in this layer are related to the actual velocity, wall distance, viscosity, wall shear stress and density and are expressed in the following equations (2.27) and (2.28) (Versteeg and Malalasekera, 2007):

$$u^+ = \frac{U}{u_\tau} \quad (2.27)$$

$$y^+ = \frac{u_\tau y}{\nu} \quad (2.28)$$

both use the friction velocity:

$$u_\tau = \left(\frac{\tau_w}{\rho_\infty} \right)^{\frac{1}{2}} \quad (2.29)$$

As the velocity gradient is non-linear it is divided into three additional sub-layers, viscous sub-layer, buffer-layer and log-layer. The viscous sub-layer is dominated by the viscous force and are found at a y^+ value below 5, which is the closest layer to the wall. The development of the viscous forces are her shown to be almost linear in progression, making y^+ equal to u^+ in this layer.

For CFD applications in which the forces on the walls or heat transfer between walls and the bulk flow is the main concern a y^+ value below 1 on the surface is preferable. Between a y^+ of 5 and 30 the buffer layer is situated, which utilises an empirical model to determine the relation between y^+ and u^+ . Lastly, at a y^+ value above 30 to approximately 500 the log-layer is found. The viscous and turbulence effects in this region approaches equality, making the relationship of y^+ and u^+ logarithmic. In the figure 2.28 below an illustration of this is presented.

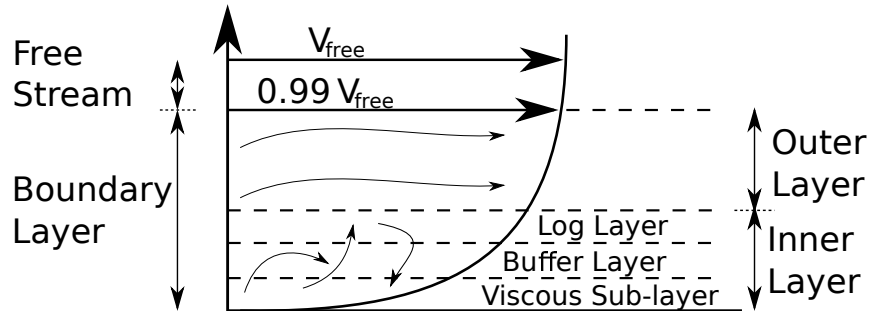


Figure 2.28: Inner and outer boundary layer illustration with inner layer sub layers from Dam and Jørgensen (2022).

Residuals, as explained in section 2.3.6, is the extent of which the chosen flow parameters are converged and satisfy the governing equations. In Star-CCM+ it is possible to obtain the local residuals in each cell. Through this, areas of high residual can be located and possibly refined in order to achieve a better convergence. **Steadyness** in a steady state simulation relates to how well the simulation converges to a constant value. In cases of large variation after a significant number of iterations, the mesh or models used should be investigated and possibly reconsidered.

Chapter 3

Grid Independence Study

3.1 Grid Convergence Index

To achieve results that are sufficiently accurate, grid independence is important to have ensured. For this, the Grid Convergence Index (GCI) will be utilised, and residuals and forces are checked to see if convergence is achieved, Celik et al. (2008). The GCI method compares 3 meshes of different sizes and calculates the theoretical deviation from the actual value for the finest mesh. The refinement ratios between the meshes have to be greater than 1.3 based the characteristic cell sizes which are calculated as follows:

$$h = \left(\frac{V_{\text{domain}}}{N_{\text{cells}}} \right)^{1/3} \quad (3.1)$$

And for the refinement ratios:

$$rr_{\text{cm}} = \frac{h_{\text{c}}}{h_{\text{m}}} = \left(\frac{N_{\text{m}}}{N_{\text{c}}} \right)^{1/3} > 1.3 \quad (3.2)$$

$$rr_{\text{mf}} = \frac{h_{\text{m}}}{h_{\text{f}}} = \left(\frac{N_{\text{f}}}{N_{\text{m}}} \right)^{1/3} > 1.3 \quad (3.3)$$

The subscripts c, m and f refer to the order of refinement, coarse, medium and fine and the combination of which are factors between those. The variables N and V_{domain} refer back to the respective meshes, where N is the number of cells in the mesh and V_{domain} is the volume of the domain the mesh occupies. Next, P , the apparent order of the numerical method, is computed iterative with the expression:

$$P = \frac{1}{\ln(rr_{\text{mf}})} \left| \ln \left| \frac{\epsilon_{\text{cm}}}{\epsilon_{\text{mf}}} \right| + \ln \left(\frac{rr_{\text{mf}}^P - s}{rr_{\text{cm}}^P - s} \right) \right| \quad s = \text{sign} \left(\frac{\epsilon_{\text{cm}}}{\epsilon_{\text{mf}}} \right) \quad (3.4)$$

The solution difference between the medium and coarse and the fine and medium meshes are denoted with ϵ . The parameter of interest ϕ_{mf} , can then be determined using the extrapolation:

$$\phi_{mf}^{(ext)} = \frac{rr_{mf}^P \phi_f - \phi_m}{rr_{mf}^P - 1} \quad (3.5)$$

Where the approximate and extrapolated error is found using:

$$e_{mf}^{(a)} = \left| \frac{\phi_f - \phi_m}{\phi_f} \right| \quad \text{and} \quad e_{mf}^{ext} = \left| \frac{\phi_{mf}^{(ext)} - \phi_m}{\phi_{mf}^{(ext)}} \right| \quad (3.6)$$

Lastly, the GCI for the fine mesh is calculated by:

$$GCI_f = \frac{1.25 e_{mf}^{(a)}}{rr_{mf}^P - 1} \quad (3.7)$$

This method is used in section 3.3 to investigate the effect of cell-numbers on the solution of open water and rudder simulations to finally settle on two meshes to be used throughout the report. The results are presented in table 3.2.

3.2 Mesh Generation

In accordance with the previously mentioned quality guidelines in 2.5 and requirement for the GCI, three meshes were constructed for a propeller with and without a rudder. As it was the same propeller which was modelled, a full cylindrical domain based on that of Rosenvinge and Sandland (2021) and Dam and Jørgensen (2022) was utilised for the grid independence test. The refinement ratios between the meshes were ≈ 1.4 and the growth ratio of the trimmed mesh was set to fast. Additional refinements were placed on select feature curves, where the angle changes significantly and a volume refinement of 5 percent of the base size is placed at the hub to capture the hub vortex and one with 10 percent on the propeller tips. The fine mesh for the simulation without rudder can be seen in the following figure 3.1:

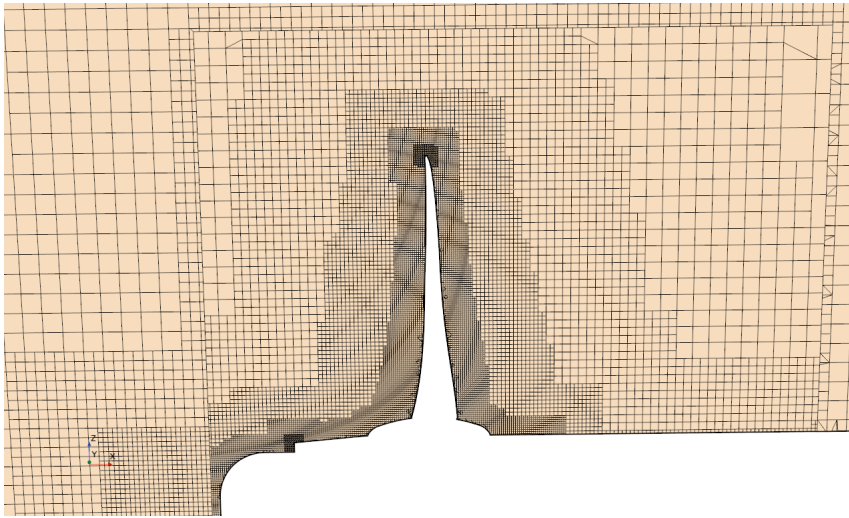


Figure 3.1: Fine mesh for the simulation without rudder.

For the simulation with rudder, the same refinement levels are applied to the rudder as the propeller, resulting in the mesh showed in figure 3.2:

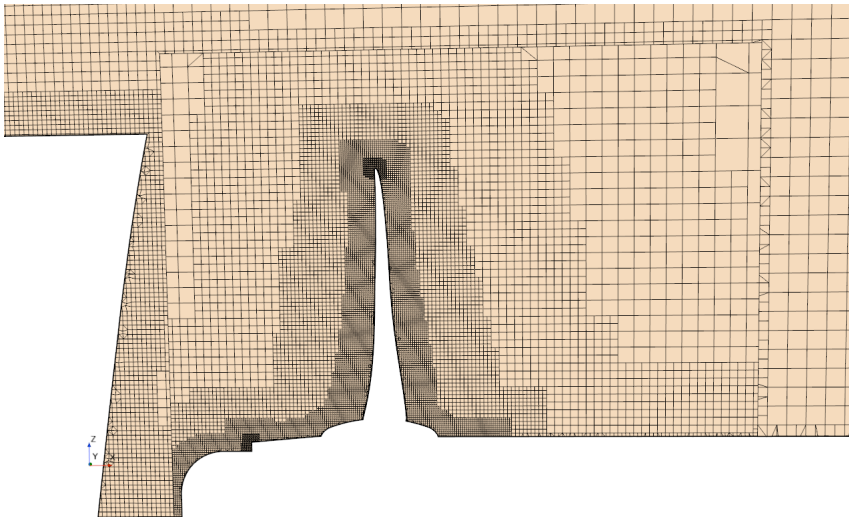


Figure 3.2: Fine mesh for the simulation with rudder.

Parameters for the different mesh refinement are found below in table:

Table 3.1: Mesh parameters for the coarse, medium and fine mesh used in the GCI study. **Results obtained after GCI was executed.*

GCI mesh parameters	Open Water			Rudder		
	Fine	Medium	Coarse	Fine	Medium	Coarse
Number of cells	$1.30 \cdot 10^7$	$4.38 \cdot 10^6$	$1.46 \cdot 10^6$	$1.45 \cdot 10^7$	$4.85 \cdot 10^6$	$1.62 \cdot 10^6$
Cells in the MRF domain	$1.15 \cdot 10^7$	$4.05 \cdot 10^6$	$1.34 \cdot 10^6$	$1.15 \cdot 10^7$	$4.05 \cdot 10^6$	$1.34 \cdot 10^6$
Cells in the outer domain	$1.50 \cdot 10^6$	$3.31 \cdot 10^5$	$1.19 \cdot 10^5$	$2.97 \cdot 10^6$	$8.02 \cdot 10^5$	$2.77 \cdot 10^5$
Maximum MRF skewness [°]	88.75	89.64	89.77	88.57	89.64	89.77
Maximum outer skewness [°]	82.39	87.07	84.82	89.77	89.85	89.93
Share of skewness >85° [%]	0.003	0.010	0.133	0.007	0.022	0.175
Average y^+ at blades* [-]	0.51	0.49	0.46	0.50	0.49	0.46
Maximum y^+ at blades* [-]	1.75	1.85	1.77	1.75	1.81	1.82
Minimum y^+ at blades* [-]	0.058	0.066	0.060	0.060	0.072	0.075
Maximum volume change [-]	1	1	1	1	1	1
Minimum volume change [-]	$8.89 \cdot 10^{-3}$	$2.31 \cdot 10^{-3}$	$1.80 \cdot 10^{-3}$	$7.31 \cdot 10^{-3}$	$2.64 \cdot 10^{-3}$	$1.71 \cdot 10^{-3}$
Share of volume change < $1 \cdot 10^{-2}$ [%]	0.000	0.001	0.004	0.000	0.001	0.003

From table 3.1 the amount of cells in each of the GCI meshes is presented. It illustrates that the MRF domains are identical between the open water and rudder implementation, where as the rudder implementation has approximately doubled the amount of cells in the outer region. This is also evident from the maximum skewness from the MRF, with the values being identical. Trends for the maximum outer skewness for the open water does not fit what would be expected, as the medium mesh see the largest skewness value. This trend could be due to the scaling method, where the base sizes were not scaled perfectly uniform and therefor could result in the mesher creating areas with poor interaction. Following a similar trend, y^+ for the medium mesh in open water also has a larger maximum and minimum value. By graphically comparing the suction and pressure sides figures A.11 to A.16 it is evident that the coarse mesh has a region with lower y^+ -values than the medium. The figures also present larger regions with low y^+ -values from fine to coarse. Residual plots and thrust and torque progressions are also displayed in appendix A.

The remaining parameters' increase in value between the fine, medium and coarse mesh, and are within the guideline values presented in sections 2.5.1 and 2.5.3.

3.3 Grid Convergence Index Results

All meshes were run for a model ships speed of 2.36 m/s and an angular velocity of 11.21 rps to obtain the thrust and torque coefficients, which are the parameters for which the GCI is conducted.

Table 3.2: Fine mesh grid convergence parameters of the thrust and torque coefficients for rudder and open water simulation.

Fine grid GCI parameters	Open water		Rudder	
	K_T	K_Q	K_T	K_Q
GCI [%]	4.54	0.20	2.57	0.36
P [-]	1.27	3.16	1.81	2.54
$e^{(a)}$ [%]	2.13	0.34	1.91	0.44
$e^{(ext)}$ [%]	3.50	0.16	2.01	0.29

From the results presented in table 3.2 it is evident that thrust is deviating mores from the theoretical value than torque, however both deviations are small (<5 %) so that the mesh can be called grid independent.

In case of both the open water and rudder GCI the torque coefficient is more grid independent compared to the thrust coefficient, inferred to by the percentages. This is believed to be a consequence of the meshing methodology which uses 18 prism-layers with fixed thicknesses no matter the overall cell count of the mesh. This is evident from the y^+ -values, presented in table 3.1, which are practically identical for the three meshes. The shear stress contributing to the torque is proportional to the velocity gradient dU/dy and is thus not affected much by the effects outside the boundary layer which is defined from 0-99% of the free stream velocity as this implies that $dU/dy \approx 0$ from 99-100%. Additional cells outside the boundary layer do not contribute to additional torque, which the GCI method also predict.

The thrust however is obtained from a pressure differential across the blades calculated as a summation of local pressures and hence the accuracy of the thrust is more dependent on cell sizes, as smaller cells in general yield higher precision in numerical methods.

Chapter 4

Validation

Validation of simulation results was made in order to determine the accuracy of the model-scale propeller simulations. To do this the simulated results and experimental tank test data given by MAN Energy Solutions Frederikshavn from the same propeller were compared. The experiments were conducted for open water and a rudder attachment. In parallel with the validation, comparisons between the γ - and γ - $\text{Re}_{\theta t}$ -transition models were conducted to evaluate their performances as little emphasis on the choice of the γ - $\text{Re}_{\theta t}$ -transition model is given in literature.

4.1 Open Water Simulations

The open water validation of the simulations was performed using the grid independent fine mesh presented in table 3.1 with constant angular velocity of 20 rps and advance ratios $0.3 \leq J \leq 1.0$ as these values were used in the model tank tests. The γ - and γ - $\text{Re}_{\theta t}$ -transition models were applied to evaluate their performances in terms of both accuracy and computational time. With use of the γ -transition model 7 variables are solved compared to 8 for the γ - $\text{Re}_{\theta t}$ -transition model, theoretically making it faster. To clarify, the 8 variables of the γ - $\text{Re}_{\theta t}$ -transition model simulations are: $u_x, u_y, u_z, p, k, \omega, \gamma$ and $\text{Re}_{\theta t}$.

In figures 4.1 and 4.2 the relative and absolute percentage deviation, calculated utilising equation (4.1), are given for each advance ratio for coefficients of thrust and torque and the open water efficiency for both transition models.

$$\Delta\phi_{Rel} = \left(\frac{\phi_{Simulation} - \phi_{Tank}}{\phi_{Tank}} \right) \cdot 100 \quad \text{and} \quad \Delta\phi_{Abs} = |\Delta\phi_{Rel}| \quad (4.1)$$

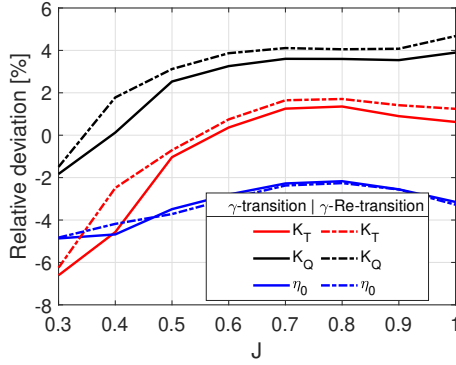


Figure 4.1: Plot of the relative percentage deviation of K_T , K_Q and η_0 for both the γ - and γ - $Re_{\theta t}$ -transition models in open water simulations.

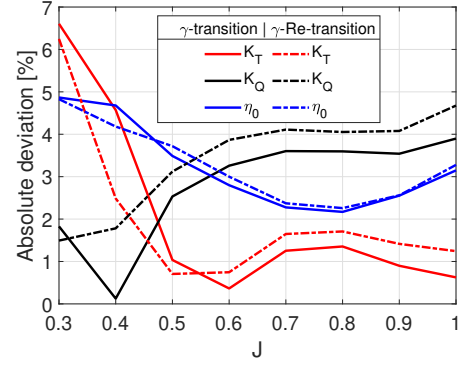


Figure 4.2: Plot of the absolute percentage deviation of K_T , K_Q and η_0 for both the γ - and γ - $Re_{\theta t}$ -transition models in open water simulations

The plots in figures 4.1 and 4.2 show good performance of both transition models for all parameters across the range of advance ratios. With exception of $J=0.3$ all parameters are within $\pm 5\%$ of the experimental data and for the range $0.6 \leq J \leq 0.9$, which is the more representative range, the absolute deviation is below 3% in the case of η_0 . In addition, it is evident that the γ -transition model marginally outperforms the γ - $Re_{\theta t}$ -transition model across all of the 3 parameters.

The aggregate computational time for the validations are 5h 47m and 7h 09m for the γ - and γ - $Re_{\theta t}$ -transition models, respectively, i.e. the γ -transition model performs the calculation in $\approx 80\%$ of the time of the γ - $Re_{\theta t}$ -transition model. The latter is significant when computational resources are limited and time is of the essence, which is generally the case for most companies.

Based on the presented matter above in this section both open water simulations are deemed validated and useful as the deviation generally is within $\pm 5\%$ which the general accepted threshold which the authors aim to comply with. In the specific simulations of this study the conclusion is that the γ -transition model is performing best and is thus used from hereon in open water simulations.

4.2 Rudder Simulations

The rudder simulation validation was performed in a likewise manner to that of the open water validation. In this case the advance ratio was kept constant through variation of both the angular velocity and model ships speed.

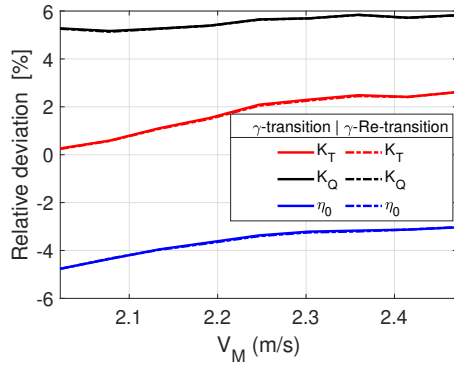


Figure 4.3: Plot of the relative percentage deviation of K_T , K_Q and η_0 for both the γ - and γ -Re- θ_t -transition models.

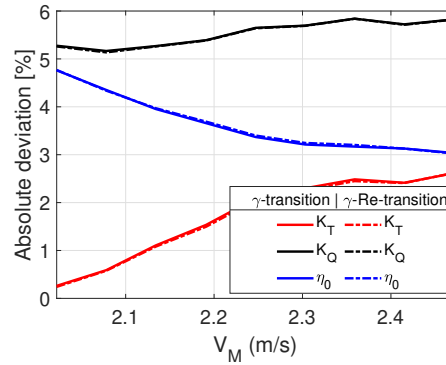


Figure 4.4: Plot of the absolute percentage deviation of K_T , K_Q and η_0 for both the γ - and γ -Re- θ_t -transition models.

From the plots in figures 4.3 and 4.4 it is difficult to distinguish between the two transition models as their performance is nearly identical across the range of ships speeds. The deviation is typically between $\pm 5\%$ with exception of K_Q that is over-estimated by 5-6%. Compared to the deviations of the open water simulations the deviations are generally larger and the spread between the parameters is bigger, possibly as consequence of the more complex flow arising from an additional geometry in the flow. However, the behaviour of the parameters and their accuracy are adequate, especially since the absolute deviation of the open water efficiency is always within 5%.

Once again both simulations are deemed validated and suitable for future use in the following studies.

Chapter 5

Pre Parametric Study

Following the observations made in both Rosenvinge and Sandland (2021) and Dam and Jørgensen (2022), improvements to the base geometry and meshing model can be made. Particularly in regards to the hub cap, and the refinement levels on the PBCF. Simulation run times were also investigated to improve workflow both in regards to number of cores and cells, subsequently by the use of a quarter domain.

5.1 Hub-Alteration

As stated in section 2.2 the hub is the last part of the shaft and has a direct influence on the hub vortex formation. The shape of the hub cap varies depending on application, but generally aim to be as streamlined as possible. It was found in the literature study that a cone with a rounded end yields the best results when PBCF are included, (Lim et al., 2014). The original hub-cap has this rounded end, with the exception of the flange, where the hub-cap is attached to the shaft. When implementing PBCF onto the original hub-cap the PBCF are limited to this initial converging part. If the PBCF were to be extended beyond this they could overlap with the bolts, making attachment difficult. For this particular propeller Rosenvinge and Sandland (2021) redesigned the hub by placing a cape above the original hub-cap in order to make it more hydrodynamically smooth and prevent overlapping regions between the PBCF and flange. The report used a limiting slope of 1.4° to ensure sufficient thickness of the cape, but theorised increasing the slope and elongating the hub-cap would produce a larger efficiency gain. As the same constrictions in regard to the rudder position applies to this report, investigating the increased slope by replacing the hub-cap was done instead.

This assumes that the thickness of the original hub-cap is sufficiently thick to withstand the forces acting on it and the same bolt locations could be utilised. The original and new hub are displayed in figures 5.1 and 5.2.

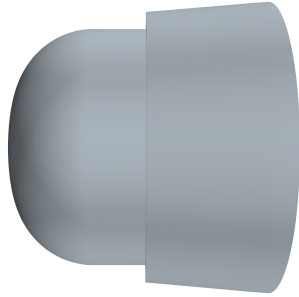


Figure 5.1: Original hub.

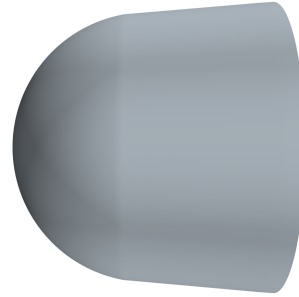


Figure 5.2: New hub.

To test whether the new hub outperforms the original, a thrust controller was utilised allowing the angular velocity to vary in order to obtain the same thrust. The thrust controller is explained further in section 6.1. Pressure coefficient and Q-criterion plots from the open-water simulation are displayed below in figures 5.3, 5.4, 5.7 and 5.8, similarly the plots for the rudder implementation are displayed in figures 5.9, 5.10, 5.11 and 5.12 along with the thrust, torque and open water efficiency results in table 5.1.

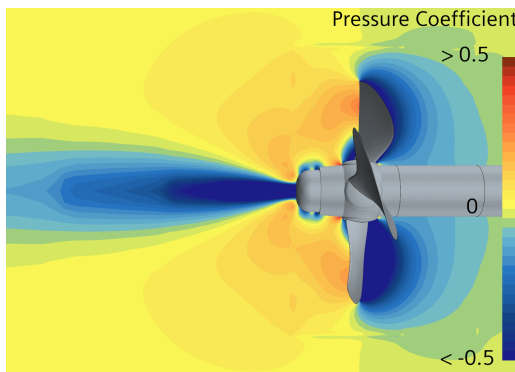


Figure 5.3: Pressure coefficient scalar plot for the original hub in open water conditions.

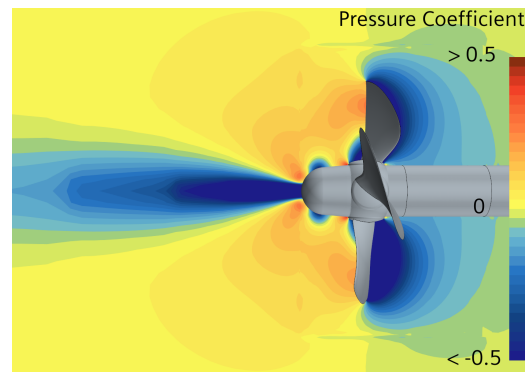


Figure 5.4: Pressure coefficient scalar plot for the new hub in open water conditions.

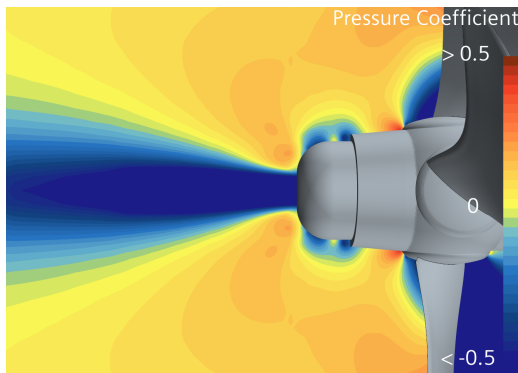


Figure 5.5: Pressure coefficient scalar plot for the original hub in open water conditions zoomed in on the hub.

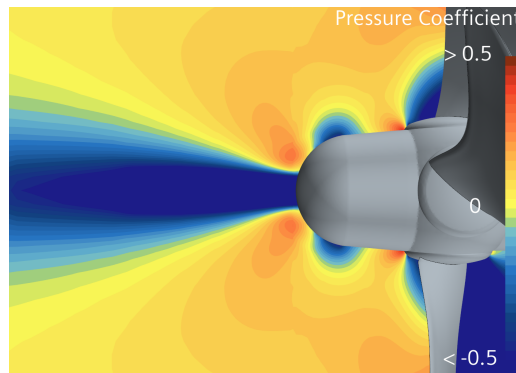


Figure 5.6: Pressure coefficient scalar plot for the new hub in open water conditions zoomed in on the hub.

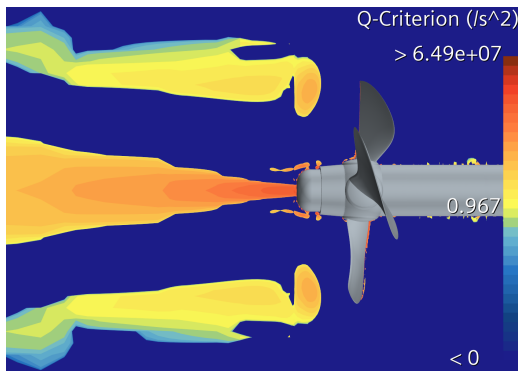


Figure 5.7: Q-criterion scalar plot for the original hub in open water conditions.

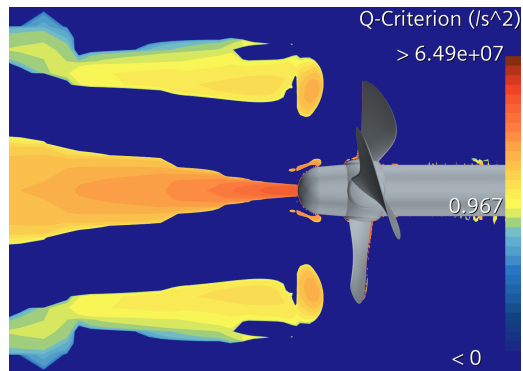


Figure 5.8: Q-criterion scalar plot for the new hub in open water conditions.

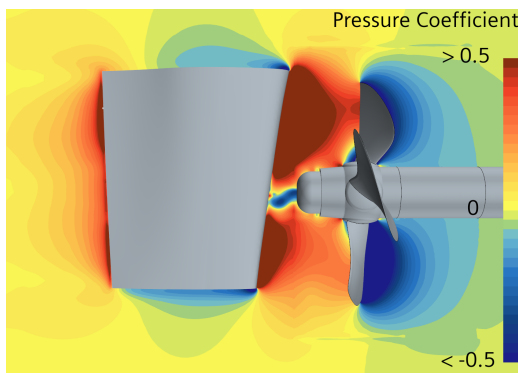


Figure 5.9: Pressure coefficient scalar plot for the original hub with rudder implementation.

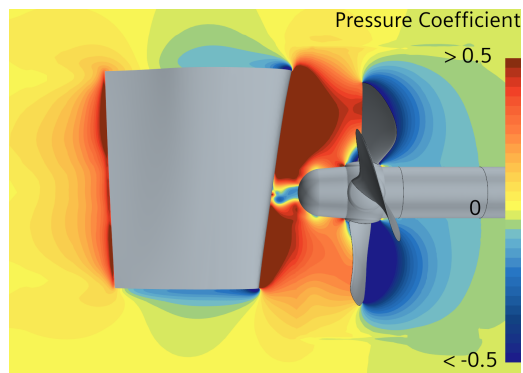


Figure 5.10: Pressure coefficient scalar plot for the new hub with rudder implementation.

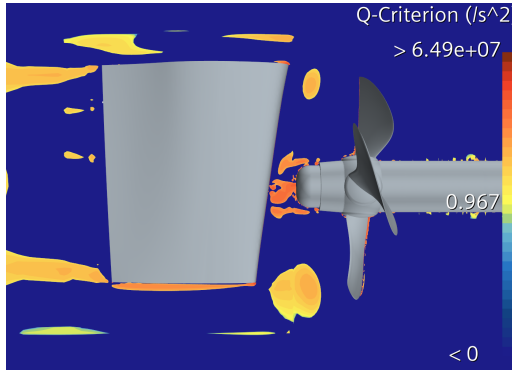


Figure 5.11: Q-criterion scalar plot for the original hub with rudder implementation.

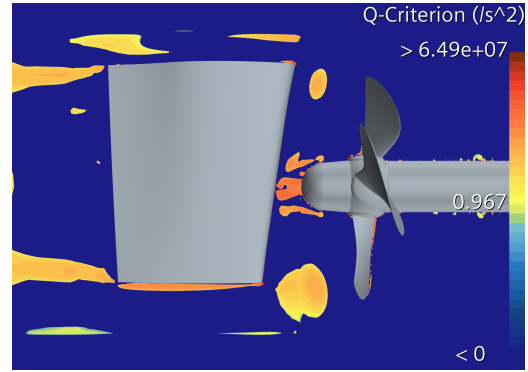


Figure 5.12: Q-criterion scalar plot for the new hub with rudder implementation.

Table 5.1: Changes in thrust and torque coefficients together with the percentage point gain in η_0 between the original and new hub.

	Open water	Rudder
ΔK_T [-]	$1.56 \cdot 10^{-4}$	$9.61 \cdot 10^{-5}$
ΔK_Q [-]	$-2.05 \cdot 10^{-5}$	$-8.52 \cdot 10^{-5}$
η_0 -gain [p.p.]	0.11	0.19

From comparing the two open water figures 5.3 and 5.4 it is evident that the new hub has a larger low-pressure zone as the hub rounds off and a more intense high-pressure zone at the hub vortex, however these combined do not create additional drag. On the Q-criterion figures 5.7 and 5.8 changes are seen to the satellite vortices, that originate from the hub rounding, where the new hub has a shorter but thicker vortex. Furthermore, the two hub geometries have approximately the same efficiency as presented in table 5.1. Similarly the rudder implementation plots in figures 5.9 and 5.10 show a larger lower pressure zone at the rounding of the hub. The low pressure zone right after the hub, created by the hub vortex, is visibly smaller and has a lower pressure coefficient. This is also seen on figures 5.11 and 5.12 where the vortex zone represented by the Q-criterion is slightly smaller with the new hub. Consequently, this change provided a small efficiency gain of 0.19 percentage points(p.p) as provided in table 5.1.

As the efficiency gains for the two simulations types were relatively small, it can not be argued that the new hub provide significant additional gains through being streamlined. However, it does not perform worse than the original hub and is therefor still logical to use, as it provides the PBCF a larger, uninterrupted installation area.

5.2 Propeller Boss Cap Fins Mesh Refinement

In effort to make the simulations more stable and more general for all PBCF implementations new refinement methods have been tested as previous computations with fixed volumetric refinement were unstable at times and yielded varying results. The previous attempts referred to are from Rosenvinge and Sandland (2021) and Dam and Jørgensen (2022). To combat these challenges parts-based meshing have been investigated as the number of surface cells scales with the geometry and the volumetric mesh then propagates from the surface into the computational domain, potentially creating smoother transition in cell size and shapes compared to previous attempts with volumetric refinement. Two approaches were examined; the first based on the edge between the suction and pressure side, and the other based on the whole PBCF geometry.

5.2.1 Edge-based Mesh Refinement

The edge-based refinement method define the curve between the suction and pressure side of the PBCF as a 'feature curve' from which a relative and target percentage of the base size is appointed. This method ensures high resolution at the edge that decays as the midpoint of the PBCF is approached due to the growth rate. The concept is illustrated in figure 5.13.

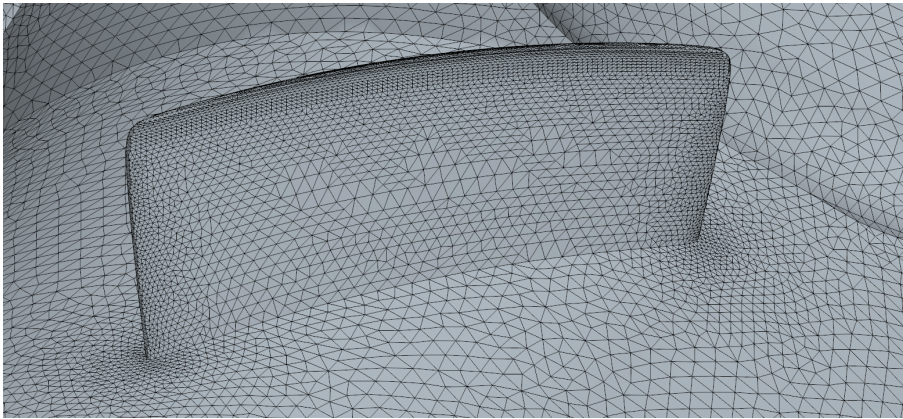


Figure 5.13: Surface mesh of a PBCF using the edge-based mesh refinement method.

5.2.2 Propeller Boss Cap Fins-based Mesh Refinement

The PBCF-based methods works similarly to the edge-based refinement but it includes more feature curves. Including the edge-curve, curves running from the leading edge to the trailing edge are also defined thus giving high resolution on the whole PBCF geometry at the expense of additional cells compared to the edge-based refinement. The concept is illustrated in figure 5.14.

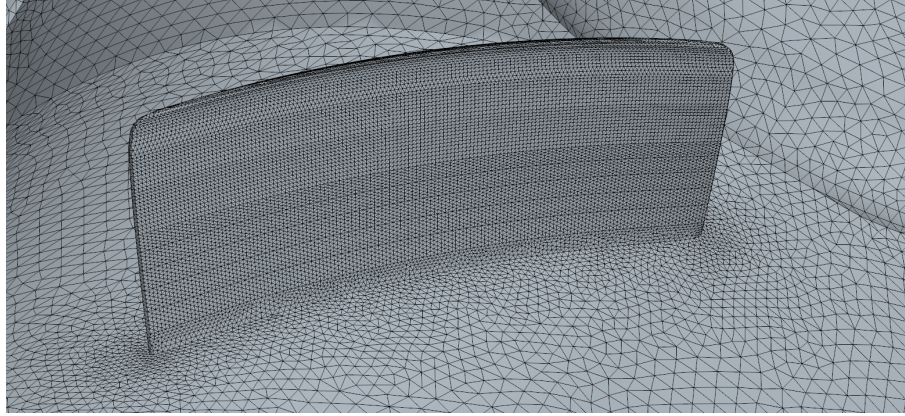


Figure 5.14: Surface mesh of a PBCF using the PBCF-based mesh refinement method.

5.2.3 Mesh Refinement Conclusion

Simulations of the edge-based and PBCF-based refinement meshing were computed to evaluate their performance. The residuals for each method along with the thrust and torque are plotted in the following figures, where Sdr denote the specific dissipation rate and Tke denote the turbulent kinetic energy:

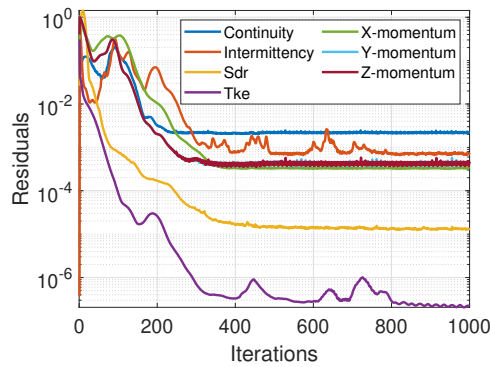


Figure 5.15: Residuals from a simulation using the edge-based mesh refinement method.

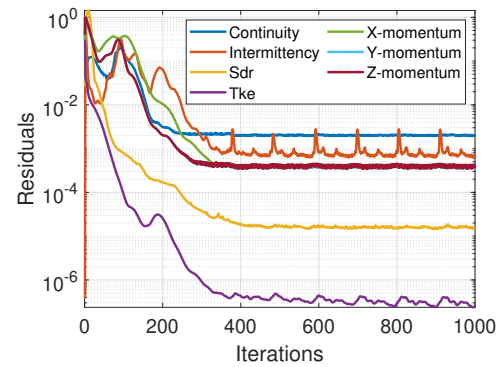


Figure 5.16: Residuals from a simulation using the PBCF-based mesh refinement method.

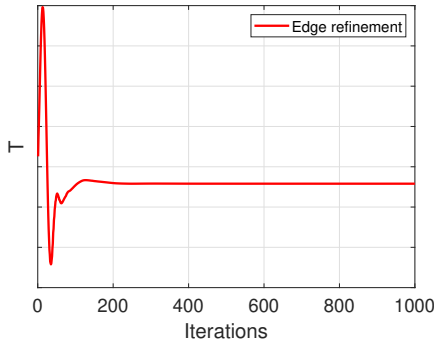


Figure 5.17: Thrust from a simulation using the edge-based mesh refinement method.

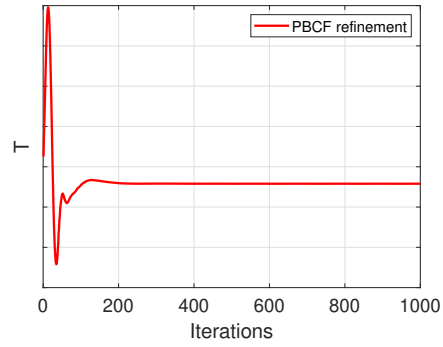


Figure 5.18: Thrust from a simulation using the PBCF-based mesh refinement method.

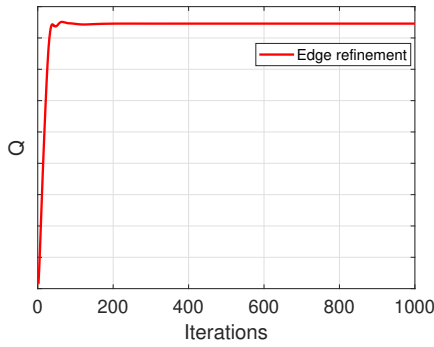


Figure 5.19: Torque from a simulation using the edge-based mesh refinement method.

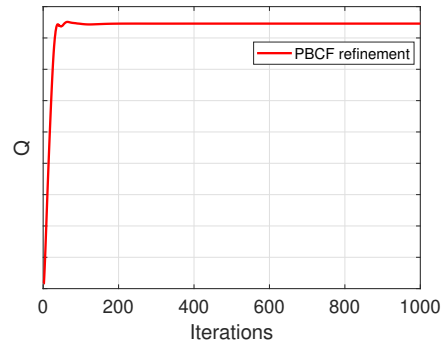


Figure 5.20: Torque from a simulation using the PBCF-based mesh refinement method.

From the results above it is clear that the performance of the two methods are very similar and yield satisfactory results. The residuals for the edge-based method does however converge to a higher degree than the PBCF-based method which also find strong cyclical trends. Hence, it is concluded that the edge-based method is preferable as the number of cells is smaller than that of the PBCF-based method with 15.0 and 16.7 million cells, respectively.

5.3 Analysis of Computational Resources

Commonly with commercially available CFD software individual licenses are acquired by the company together with a cluster containing a certain amount of cores. It is then a cost balance between potential usage and income opportunity,

as to how many cores and licenses are acquired. Therefore, it is highly beneficial to understand the impact of executing simulations with different amounts of cores to efficiently utilise the available resources. Logically, the computational time for one simulation would decrease as the amount of cores increase, but this would not be linear as communication time between cores would also increase. Similarly, an increase in the number of cells for a simulation would increase computational time. Simulation-time results from the cluster available at MAN Energy Solutions Frederikshavn are shown in figure 5.21 below.

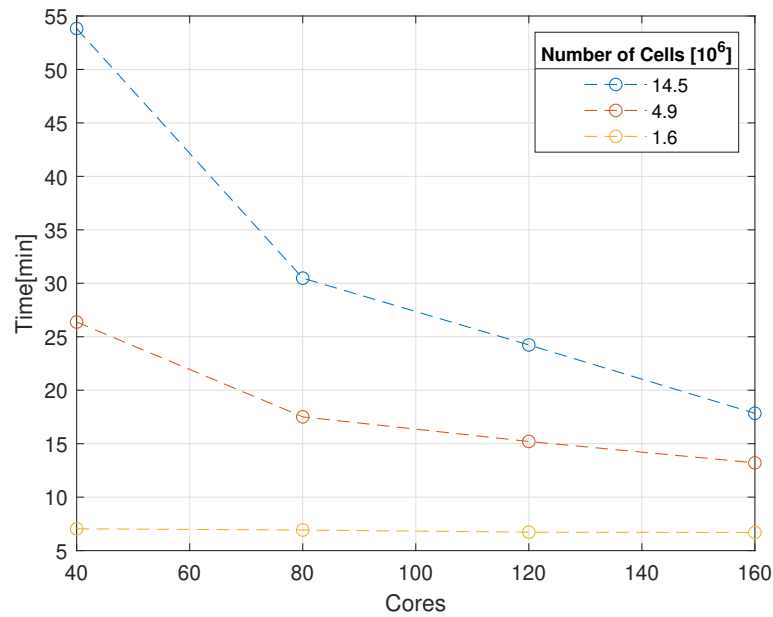


Figure 5.21: Computational time as a function of cores and cells. Each line represent a different amount of cells in the computational domain and increments of 40 cores were chosen based on the cluster architecture.

From figure 5.21 the previously discussed trends are evident as the decrease in computational time for 14.5 and 4.9 million cells when using 80 cores compared to 40 is greater than the decrease from 80 to 160 cores. In other words, the return is diminishing. Additionally the computational time between 14.5 and 4.9 million cells for 40 cores only doubles, even though the total amount of cells almost triples. In the case of the 1.6 million cells mesh 40 cores is already enough as communication time between cores halts the progress when more cores are used. Based on this investigation using 40 cores is optimal in terms of computational time but if licences are few 80 cores should be considered as the licence used is released after the simulation is finished ready to be used by others.

5.4 Computational Domain

As described in section 2.5 two possible domains are available for the study in this report; the quarter cylinder and whole cylinder. In order to potentially utilise the quarter domain, thereby reducing the computational time, a comparison test between the two domain types was performed. In the test the quarter domain was build from the open water domain, thereby having the same initial guesses and boundary conditions, except for the periodic interfaces. The periodical approach assume the periodic interfaces as being spatially detached and as the rotation occur eventually coincide, utilises the face values from one plane to reconstruct a gradient on the other plane. A representation of the quarter domain is presented in figure 5.22.

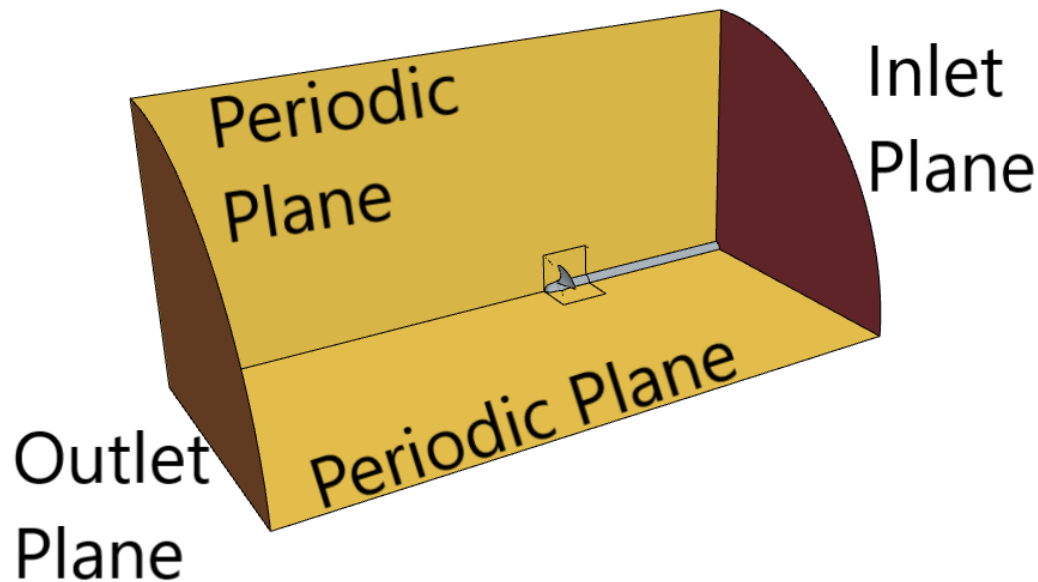


Figure 5.22: Quarter domain with illustrated periodic planes.

Physical results from the quarter domain is only a fourth of the true value, where as non-physical values such as residuals and y^+ -values does not see this influence. This arises from the physical values being determined as an integration over the selected surface area. The presented results in table 5.2 are therefore multiplied by four to compare with the full domain.

Table 5.2: Simulation results for K_T , K_Q , η_0 and the simulation time with 1000 iterations from the quarter domain as the relative deviation from the full domain.

	K_T	K_Q	η_0	t_{1000}
Relative deviation [%]	-0.33	-0.48	0.15	-76.45

From the results in table 5.2 it is evident that the quarter domain performs almost identically to the full domain, deviating less than 0.5 %. Arguably, by utilising the quarter domain, more accurate results could be obtained, as the full domain was found to overestimate K_T and K_Q and underestimate η_0 . Additionally, the reduction in computational time would allow for more results to be produced in the same time span, without compromising on the quality. Lastly, to ensure that the quarter domain is stable the residuals and physical properties thrust and torque are presented in figures 5.23 and 5.24.

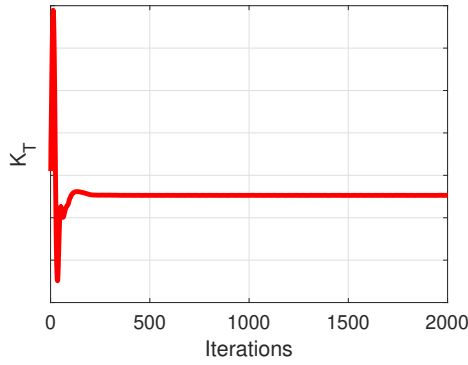


Figure 5.23: K_T during a range of 2000 iterations.

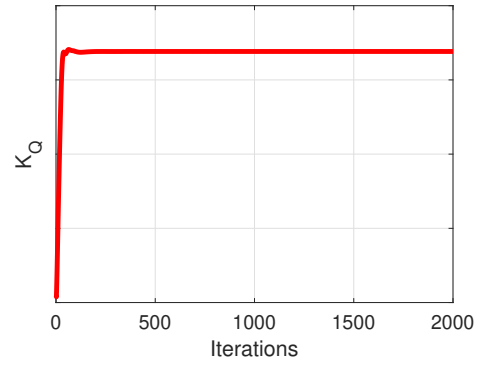


Figure 5.24: K_Q during a range of 2000 iterations.

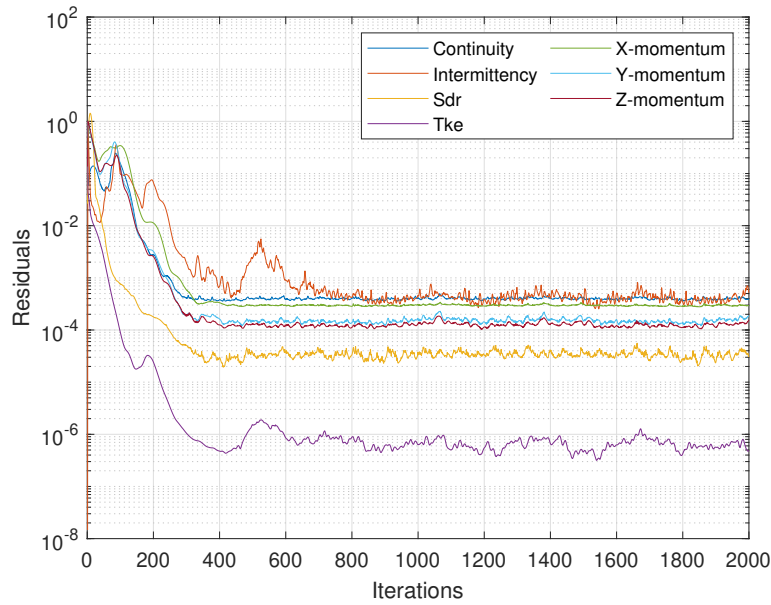


Figure 5.25: Residual results for 2000 iterations in the quarter domain.

Residuals for the quarter domain in figure 5.25 is said to converge around at iteration 1000, where fluctuations are minimal as is the case with the full domain. As the results from the quarter domain aligns with that of the full domain, the quarter domain will be utilised in the parametric study instead of the full domain in open water.

Chapter 6

Parametric Study

In this chapter the four PBCF parameters chord length, height, pitch and rake are investigated through a single-parameter study. The general setup and production method for the PBCF are stated and the best performing PBCF are found together with the contribution changes to thrust and torque. Lastly, the inflow to the PBCF is evaluated.

6.1 Parameter-Simulation Variables

The parametric study in this report focus on the effect of the four PBCF-parameters in regards to the hub vortex and open water efficiency. The study is a single-parameter study of the pitch, rake, height and chord length, where each parameter is simulated at 7 values giving a total of 25 simulations. In table 6.1 the 7 variations are assigned an identification (ID) number from 1-7. The fourth ID-number for each parameter, highlighted with bold font in the table, serves as the standard which is used as the basis for each parameter variation, hence the total of 25 simulations and not 28.

Table 6.1: Identification number for each variable parameter and their corresponding values.

Parameter	Identification Number						
	1	2	3	4	5	6	7
Chord Length (c/D)	3%	4%	5%	6%	7%	8%	9%
Height (r/R_p)	27%	28%	29%	30%	31%	32%	33%
Pitch	38°	42°	46°	50°	54°	58°	62°
Rake	0°	2°	4°	6°	8°	10°	12°

In appendix B a selection of the PBCF used in the parametric study is presented to visualise the parameter changes.

6.2 Workflow of the Parametric Study

Below in the figure the general workflow concerning the parametric study is presented to clarify the process from the beginning until the study is finished. The scheme is used for both the open water and rudder studies.

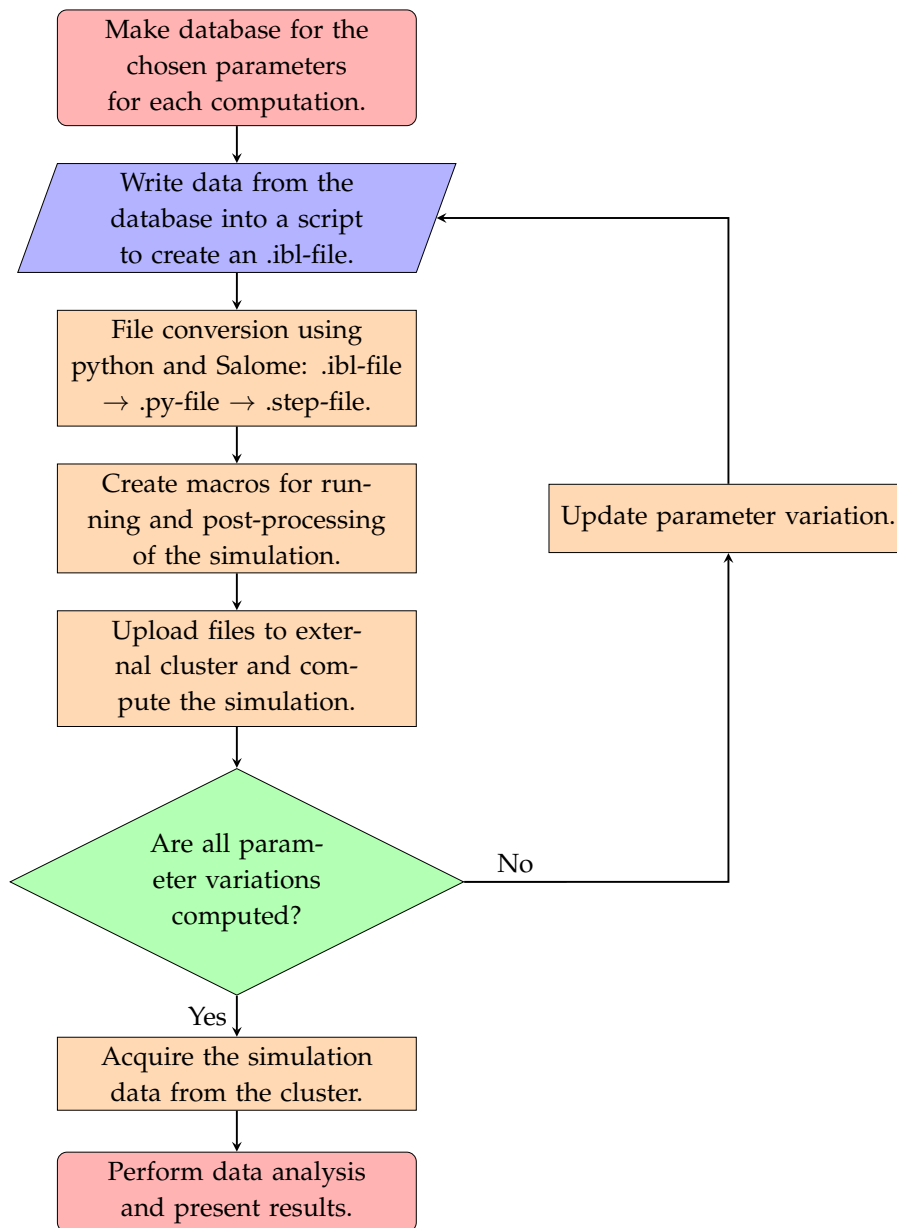


Figure 6.1: Flowchart of the workflow of the parameter study with all necessary steps from start to finish included.

6.3 General Simulation Setup

When examining equation (6.1) and (6.2) of the open water efficiency and the advance ratio it is evident that the efficiency is proportional to the thrust and inversely proportional to torque and angular velocity.

$$\eta_0 = \frac{J}{2\pi} \frac{K_T}{K_Q} \quad (6.1)$$

$$J = \frac{V_A}{nD} \quad (6.2)$$

To compare the efficiency improvements of each PBCF the thrust and thus ships speed is kept constant through variation of the angular velocity and the torque adjust freely accordingly. In order to maintain constant thrust a proportional controller is introduced which uses the deviation from the design thrust to correct the angular velocity of the propeller of the next iteration in the simulation. The thrust controller is formulated as follow:

$$n_i = n_{i-1} + K_p \cdot (T_{\text{design}} - T_{\text{actual},i-1}), \quad K_p = 0.04 \wedge 0.08 \quad (6.3)$$

The term T_{design} is the thrust of the propeller without PBCF operating at the design point and $T_{\text{actual},i-1}$ is the thrust of the propeller with PBCF operating at new conditions. The proportional constant K_p was determined iterative through a 'trial and error'-process for both the open water and the rudder simulations.

This method of determining the efficiency gain was also used in Rosenvinge and Sandland (2021) and Dam and Jørgensen (2022).

The initial conditions are kept the same for all simulations and are as presented in table 6.2. These values, except for velocity, are either default recommend values from the Star-CCM+ manual or from other similar studies. Mesh-parameter values for the base case are presented in table 6.3 below and are not constant for all parameter variations, but are representative of.

Table 6.2: Initial conditions used in the parametric study simulations.

Parameter	Value	Units
Velocity, U	(-2.36, 0, 0)	m/s
Pressure, p	0.0	Pa
Intermittency, γ	1.0	–
Turbulence Intensity, I	0.01	–
Turbulent Velocity Scale	1.0	m/s
Turbulent viscosity Ratio	10.0	–

Table 6.3: Mesh and simulation values used in the parametric study simulations.

Parameter	Value	Units
Number of Cells	$3.76 \cdot 10^6$	–
Range of y^+	[0.08;2.12]	–
Scaling factor, λ	21.24	–
Number of blades, Z	4	–
Range of Volume change	$[1.10 \cdot 10^{-2}; 1]$	m^3
Share of Skewness $> 85^\circ$	0.003	%

6.4 Efficiency Gain and Vorticity Results

Simulation results for the PBCF variations described in 6.1 are displayed in this section, for the open water and rudder implementation. This include for each of the parameter variations a graph of the percentage point gain in η_0 between the propeller with and without a PBCF for open water and rudder implementation and two Q-criterion plots. These Q-criterion plots are for a sideways slice through the centre of the propeller and hub normal to the x-axis and a wake slice, $0.74 D_p$ downstream from the propeller, showed from an upstream perspective.

6.4.1 Chord Length

Variations in the chord length was found to have an increasing efficiency gain, along the entire range, as the length increased. The efficiency gains provided by the PBCF are between 0.3 p.p. to 0.8 p.p, with the open water simulations finding increasingly larger gains compared to the rudder implementation as presented on figure 6.2.

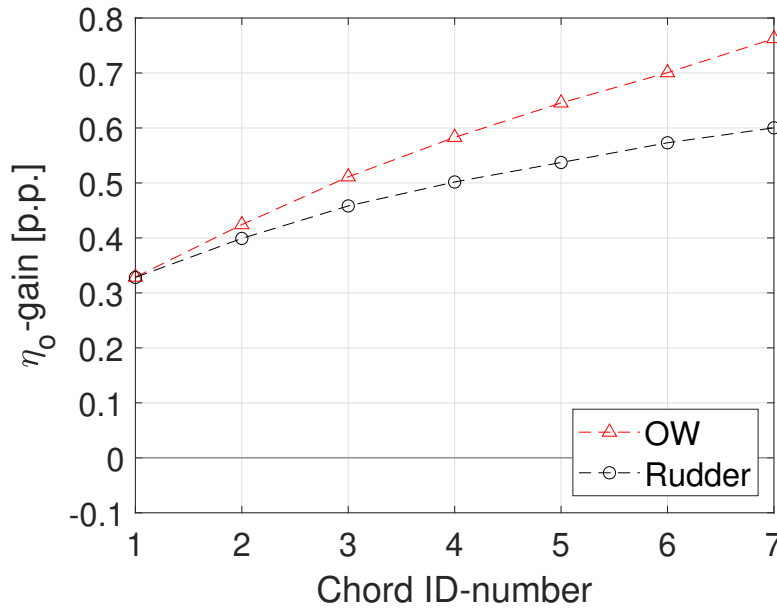


Figure 6.2: Percentage point gain in η_0 in the open water and rudder implementations with PBCF.

The Q-criterion results for chord ID-number 1 and 7 on figures 6.3 and 6.4 illustrate how the chord length of the PBCF alters the hub vortex downstream. The hub vortex originating immediately after the centre of the hub becomes narrower and the satellite vortices increase in size which results in them merging with the hub vortex. The corresponding low pressure zone induced by the hub vortex is reduced in size and intensity as the hub vortex diffuses which is evident from the pressure coefficient plots 6.5 and 6.6. To further emphasise this effect the iso-surface plots in figures 6.7 and 6.8 are provided below for a fixed Q-criterion value of 10 with a pressure coefficient overlay. Here the diffusion effect is once again visible as the physical size of the vortex increase for the Q-criterion value as the intensity from the core of the vortex is spread out, which in turn gives a larger pressure coefficient for the given Q-criterion value. The vortex diffusion between chord ID-number 1 and 7 is also evident from the wake slices in figures 6.9 and 6.10.

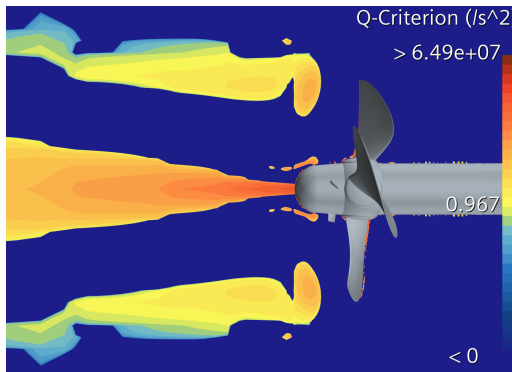


Figure 6.3: Open water Q-criterion representation for a sideways slice for chord length ID-number 1.

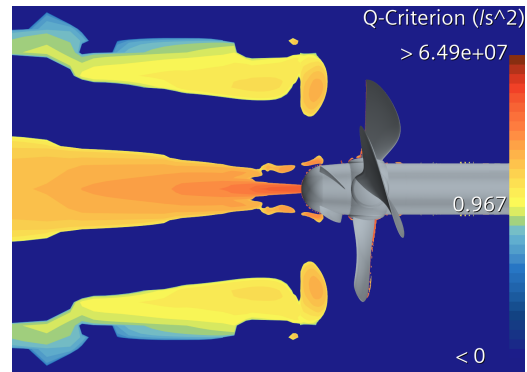


Figure 6.4: Open water Q-criterion representation for a sideways slice for chord length ID-number 7.

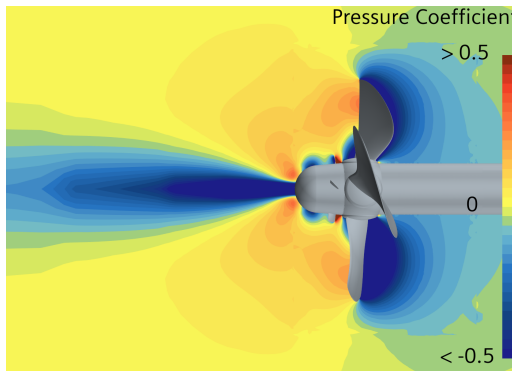


Figure 6.5: Open water pressure coefficient representation for a sideways slice for chord length ID-number 1.

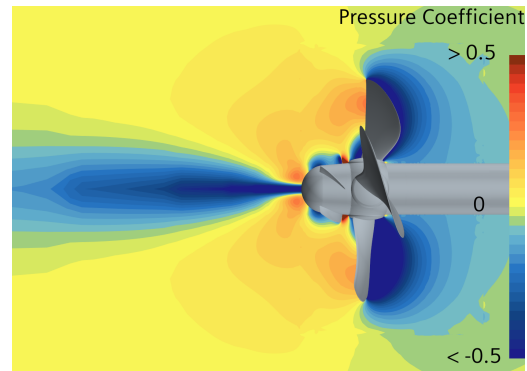


Figure 6.6: Open water pressure coefficient representation for a sideways slice for chord length ID-number 7.

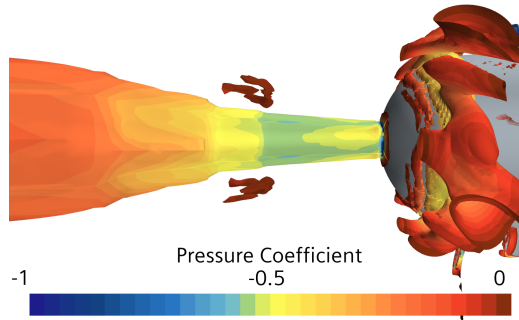


Figure 6.7: Iso-surface plot of the hub vortex for $Q=10 \text{ s}^{-2}$ with pressure coefficients between -1 and 0. This illustration is for chord length ID-number 1.

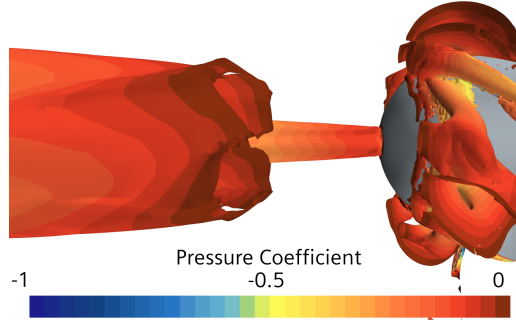


Figure 6.8: Iso-surface plot of the hub vortex for $Q=10 \text{ s}^{-2}$ with pressure coefficients between -1 and 0. This illustration is for chord length ID-number 7.

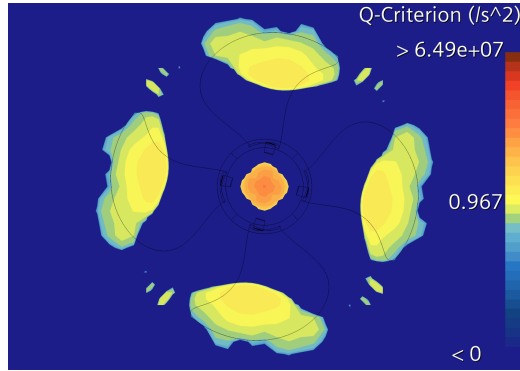


Figure 6.9: Open water Q-criterion representation for a wake slice for chord length ID-number 1.

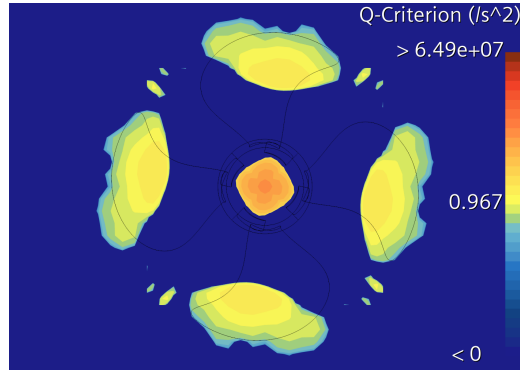


Figure 6.10: Open water Q-criterion representation for a wake slice for chord length ID-number 7.

The Q-criterion results with the rudder implementation are seen in figures 6.11 and 6.12 for the a sideways slice in the flow direction and 6.13 and 6.14 across the flow direction in the wake. The sideways slices illustrate how the immediate hub vortex before the rudder slightly decrease in width where as further downstream it increase in size. On the wake slices this effect is also visible as the hub vortex volume has increased and the intensity decreased, thereby making the hub vortex more diffused for the larger chord length. The surrounding vortices from the propeller tips remain unchanged.

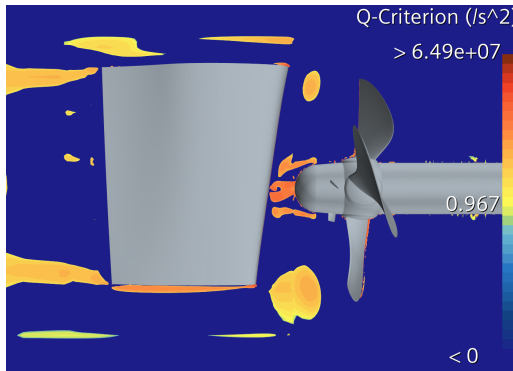


Figure 6.11: Rudder implementation Q-criterion representation for a sideways slice for chord length ID-number 1.

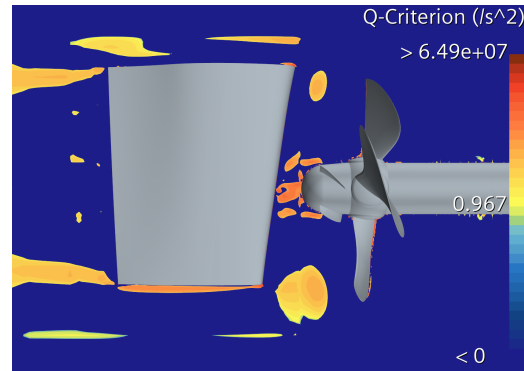


Figure 6.12: Rudder implementation Q-criterion representation for a sideways slice for chord length ID-number 7.

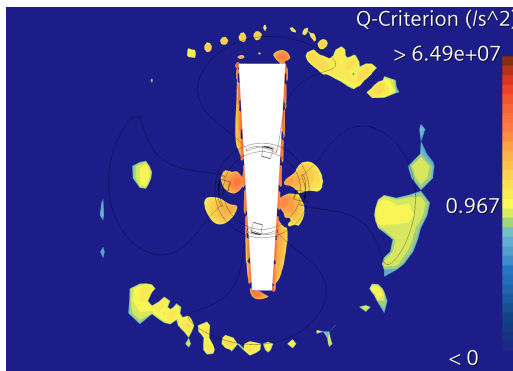


Figure 6.13: Rudder implementation Q-criterion representation for a wake slice for chord length ID-number 1.

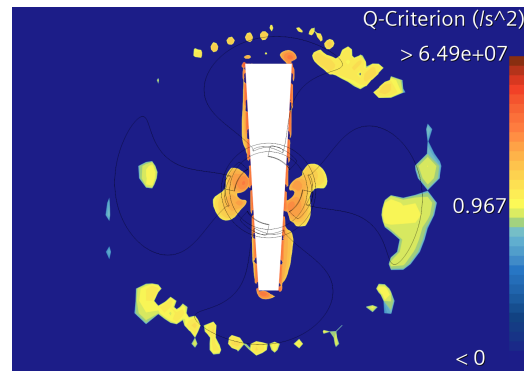


Figure 6.14: Rudder implementation Q-criterion representation for a wake slice for chord length ID-number 7.

6.4.2 Height

The height of the PBCF was according to the literature study to find an optimum between 15 and 33% relative radius, where most articles place the optimum in the upper half. From figure 6.15 this is proven to be true for this PBCF as well. The optimum for the open water simulations is at ID-number 6 with an efficiency gain of 0.12 p.p. and for the rudder implementation ID-number 5 with 0.51 p.p. efficiency gain. At a lower relative radius the efficiency gain is almost identical, but as the height increases the difference does so as well to a percentage point difference of 0.13.

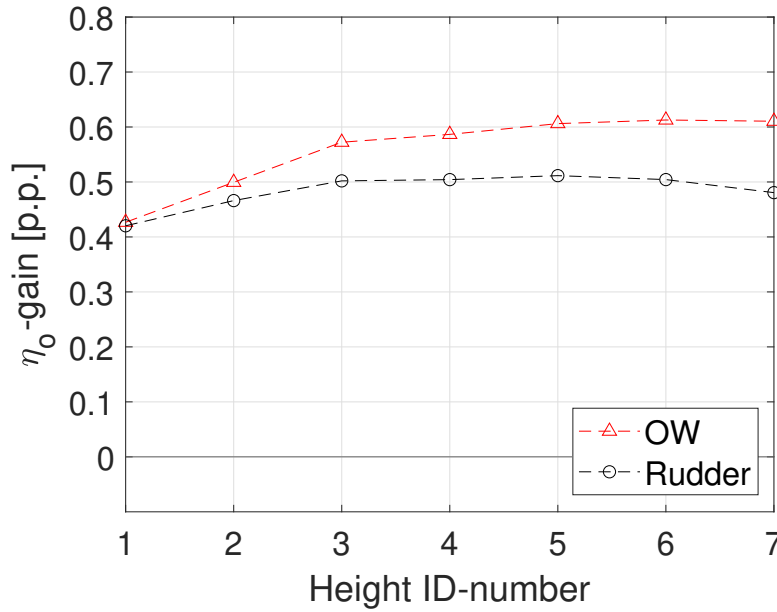


Figure 6.15: Percentage point gain in η_0 in the open water and rudder implementations with PBCF

On the figures 6.16, 6.17, 6.18 and 6.19 the open water Q-criterion for a sideways and wake slices are plotted to illustrate the changes in the flow between height 1 and 7 as the efficiency increase. The sideways representations show the satellite vortices are elongated by the height in a similar manner to the longer chord lengths. This results in the hub vortex lessening in intensity while the downstream hub vortex is wider, making it diffused which is evident from the wake slices. Similarly to the chord length, the propeller tip vortices do not change.

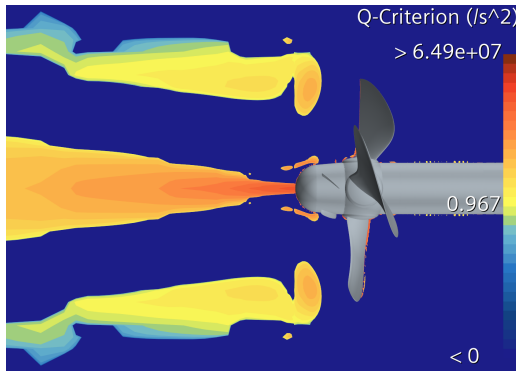


Figure 6.16: Open water Q-criterion representation for a sideways slice for height ID-number 1.

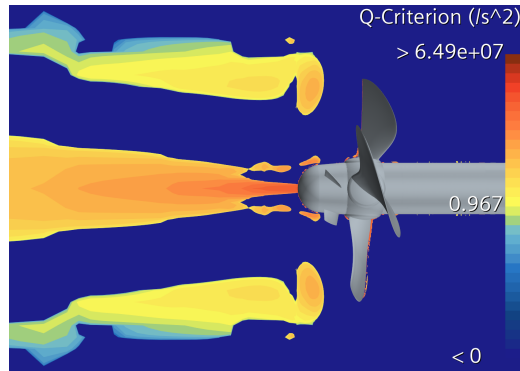


Figure 6.17: Open water Q-criterion representation for a sideways slice for height ID-number 7.

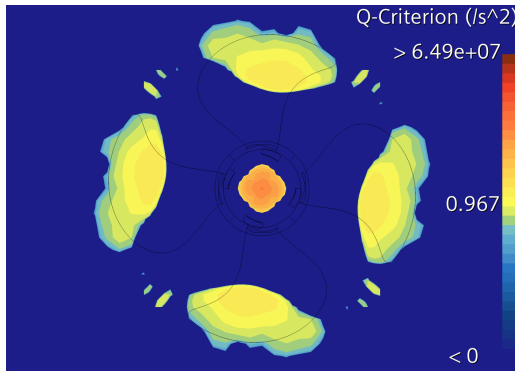


Figure 6.18: Open water Q-criterion representation for a wake slice for height ID-number 1.

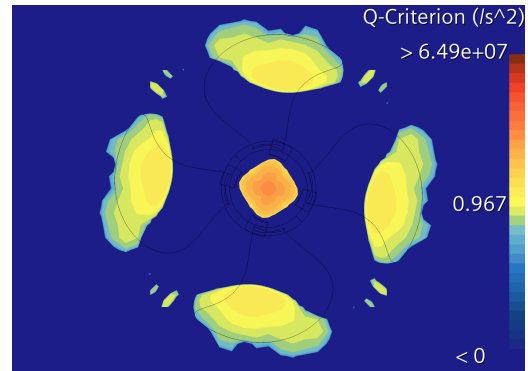


Figure 6.19: Open water Q-criterion representation for a wake slice for height ID-number 7.

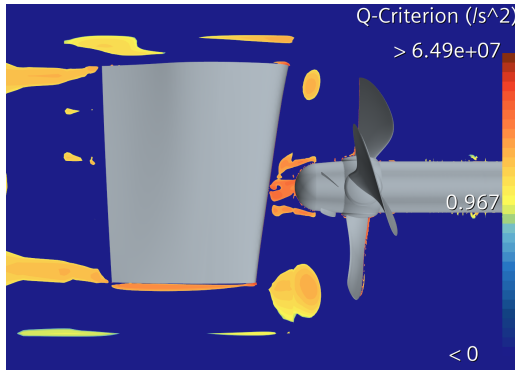


Figure 6.20: Rudder implementation Q-criterion representation for a sideways slice for height ID-number 1.

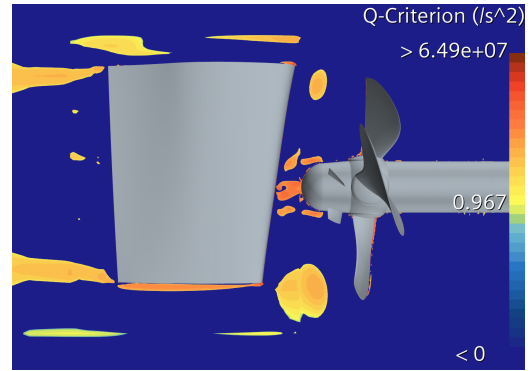


Figure 6.21: Rudder implementation Q-criterion representation for a sideways slice for height ID-number 7.

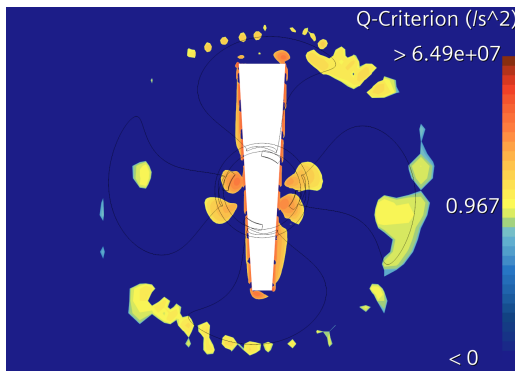


Figure 6.22: Rudder implementation Q-criterion representation for a wake slice for height ID-number 1.

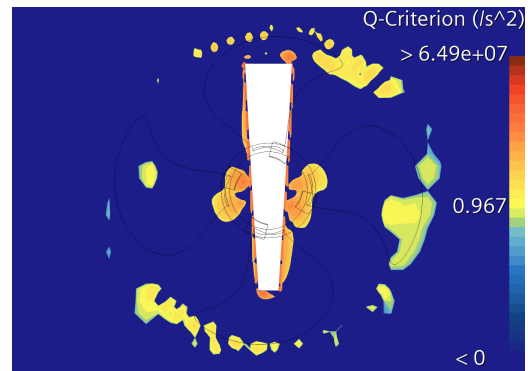


Figure 6.23: Rudder implementation Q-criterion representation for a wake slice for height ID-number 7.

The rudder implementation Q-criterion plots 6.20, 6.21, 6.22 and 6.23 also find a vorticity lessening effect at the hub vortex, where the satellite vortices detach. In the wake slices, similarly to what was observed for the chord length, the hub vortex region is more diffused.

6.4.3 Pitch

The pitch was varied between 38° and 62° , where the median value of pitch approached that of the propeller pitch at the hub. From figure 6.24 it is evident that pitch has a significant influence on the efficiency gain ranging from 0.67 to -0.01 percentage points. Open water produced a generally larger efficiency gain except for ID-number 7. Both simulations found pitch ID-number 2 as being the optimum point with a gain of 0.67 and 0.56 p.p., respectively.

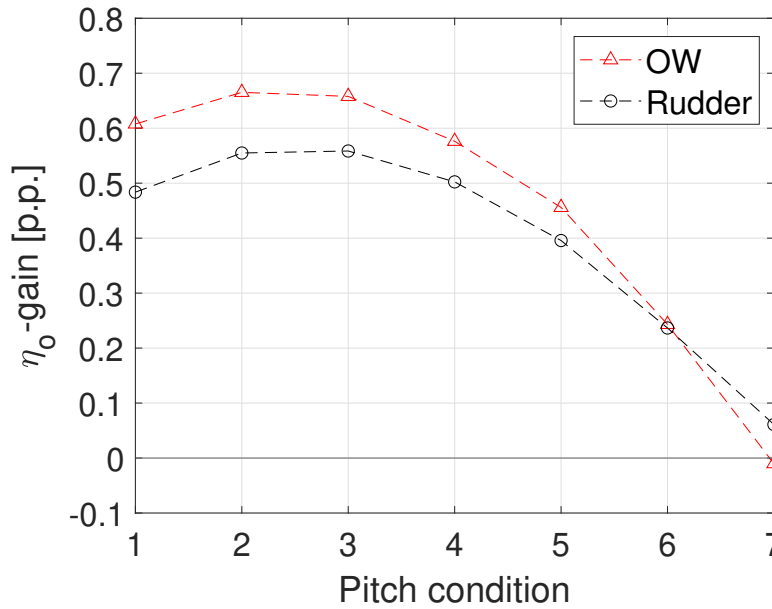


Figure 6.24: Percentage point gain in η_0 in the open water and rudder implementations with PBCF

To illustrate the change in vorticity the Q-criteria are plotted for ID-numbers 1, 3 and 7 on figures 6.25, 6.26, 6.27, 6.18, 6.18 and 6.19 due to the parabolic trend. From the sideways slice it is evident that as the pitch increases the hub vortex immediately after the hub does as well, whereas the satellite vortices decrease, especially between ID-number 3 and 7. Further from the hub the hub vortex diffuse between ID-number 3 and 7, whereas only the intensity changes between 1 and 3.

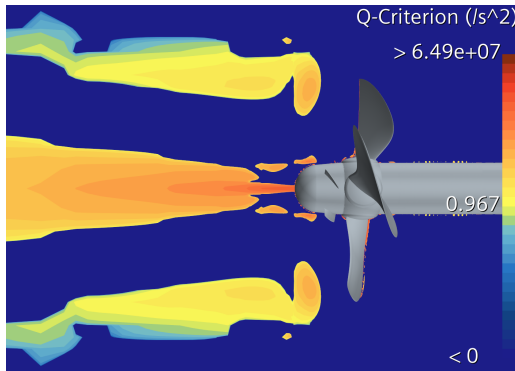


Figure 6.25: Q-criterion representation for a sideways slice for pitch ID-number 1

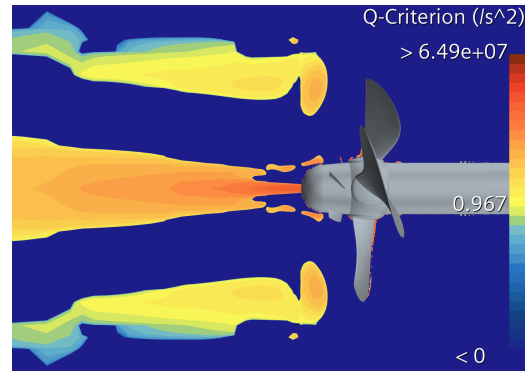


Figure 6.26: Q-criterion representation for a sideways slice for pitch ID-number 3

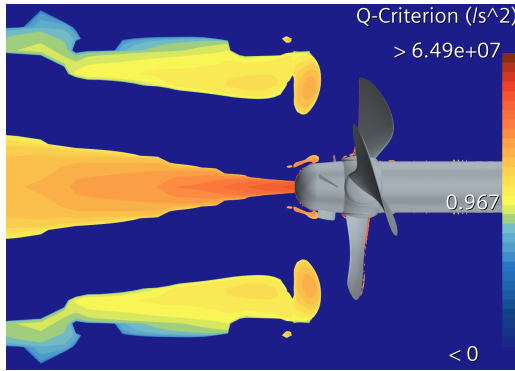


Figure 6.27: Q-criterion representation for a sideways slice for pitch ID-number 7.

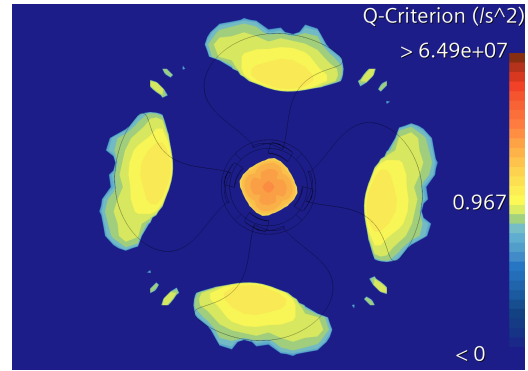


Figure 6.28: Q-criterion representation for a wake slice for pitch ID-number 1

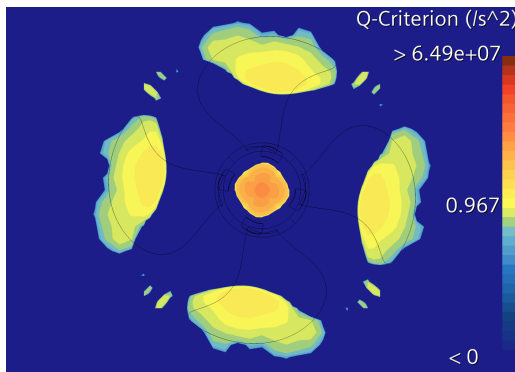


Figure 6.29: Q-criterion representation for a wake slice for pitch ID-number 3.

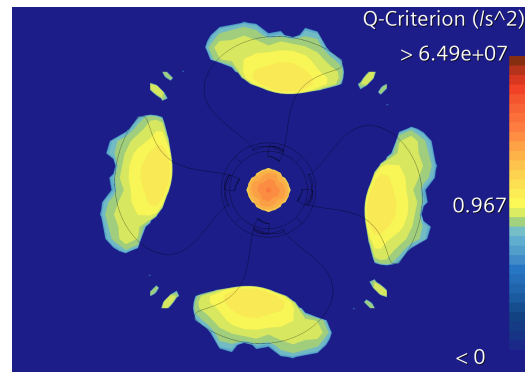


Figure 6.30: Q-criterion representation for a wake slice for pitch ID-number 7.

The vortex progression for the rudder implementation is different than that of the open water representation. On figures 6.31 and 6.33 the hub vortex and connected satellite vortices are larger than on figure 6.32. The wake representations on figures 6.34, 6.35 and 6.36 illustrate how the hub vortex diffuse from ID-number 7 to 3, where as only the intensity seem to decrease slightly between ID-number 1 and 3.

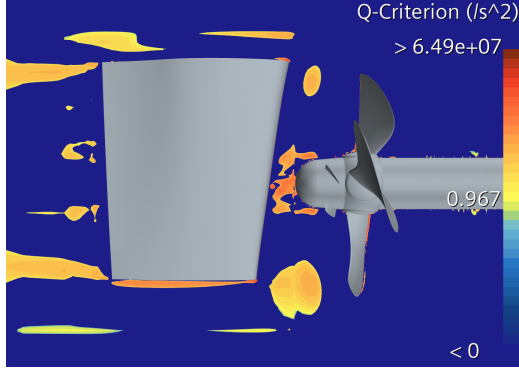


Figure 6.31: Rudder implementation Q-criterion representation for a sideways slice for pitch ID-number 1.

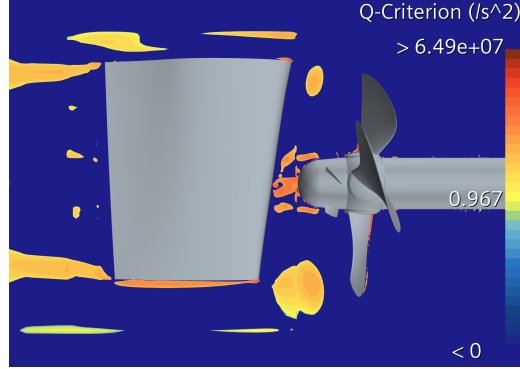


Figure 6.32: Rudder implementation Q-criterion representation for a sideways slice for pitch ID-number 3.

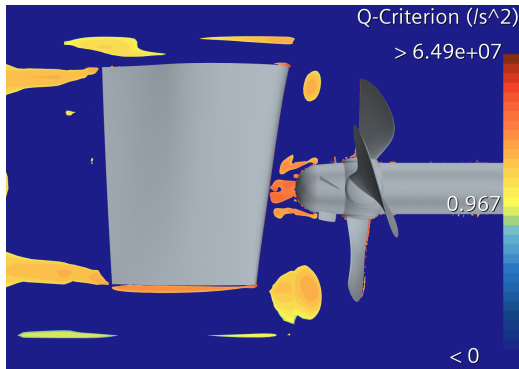


Figure 6.33: Rudder implementation Q-criterion representation for a sideways slice for pitch ID-number 7.

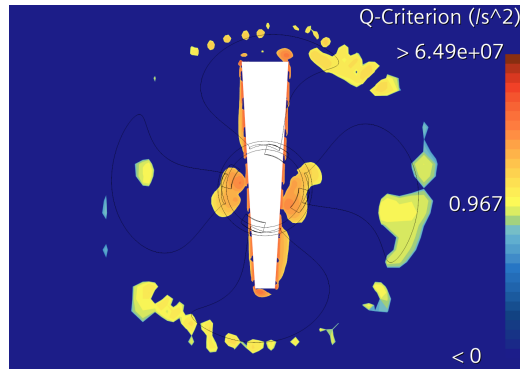


Figure 6.34: Rudder implementation Q-criterion representation for a wake slice for pitch ID-number 1.

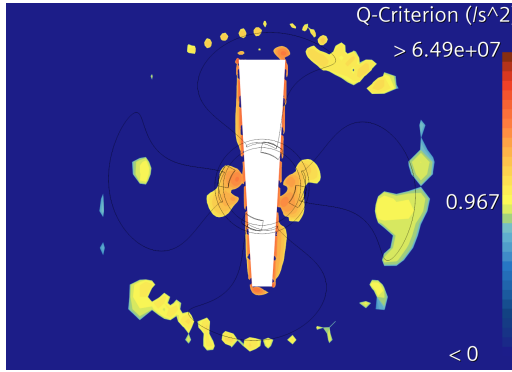


Figure 6.35: Rudder implementation Q-criterion representation for a wake slice for pitch ID-number 3.

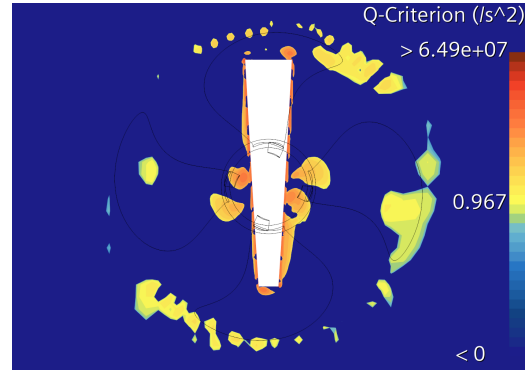


Figure 6.36: Rudder implementation Q-criterion representation for a wake slice for pitch ID-number 7.

6.4.4 Rake

Within the selected span of rake values, the efficiency gain increased with the rake. Resulting in optimal values at rake ID-number 7 of 0.61 and 0.52 p.p. gain respectively. Open water found between 0.07 and 0.09 p.p. more efficiency gain than the rudder implementation along the range, when ID-number 3 is disregarded.

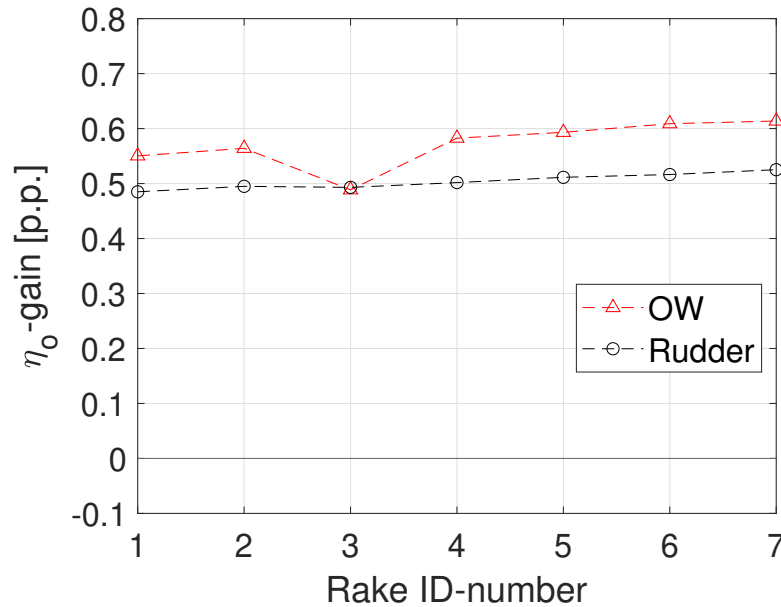


Figure 6.37: Percentage point gain in η_0 in the open water and rudder implementations with PBCF

The Q-criterion plots 6.38, 6.39, 6.40 and 6.41 illustrate the open water vorticity. The sideways slices appear similar, except for a small increase in satellite vortices. Similarly, the wake slices show only minute changes with the centre of ID-number 1 having a small area with a darker orange shade. The displayed changes align well with the small efficiency gain for open water found in figure 6.37.

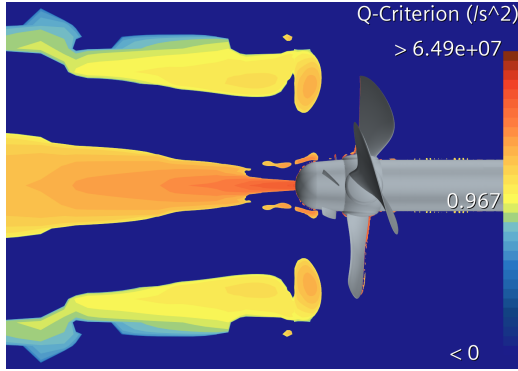


Figure 6.38: Open water Q-criterion representation for a sideways slice for rake ID-number 1.

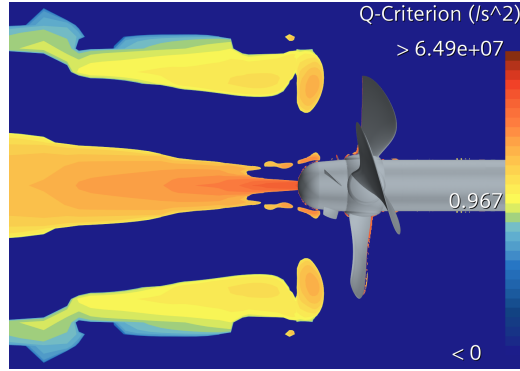


Figure 6.39: Open water Q-criterion representation for a sideways slice for rake ID-number 7.

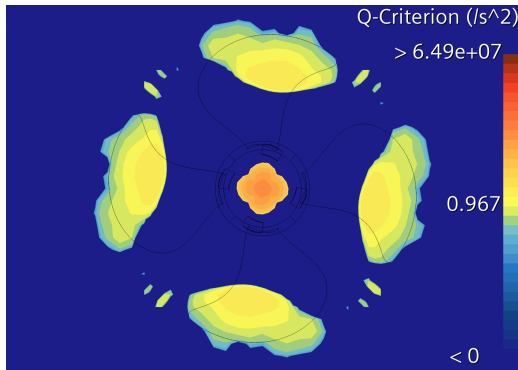


Figure 6.40: Open water Q-criterion representation for a wake slice for rake ID-number 1.

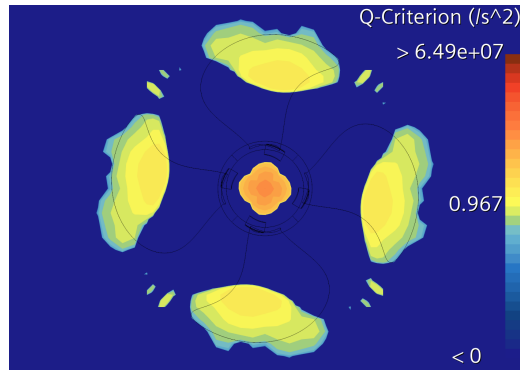


Figure 6.41: Open water Q-criterion representation for a wake slice for rake ID-number 7.

The rudder implementation Q-criterion plots 6.42 and 6.43 show less change than the open water counterpart. The wake slices 6.44 and 6.45 show changes on the left side of the rudder, where the vortices merge.

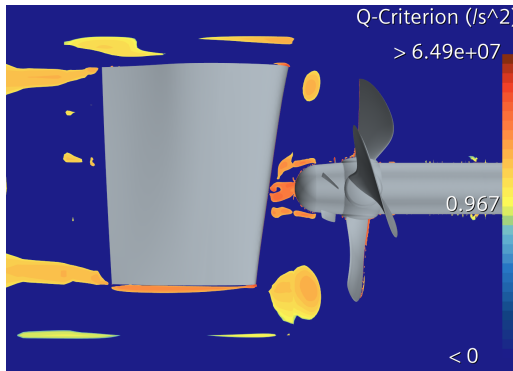


Figure 6.42: Rudder implementation Q-criterion representation for a sideways slice for rake ID-number 1.

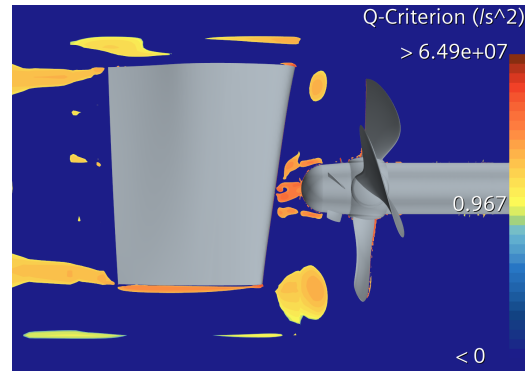


Figure 6.43: Rudder implementation Q-criterion representation for a sideways slice for rake ID-number 7.

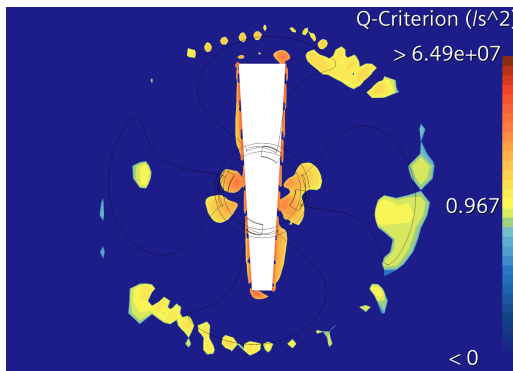


Figure 6.44: Rudder implementation Q-criterion representation for a wake slice for rake ID-number 1.

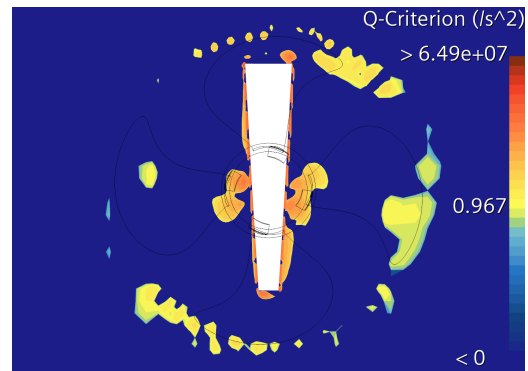


Figure 6.45: Rudder implementation Q-criterion representation for a wake slice for rake ID-number 7.

6.4.5 Recapitulate Remarks on the Results

A general trend presented throughout the results is the gap in efficiency gain from the open water to the rudder simulations. The efficiency gain in open water conditions are often >10% greater than in the rudder conditions. This is the case as the rudder is an ESD in itself, evident from the ≈ 3 p.p. greater open water efficiency presented in table 5.1, thus giving diminishing returns when another ESD is implemented.

In general the parameters are evenly matched across the ranges, each giving anything between 0.4-0.8 p.p. The height and pitch have reached an optimum within the range, the rake is almost constant with a slight rising trend and finally the

chord length is steadily rising suggesting an even longer PBCF could bring more performance.

The Q-criterion visualisation is succeeding in showing the vortices and the effects the PBCF have on the hub vortices, however, the method has its limitation in the rudder cases where many scattered vortices are present. No changes to the tip vortices were found throughout this study, suggesting the PBCF do not impact this region of the flow which was expected as the literature solely focused on the hub vortex.

6.5 Best Performing Propeller Boss Cap Fins

In the previous section 6.4 the influences of the different parameters were explored and clear trends were found. Utilising these results and combining the most efficient parameter values an optimum PBCF is produced, assuming all the parameters work independently. In table 6.4 a recap of the design conditions for the base case, best parameter values from the parametric study and best overall parameter, together with the individual efficiency increases are presented.

Table 6.4: Design parameters for the base case, best parameter values from the parameter study and the overall best design, chord length ID-number 7 (C7).

Parameters	Base Case	Best Parameter values	C7
Chord Length (c/D_P) [%]	6	9	9
Height (r/R_P) [%]	30	31	30
Pitch [°]	50	42	50
Rake [°]	6	12	6
Efficiency gain			
OW [p.p.]	0.58	0.65	0.76
Rudder [p.p.]	0.50	0.51	0.60

From the efficiency gains in table 6.4 it is clear that the four design parameters has an internal influence which should be accounted for as the combined 'best parameter values' efficiency is lower than that of the chord length ID-number 7 (C7). To properly quantify these combined effect a comprehensive optimisation study where all possible combinations are explored should be conducted, such as Dam and Jørgensen (2022), Mizzi et al. (2017) or Lim et al. (2014). For the following investigations PBCF C7 are therefor utilised as they found the largest efficiency gain.

6.5.1 Distribution of Thrust & Torque Coefficients

Having quantified the influence of the PBCF on the η_0 and vorticity, in the previous sections, this subsection will explore the thrust and torque coefficient contributions from the different geometry parts for the best PBCF, C7. This was done by separating the propeller into five parts: Pressure and suction side (PS and SS) of both the propeller blade and PBCF and hub. The propeller blades and PBCF were split into pressure and suction side as the two sides contribute differently to the thrust and torque coefficients. To calculate the weighted relative difference the following equations 6.4 and 6.5 are used:

$$\Delta K_{T,Part} = (K_{T,Part,PBCF} - K_{T,Part,woPBCF}) \cdot 100 \quad (6.4)$$

$$\Delta K_T = \frac{\Delta K_{T,BladePS}}{K_{T,Total}} + \frac{\Delta K_{T,BladeSS}}{K_{T,Total}} + \frac{\Delta K_{T,PBCFPS}}{K_{T,Total}} + \frac{\Delta K_{T,PBCFSS}}{K_{T,Total}} + \frac{\Delta K_{T,Hub}}{K_{T,Total}} \quad (6.5)$$

Each fraction in equation 6.5 relates to the weighted relative difference which the part find by the inclusion of the PBCF. As the PBCF do not have a K_T value before the inclusion, the $\Delta K_{T,PBCF}$ is of the same value as the $K_{T,PBCF}$. The relative deviation for K_Q is calculated using the same equations as for K_T . The changes are presented in table 6.5 and figure 6.46.

Table 6.5: Relative deviation for the thrust and torque coefficients of the different propeller parts. Note the unit is per mille.

Propeller Part	Weighted relative deviation [%]	
	ΔK_T	ΔK_Q
Blade Pressure side	4.93	4.12
Blade Suction side	-2.26	-2.88
PBCF Pressure side	-12.39	-8.05
PBCF Suction side	-4.94	-1.09
Hub	17.11	0.06
Total	2.4	-7.8

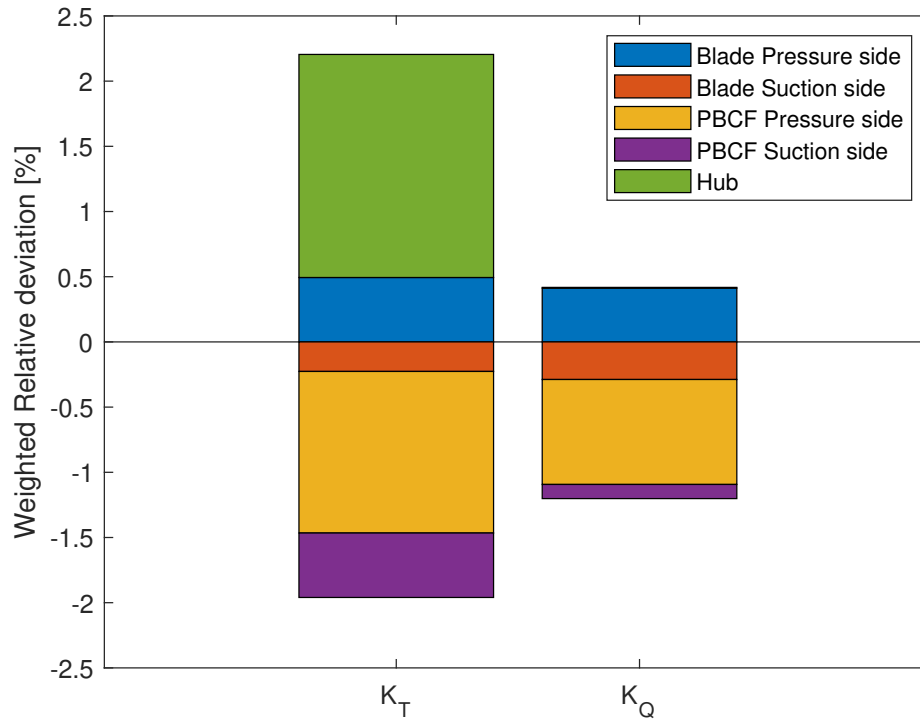


Figure 6.46: Individual influences of the propeller geometry on the thrust and torque coefficient expressed as the relative deviation between the open water simulation base case and C7.

In figure 6.46 the individual changes in K_T and K_Q for the geometry parts are presented. It is evident that the relative deviations of K_T and K_Q for each part are exclusively positive or negative. It should be noted that a negative relative deviation in K_Q result in a larger efficiency and should therefore be viewed as a positive effect. The hub is the geometry part which find the largest relative deviation which is expected since hub vortex is the phenomenon that should be mitigated to increase the open water efficiency. The weaker vortex affecting the hub is essentially increasing thrust per definition. Naturally, the PBCF experience a change as they are introduced and the blades experience minor changes as the demand for thrust changed with the weakened hub vortex and the rotational speed is changed because of the thrust controller.

6.6 Inflow Analysis of Propeller Boss Cap Fins

From the results in section 6.4 it is evident that the optimum pitch angle of the PBCF is lower than that of the propeller, as shown in figure 6.24. From this clear tendency a study of the flow around the propeller foot was initiated in an effort to determine the angle of the flow around the propeller foot, angle of attack (AoA) of the PBCF, potential upstream-effects on the flow due to the PBCF and the combined effect of those.

The velocity vector \mathbf{U} was obtained upstream of the PBCF to avoid errors due to the displacement around the profile, from Star-CCM+, to calculate the flow angle and a figure of seeded streamlines was rendered to visualise the 3-dimensional flow around the propeller foot and PBCF.

The flow angle leading to the front of the PBCF was deemed constant along the height of the PBCF and a representative point was chosen from which the angle was calculated at 58° from the y-z-plane (same reference as the pitch angle).

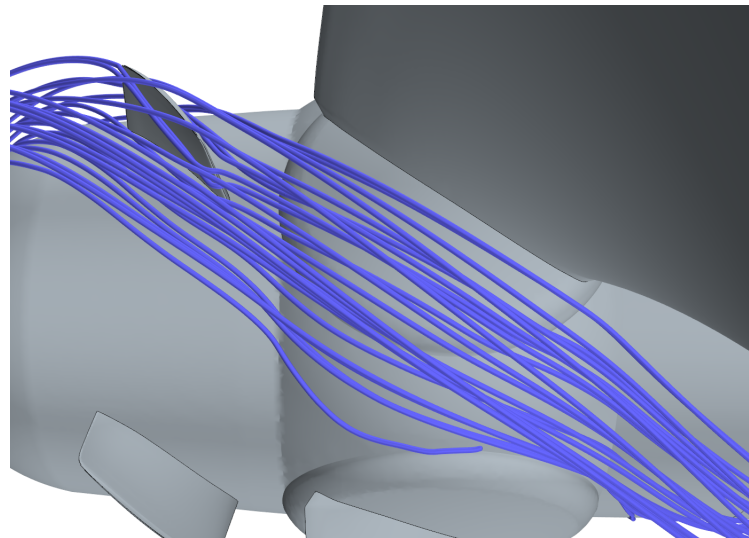


Figure 6.47: Illustration of the inflow towards a PBCF blade with optimum pitch using blue seeded particles.

The conclusion is that the flow is not parallel with the propeller chord in front of the PBCF and the PBCF experience a flow with negative AoA for the optimum condition.

Comparing the flow of the base case and the case of the optimum pitch the upstream effect of the PBCF is negligible as the flows aft of and next to the propeller are indistinguishable.

Chapter 7

Controllable Pitch Propeller Study

In the following chapter the interaction between a CPP propeller and PBCF was investigated. This include the operational conditions of the propeller and a theoretical expanded operational pitch range with variations in both pitch and ships speed. Lastly, the propeller was pitched at a constant ships speed to examine the effects.

7.1 Propeller Pitch

Propellers can be divided into two subcategories: Fixed and controllable pitch propeller abbreviated FPP and CPP, respectively. What differentiates the CPP from the FPP is its ability to change the pitch, which gives an additional degree of freedom. It can therefore, in off-design, achieve higher efficiencies and lower fuel expenditures in comparison to the FPP. Examples of the pitch in condition 1 and 4 from table 7.1 are displayed in figures 7.1 and 7.2.

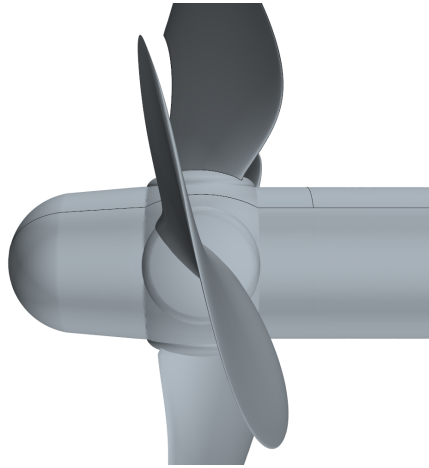


Figure 7.1: Propeller with a 48.8° pitch from condition 1.

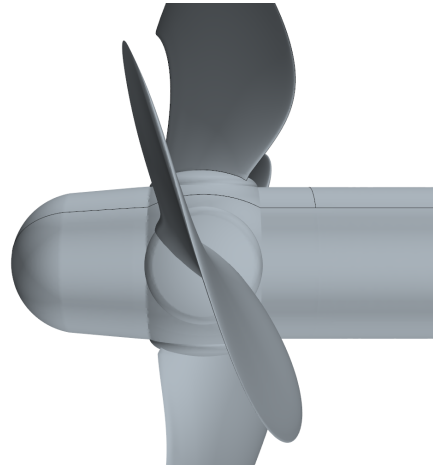


Figure 7.2: Propeller with a 53.4° pitch from condition 4.

In practise there are three modes of operation:

- **Constant angular velocity (Synchronous mode):** The angular velocity is kept as a constant with the pitch adjusting which simplifies the operational conditions.
- **Combinator mode:** Adjusting angular velocity and pitch according to predefined settings along a combinator curve.
- **Manual control:** Adjusting shaft speed and propeller pitch individually without predefined settings.

Comparisons were made between simulations with and without PBCF as models scale test data was not available. To achieve the same ships speed the simulation with PBCF included utilised the thrust controller from the parametric study. The following table show the froude-scaled ships speeds and pitches for the four testing conditions.

Table 7.1: Pitching testing conditions for the propeller blade.

Conditions	V_M [m/s]	α at hub [$^\circ$]
1	1.91	48.8
2	2.06	52.3
3	2.17	52.9
4	2.13	53.4

On figure 7.3 the percentage point changes between the propeller with and without PBCF and the propeller without PBCF from the design point at different pitches are displayed. From this it is evident that the PBCF not only increase the efficiency at all settings, but find a larger or equal gain outside the design point. The overall greatest efficiency is still at the design point after the PBCF are installed.

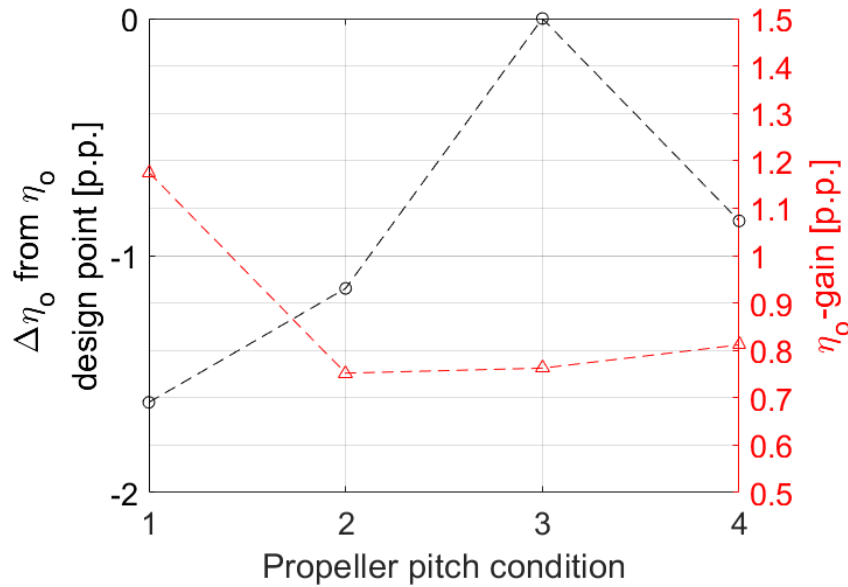


Figure 7.3: Percentage point change for efficiency from design point (condition 3) with PBCF on the left y-axis and between the propeller with and without PBCF on the right y-axis.

The variation in pitch between the four testing conditions are quite small, as it focused on the design area for this particular propeller. From a design perspective off-design effects and in particular the break-even point for efficiency gain with the PBCF would be desirable knowledge to obtain and therefor a more expanded range of design pitches is investigated. The new range increase with increments of 0.1 from 0.7 to 1.5 P/D with correspondingly increasing ships speeds, all supplied by MAN Energy Solutions Frederikshavn. It should be noted that the propeller is only designed to operate in the 0.7 to 1.2 range, so results outside of this are purely theoretical.

From figure 7.4 it is evident that there is an increasingly positive influence from the PBCF on the propeller. Below a P/D value of 0.9 the gain becomes negative, meaning the PBCF reduces the efficiency. In the theoretical area, $P/D < 1.2$, the efficiency gain initially decreases and then increases again which does not align with what was expected.

Another interesting observation is that propeller pitch condition 1 which resembles that of P/D 1.0, but has a slightly lower pitch and ships speed, find approximately 0.6 p.p. more efficiency gain. This gain is also the largest observed increase in the report.

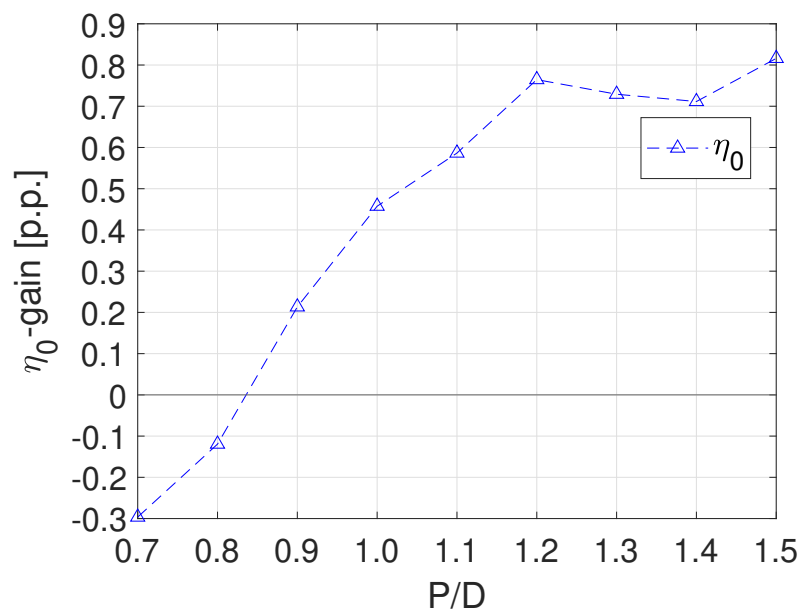


Figure 7.4: Percentage point change for K_T , K_Q and η_0 between a propeller with and without the PBCF.

7.1.1 Individually Varied Pitching

The previous subsection focused on the efficiency gains found at different specified pitch and velocity points and the design condition. By separating the pitch and velocity the varying pitch operational mode can be investigated. This was done independently of the design condition for the propeller with increments of 0.1 for the P/D. Similarly to previous CPP-investigations the thrust controller was utilised. Pitching found the following percentage point gains:

Table 7.2: Percentage point gain for pitching at a fixed ships speed.

	<u>P/D</u>									
	0.7	0.8	0.9	1	1.1	1.2	1.3	1.4	1.5	
η_0 -gain [p.p.]	-24.31	-3.08	0.09	0.43	0.62	0.84	0.87	0.93	0.89	

From table 7.2 the same tendency found in figure 7.4 is present. However, the tendency differs for P/D-values above 1.2, where table 7.2 pitching the propeller found a peak at a P/D of 1.4 instead of 1.2 and 1.5. This suggests that the combination of pitch and velocity has to be tuned for each operational point reminiscent of a combinator curve operational mode.

Chapter 8

Full-scale Studies

The full-scale simulations in this chapter are performed in effort to demonstrate the stated efficiency gain factor of 2-3 between model and full-scale PBCF implementation and to identify and localise the often-mentioned, but rather undefined, scaling-effects found in the literature.

8.1 Simulation Flow & Mesh Parameters

The mesh generation method used in the full-scale simulations is generally the same as the method used in the model-simulations in section 3.2. In the full-scale mesh only the base-sizes, relative minimum and target sizes, and the prism-layer thickness have been altered to ensure satisfying resolution of the domain, especially with emphasis on the y^+ -values of the boundary layer. Ideally, the y^+ -values should be below 6 to properly estimate the physical forces acting on the geometry which are the essential parameters of the simulations. The flow parameters are identical to those of the model-scale simulations with exception of the ships speed and the angular velocity that are not Froude-scaled with the scaling factor λ - these are listed in table 8.1.

Table 8.1: Froude-scaled parameters used in the full-scale simulations.

Parameter	Value	Units
Velocity, \mathbf{U}	(-10.88, 0, 0)	m/s
Angular Velocity, n	2.43	rps

Propeller Blade y^+ -distribution

The propeller blade y^+ -distribution on the suction and pressure side is examined to ensure the boundary layer is properly resolved. The distribution is as follow:

Table 8.2: Distribution of y^+ on the propeller suction and pressure side. The pressure side has 178,756 surface cells and the suction side has 182,047.

Interval	Share of Cells [%]	
	Pressure Side	Suction Side
$0 < y^+ \leq 3$	47.48	43.64
$3 < y^+ \leq 6$	50.81	53.94
$6 < y^+$	1.71	2.41
Total	100.00	99.99

Comparison of Data-sheet Calculation and Numerical Simulation

Full-scale data is not available for the propeller used in this full-scale study. However, full-scale calculations from the propeller's data-sheet was provided by MAN Energy Solutions so this will serve as reference for comparison.

The calculations are performed with empirical and theoretical factors to account for the effect of the hull on the wake flowing into the propeller and thus the propeller performance. The efficiency stated is no longer η_0 but η_B (behind the hull). In addition, the draft and trim are potentially different to the simulations. The comparison is done to judge whether the full-scale simulations are in the 'ballpark' and to avoid mistakes in the settings, and additionally to underline the complex nature of propellers and the general uncertainties involved. The differences between K_Q , K_T and η_0 from the data-sheet to the simulation are provided in table 8.3:

Table 8.3: Differences in K_T , K_Q and η_0 between the data-sheet and the full-scale simulation. *Difference in η_B and η_0

ΔK_T [%]	ΔK_Q [%]	$\Delta \eta_0^*$ [%]
-8.11	0.28	-8.37

The differences between K_T and η_0 are larger than the general rule of thumb of $\pm 5\%$ in a typical validation - *which this is not* - but this is not surprising due to the nature of the calculations as mentioned above.

The full-scale simulation is with the original hub from MAN Energy Solutions and it is using the γ - $Re_{\theta t}$ -transition model. The γ -transition model could have been used as their performance in full-scale was near identical, it was found.

8.2 Full-scale Efficiency Gain

In this full-scale study 3 simulations were conducted: A simulation of the original hub (OH) which was also used in the comparison, the new hub (NH) and the new hub with PBCF (NH w/ PBCF). A thrust controller similar to the one used in the model-scale studies were used to keep the thrust constant at the value of the original hub by changing the angular velocity. The open water efficiency gains between the 3 simulations are listed in table 8.4:

Table 8.4: The respective efficiency gains between the 3 full-scale simulations, the model-scale simulations and the factor of gain between model- and full-scale simulations. FS and MS are short for full-scale and model-scale, respectively. The model-scale gains are from sections 5.1 and 6.5.

	NH vs. OH	NH w/ PBCF vs. NH	NH w/ PBCF vs. OH
$\Delta\eta_0$ FS [p.p.]	0.39	1.00	1.39
$\Delta\eta_0$ MS [p.p.]	0.11	0.76	0.87
MS-FS factor [-]	3.55	1.32	1.60

The column highlighted in bold is for the same scenarios as the small-scale studies are conducted, and from this it is evident that the efficiency gain is greater in the full-scale simulation compared to the model-scale, but it is only by a factor of 1.32 and not 2-3 as the literature suggested. The factor from the literature is based on the relative percentages, which this report cannot state together with percentage points due to confidentiality, but the conclusion is still valid.

The gain in open water efficiencies purely as a results of upscaling from model- to full-scale are listed:

Table 8.5: The open water efficiency gain as function of upscaling the model-scale to full-scale. The three full-scale configurations are compared to their own model-scale counterpart.

	<u>OH</u>	<u>NH</u>	<u>NH w/ PBCF</u>
$\Delta\eta_0$ [p.p.]	1.18	1.45	1.71

The large and increasing gains shown in table 8.5 suggest that the full-scale are better at resolving the flow better, which could be due to the relatively slower boundary layer velocity.

8.3 Full-scale Observations and Effects

In this section the 3 full-scale simulations' vorticity profiles are compared to their respective model-scale counterpart to uncover the scaling effects on the vorticity and general flow. The left hand side illustrations are from the full-scale simulations and those on the right hand side from the model-scale simulations.

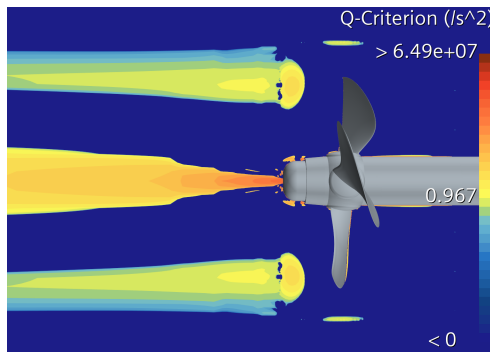


Figure 8.1: Original hub FS.

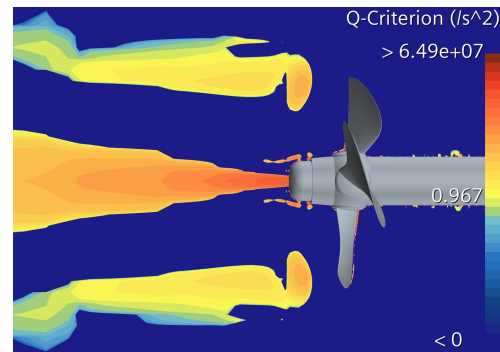


Figure 8.2: Original hub MS.

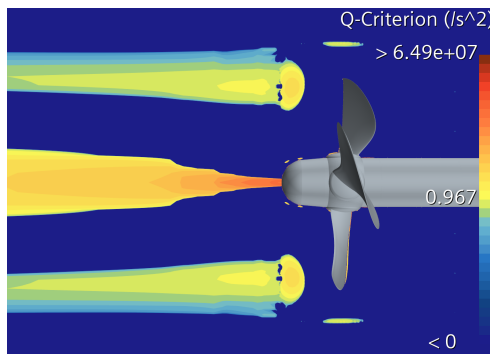


Figure 8.3: New hub FS.

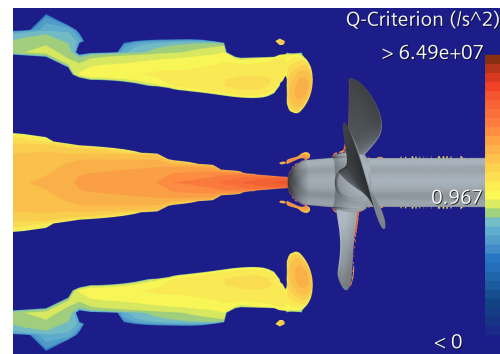


Figure 8.4: New hub MS.

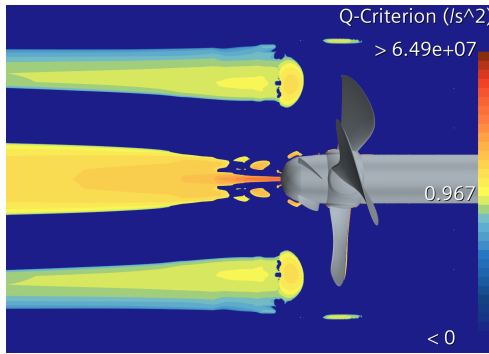


Figure 8.5: New hub with PBCF, FS.

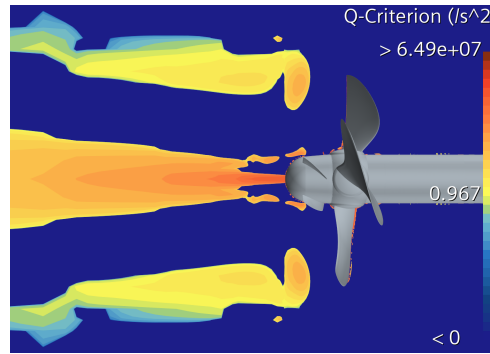


Figure 8.6: New hub with PBCF, MS.

The apparent differences in vorticity between full-scale and model-scale are as follow:

- The hub vortices in FS are narrower and less intense compared to MS, which is advantageous in terms of efficiency, according to literature.
- The full-scale simulations contain information about the tip vortices directly above the tips which the model scale simulations do not capture.
- The shed tip vortices moving downstream in FS are more orderly layered in the radial direction, whereas the MS layers are warped.
- The satellite vortices in FS are less pronounced and more scattered downstream compared to the secondary vortices in MS which are larger, more intense and more directly attached to the hub.

The wake slices for the FS were also compared to those of the MS, but no distinctive differences were observed. Small patches of vorticity was found in between the tip vortices, which is likely to be a consequence of the different shape of the tip vortices apparent in the sideways slices. Froude-scaling is typically the scaling method of choice in maritime applications, as this scales the waves properly as the waves are the dominant drag inducers. This could suggest that favouring the waves the information of the inertia is not as accurate as it would be with Reynolds-scaling for instance, giving rise to the shown overestimation of vorticity compared to the FS simulations.

Chapter 9

Discussion

This following chapter discusses and evaluates the results attained in the previous chapters 6, 7 and 8.

In the parametric study the graphical influences to the flow which were specifically parameter dependent were difficult to distinguish due to the complex nature of a flow. However general overlapping tendencies could be found. In open water the inclusion of the PBCF illustrate that diffusing the hub vortex, thereby weakening the core of the hub vortex, produces an increase in efficiency gain. In the pitch variations a limit of this is evident at pitch 1, where the efficiency gain is less than pitch 3, despite graphically having a weaker hub vortex. This could be due to the the PBCF at lower pitching act more as a walls. Consequently, this alludes to the correlation between the hub vortex and the efficiency, where focusing only on alleviating the hub vortex results in a lower efficiency gain.

The rudder implementations had the same efficiency gain tendencies as were found in open water, but the correlation with the hub vortex presents slightly different, due to the upstream effects from the rudder. In particular the hub vortex on the wake slices with the highest efficiency gain has the smallest area, in contrast to the open water wake slices. Similarly to the open water pitch 1 is an exception, as it presents more cohesion on the wake plot, despite finding a lower efficiency.

Relating the weakening of the hub vortex to the efficiency gain through visualisation is challenging as 'weakening' is a combination of the change in size and intensity of the vortex and the interaction between the vortex and the geometry is an unknown in terms of efficiency. However, the total effect of the combinations are, of course, evident in the efficiency calculations.

A limitation of the visual representation is naturally occurring as a 3-dimensional domain is shown in 2-dimensional slices. The sideways slice is spanning the x-y-plane for $z=0$ and movements in the z-direction would give visually different figures. In addition the wake slices are placed $0.74 D_p$ downstream of the propeller and this was chosen rather arbitrary at the middle of the rudder meaning the impact of this choice is unknown. In both cases the comparisons are done in the same places and are valid within the mentioned limitations.

The efficiency gain between open water and the rudder implementation has a non-linear correlation even though they are sharing similar tendencies. Therefore, it can be argued that investigating the PBCF for its general tendencies can be done as an open water investigation, but the actual efficiency gain would have to be found through the rudder implementation.

The ranges chosen for the parameter variations were based on either software-, geometry limitations or literature study recommendations. Global peaks were found in the case of PBCF pitch and height but not for rake and chord length, which should be considered when evaluating the results. Within the examined ranges parameter interaction was found to adversely effecting efficiency gain when making the 'Best Parameter Values' PBCF, see table 6.4, meaning the best PBCF was C7, but it is uncertain if that would be the case if the ranges for rake and chord length were extended. A new global optimum for the 4 parameters would likely have been found.

Results gained in the controllable pitch section for the extended range of P/D both with a varying pitch and ships speed and fixed ships speed find the same tendencies except for the theoretical values between P/D of 1.2 and 1.5. It is assumed as the correlation between the varying pitch and ships speed changes between P/D 1.2 and 1.5 that this may be the reasoning behind the behaviour. Thereby illustrating the importance between pitch and ships speed in that operational mode.

In the case of the full-scale simulations the same uncertainties applying to model-scale apply to these simulation. In addition, literature regarding full-scale propeller simulations is sparse and no general recipe was found. As stated in chapter 8 a validation could not be performed, instead a comparison was made with data-sheet calculations from MAN Energy Solutions Frederikshavn. The mesh philosophy was based around the one used in the model-scale simulations and through the iterative process the final mesh was deemed mesh independent, making the authors convinced a quality mesh was obtained.

Throughout the report η_0 has been utilised as a major comparison point but has been used for conditions differing from those of the definition, as the shaft, PBCF and rudder are included.

Froude-scaling have been used throughout the report as this is the main method of scaling applied in marine-studies but Reynolds-scaling is also a way of scaling the simulations. The effect of this choice is an unknown, especially with wave drag and vorticity in mind when comparing model- and full-scale. As a final remark it is reminded that the simulation flow conditions are much simplified compared to the flow a propeller would experience out at sea, where waves, current and the ship itself all influence the inflow to the propeller. Once again, the comparisons are made under the same assumption and limitations and are therefore still valid.

Chapter 10

Conclusion

In this section the three research questions stated in the problem statement are concluded upon on in the same order:

Quantify and if possible qualitatively identify the influence of the four PBCF parameters chord length, height, pitch and rake on the hub vortex through Q-criterion representations and open water efficiency calculations.

It is concluded that all PBCF parameters have a positive influence on the open water efficiency, with the exception of pitch which have an adverse effect in open water pitch condition 7 equivalent to 62° .

The strongest trend is seen in the case of the **chord length** where it is concluded that condition 7, 9% c/D, is the best and an even longer chord would likely have performed better.

The effect of the **height** of the PBCF plateau around 0.6 p.p. at open water condition 3-7, equivalent to 29-33% of the propeller diameter, and peaks at condition 5 in the rudder case.

The optimum **pitch** is found at condition 2-3, $42-46^\circ$, with very strong parabolic trends clearly indicating the maxima have been located. Adverse effects are seen for open water condition 7 (62°).

Rake is concluded to contribute 0.5-0.6 p.p. across the range in open water and 0.4-0.5 in the rudder case.

The optimum PBCF constructed based on the best results from the parameter study improved the efficiency with 0.65 and 0.51 p.p in the open water and rudder cases which is significantly lower than the 0.76 and 0.60 p.p. of the optimum chord length. From this, it concluded that parameter interaction is occurring having adverse effect on the efficiency.

The influences identified on the Q-criterion plots were the same for almost all variations. The hub vortex became narrower immediately after the hub and diffused from hereon and downstream, thus overall weakening the vortex giving an efficiency gain. This is in line with statements from the literature.

Utilising the most efficient PBCF elaborate on the open water efficiency effect of introducing a PBCF on a CPP.

For the CPP propeller's actual operational range it is concluded that the PBCF do increase the open water efficiency in all 4 conditions and the maximum increase is at condition 1, but the most efficient overall combination is found for condition 3 i.e the design point.

When examining a larger span of P/D for the CPP it is concluded that a 'break even' point lies between $0.8 < P/D < 0.9$ from which a lower P/D yields a negative open water efficiency gain with the implementation of the PBCF. After $P/D=3$ the gain rises rapidly and settles on 0.7-0.8 p.p. from $1.2 < P/D < 1.5$.

Lastly, evaluate the difference between model- and full-scale CFD simulations with and without PBCF, focusing on efficiency gains and vortex structures.

It is concluded that the open water efficiency and the efficiency gain is greater in full-scale as the new hub is 1.45 p.p. more efficient in full-scale and it gains 1.32 times more from the PBCF compared to model-scale. The effect of the new hub is 3.55 times greater in full-scale compared to model-scale, which is the largest relative increase of all.

As for the vortex structure in full-scale 4 distinctive observations are made compared to the model-scale simulations:

- Narrower and less intense hub vortex.
- Tip vortices are observed directly above the propeller blades.
- Orderly radial layered shed tip vortices.
- Less pronounced and more scattered satellite vortices.

It is concluded that the model-scale simulations overestimate the vorticity in comparison to the full-scale simulation which' open water efficiency estimations are closer to the actual propeller efficiency.

Chapter 11

Future Work

Further work in relation to this report could consist of separating lift and drag forces. By doing so it can be assessed whether the PBCF contribute to the thrust through additional lift or by decreasing drag by diffusing the hub vortex. This could also lead into a study of the forces in relation to different PBCF parameters or how the flow interact with the PBCF through evaluation of velocity vectors.

From the parametric study it was found that the open water and rudder implementation simulations with the PBCF inclusion did not have a linear correlation in relation to the efficiency gain. Investigating the effects of the rudder could therefore lead to other design choices for the PBCF. Furthermore, this could be extended to alterations of the design and position of the rudder in order to find the best interaction points through flow, force or pressure distribution investigations.

The efficiency of the propeller is highly effected by the inflow profile, and in this report a plug flow with no pressure gradient was used. Modelling the flow to resemble that of an actual wake would give a more in-depth understanding of how the PBCF works and interacts with the propeller. This could also include a full ship geometry.

Most studies on the PBCF altered the parameters for the PBCF in relation to one propeller similarly to this report. Expanding the investigations to include more propellers with similar designs could find general trends that would allow a standardised design process i.e a number-in-number-out calculator.

Cavitation and noise are important things to consider when designing propeller blades, and to the best of the authors knowledge this has not been investigated in relation to the PBCF.

Finally, the results from this report were obtained using a thrust controller keeping the ships speed constant throughout the individual studies.

An alternative is a self-propulsion simulation where both the thrust and revolutions are set free constrained by the ship's resistance thus reaching an equilibrium. This could yield results with greater ships speed and better efficiency simultaneously.

Bibliography

- Cai et al., 2013.** Hao-Peng Cai, M A Cheng, Chen Ke, Qian Zheng-Fang and Chen-Jun Yang. *An Integrative Design Method of Propeller and PBCF(Propeller Boss Cap Fins) **. 2013.
- Celik et al., 7 2008.** Ismail B. Celik, Urmila Ghia, Patrick J. Roache, Christopher J. Freitas, Hugh Coleman and Peter E. Raad. *Procedure for estimation and reporting of uncertainty due to discretization in CFD applications*. Journal of Fluids Engineering, Transactions of the ASME, 130(7), 0780011–0780014, 2008. ISSN 00982202. doi: 10.1115/1.2960953/444689. URL http://asmedigitalcollection.asme.org/fluidsengineering/article-pdf/130/7/078001/5491455/078001_1.pdf.
- Cengel et al., 2016.** Y.A Cengel, John Cimbala and Robert H. Turner. *Fundamentals of Thermal Fluid Sciences*. 2016. ISBN 978-9-814-72095-3.
- Dam and Jørgensen, 2022.** Patricia Dam and Mikkel Jørgensen. *Multi-variable Optimisation Study of Propeller Boss Cap Fins*, 2022. URL https://projekter.aau.dk/projekter/files/419122327/Optimum_Design_of_Propeller_Boss_Cap_Fins_PBCF_by_Model_Scale_Numerical_Evaluation.pdf.
- Dang et al., 2012.** Jie Dang, Guoxiang Dong and Hao Chen. *An exploratory study on the working principles of energy saving devices (ESDs) - PIV, CFD investigations and esd design guidelines*. Proceedings of the International Conference on Offshore Mechanics and Arctic Engineering - OMAE, 5, 25–34, 2012. doi: 10.1115/OMAE2012-83053. URL https://www.researchgate.net/publication/267606561_An_Exploratory_Study_on_the_Working_Principles_of_Energy_Saving_Devices_ESDs_PIV_CFD_Investigations_and_ESD_Design_Guidelines.
- Gao et al., 3 2019.** Zhuwei Gao, Juan Wang, Jiangyun Wang, Yu Mao and Yaodong Wei. *Analysis of the effect of vortex on the flow field of a cylindrical cyclone separator*.

- Separation and Purification Technology, 211, 438–447, 2019. ISSN 13835866. doi: 10.1016/j.seppur.2018.08.024.
- Hansen et al., 2011.** Hans Richard Hansen, Mr Tom Dinham-Peren and Mr Takeo Nojiri. *Model and Full Scale Evaluation of a 'Propeller Boss Cap Fins' Device Fitted to an Aframax Tanker*. 2011.
- International Marine Organisation.** International Marine Organisation. <https://www.imo.org/en/OurWork/Environment/Pages/GHG-Emissions.aspx>.
- Kawamura et al., 2013.** Takafumi Kawamura, Kazuyuki Ouchi and Susumu Takeuchi. *Model and full scale CFD analysis of propeller boss cap fins (PBCF)*. 2013.
- Kellett et al., 7 2013.** Paula Kellett, Osman Turan and Atilla Incecik. *A study of numerical ship underwater noise prediction*. Ocean Engineering, 66, 113–120, 2013. ISSN 0029-8018. doi: 10.1016/J.OCEANENG.2013.04.006.
- Kok.** J C Kok. *Resolving the dependence on free-stream values for the k-omega turbulence model*.
- Lim et al., 6 2014.** Sang Seop Lim, Tae Won Kim, Dong Myung Lee, Chung Gil Kang and Soo Young Kim. *Parametric study of propeller boss cap fins for container ships*. International Journal of Naval Architecture and Ocean Engineering, 6(2), 187–205, 2014. ISSN 2092-6782. doi: 10.2478/IJNAOE-2013-0172.
- Menter, 1994.** F. R. Menter. *Two-equation eddy-viscosity turbulence models for engineering applications*. AIAA Journal, 32(8), 1598–1605, 1994. ISSN 00011452. doi: 10.2514/3.12149.
- Mizzi et al., 2017.** Kurt Mizzi, Yigit Kemal Demirel, Charlotte Banks, Osman Turan, Panagiotis Kaklis and Mehmet Atlar. *Design optimisation of Propeller Boss Cap Fins for enhanced propeller performance*. Physics Procedia, 62, 210–222, 2017. doi: 10.1016/j.apor.2016.12.006. URL <http://creativecommons.org/licenses/by/4.0/>.
- Nojiri et al., 2011.** Takeo Nojiri, Norio Ishii and Hisashi Kai. *Energy Saving Technology of PBCF (Propeller Boss Cap Fins) and its Evolution*. Journal of The Japan Institute of Marine Engineering, 46(3), 350–358, 2011. ISSN 1346-1427. doi: 10.5988/JIME.46.350. URL https://www.researchgate.net/publication/287859064_Energy_Saving_Technology_of_PBCF_Propeller_Boss_Cap_Fins_and_its_Evolution.
- Ouchi et al., 1988.** K. Ouchi, M. Ogura, Y. Kono, H. Orito, T. Shiotsu, M. Tamashima and H. Koizuka. *A Research and Development of PBCF(Propeller*

Boss Cap Fins). Journal of the Society of Naval Architects of Japan,, 168(2), 66–68, 1988. ISSN 0009-2347. doi: 10.1021/cen-v032n039.p3814.

Ouchi et al., 1989. Kazuyuki. Ouchi, Masahiro. Tamashima and Samebo. Japan. *Research and development of PBCF. New and practical device to enhance propeller efficiency.* page 10, 1989.

Rosenvinge and Sandland, 2021. Christian K Rosenvinge and Marcus Pless Sandland. *Optimum Design of Propeller Boss Cap Fins (PBCF) by Model Scale Numerical Evaluation.* (May), 2021.

Versteeg and Malalasekera, 2007. H K. Versteeg and W. Malalasekera. *An Introduction to COMPUTATIONAL FLUID DYNAMICS The Finite Volume Method.* Pearson Education Limited, 2. ed. edition, 2007. ISBN 978-0-13-127498-3.

Appendix A

Mesh & Residuals Analysis

Following graphs display the residual, thrust and torques progressions during a simulation.

A.1 Open Water

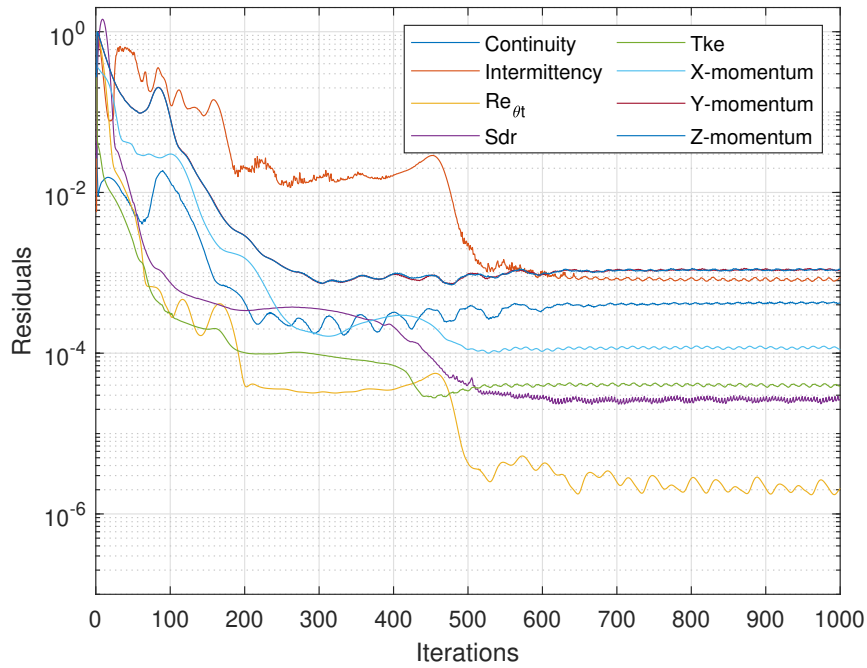


Figure A.1: Residual plot for the X-, Y- and Z-momentum, continuity, intermittency, momentum thickness turbulent Reynolds number, specific dissipation rate and turbulent kinetic energy.

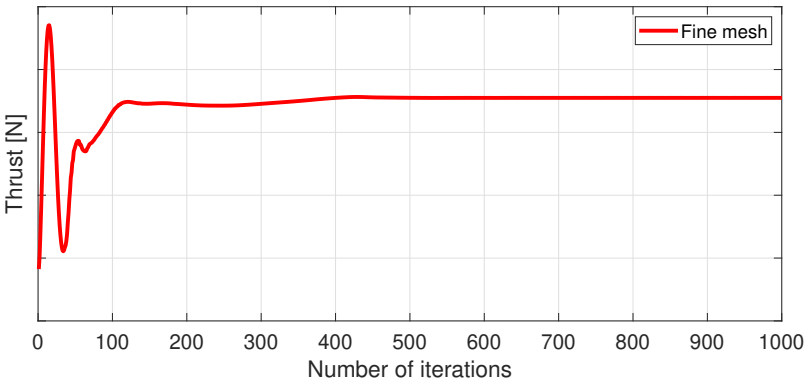


Figure A.2: Thrust progression from iteration 1 to 1000.

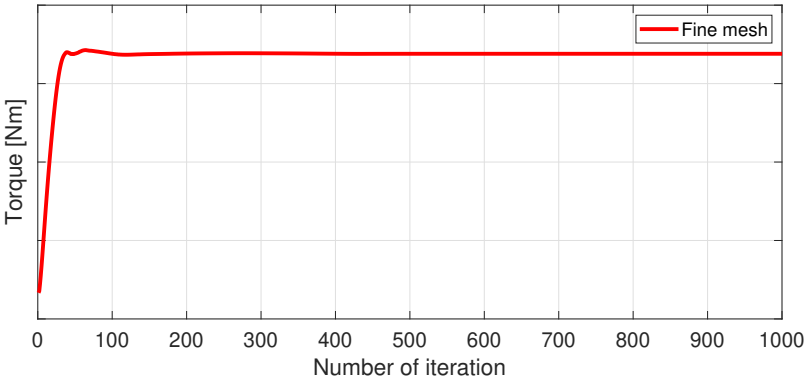


Figure A.3: Torque progression from iteration 1 to 1000.



Figure A.4: Mesh visualisation of the cell quality below values of 0.3.



Figure A.5: Mesh visualisation of intermittency residual below the values of $-1.0 \cdot 10^{-5}$ and above $1.0 \cdot 10^{-5}$.

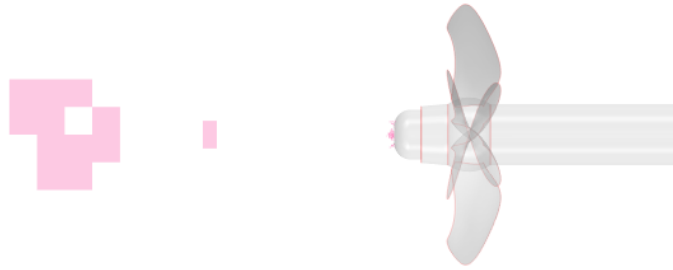


Figure A.6: Mesh visualisation of mass imbalance (continuity) residual below the values of $-1.0 \cdot 10^{-6}$ and above $1.0 \cdot 10^{-6}$.



Figure A.7: Mesh visualisation of X-, Y- and Z-momentum residuals below the values of $-1.0 \cdot 10^{-5}$ and above $1.0 \cdot 10^{-5}$.

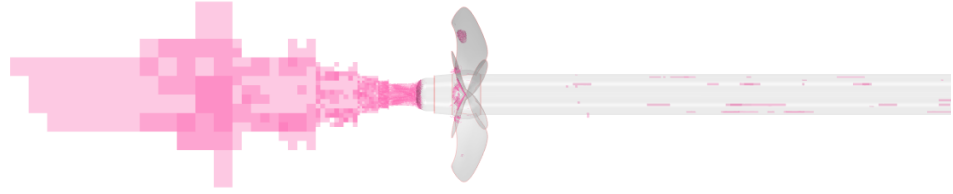


Figure A.8: Mesh visualisation of the specific dissipation rate below the values of $-1.0 \cdot 10^{-3}$ and above $1.0 \cdot 10^{-3}$.

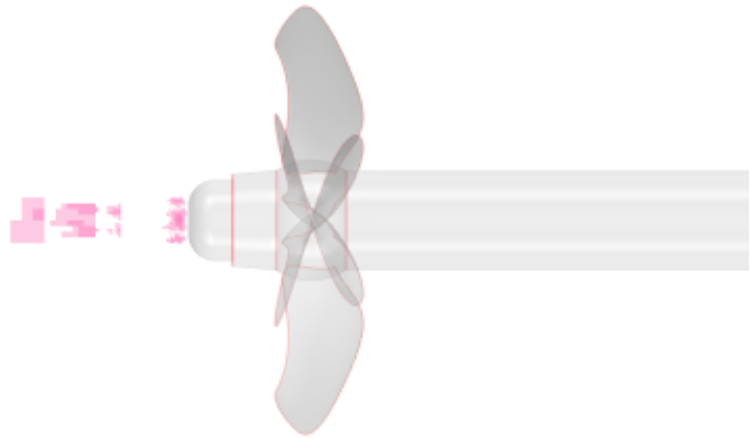


Figure A.9: Mesh visualisation of the turbulent kinetic energy below the values of $-1.0 \cdot 10^{-6}$ and above $1.0 \cdot 10^{-6}$.

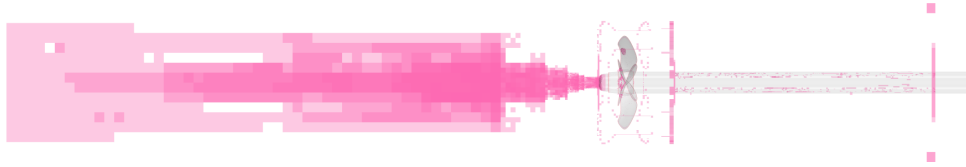


Figure A.10: Mesh visualisation of all the different residuals from the residual plot on figure A.1.

The figures A.4, A.5, A.6, A.7, A.8, A.9 and A.10 above were aids used in the refinement process with these being the final visualisations.

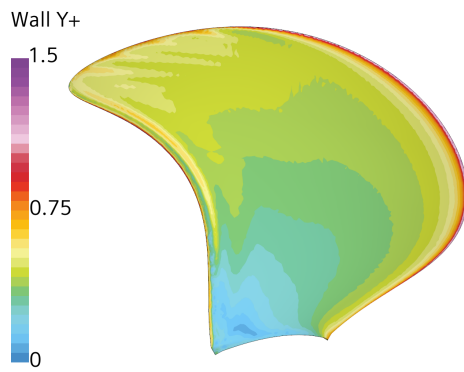


Figure A.11: Pressure side blade with y^+ illustration for a fine mesh.

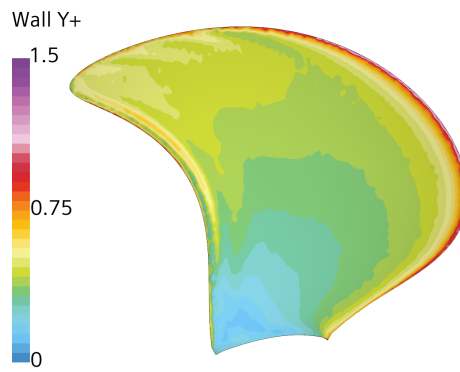


Figure A.12: Pressure side blade with y^+ illustration for a medium mesh.

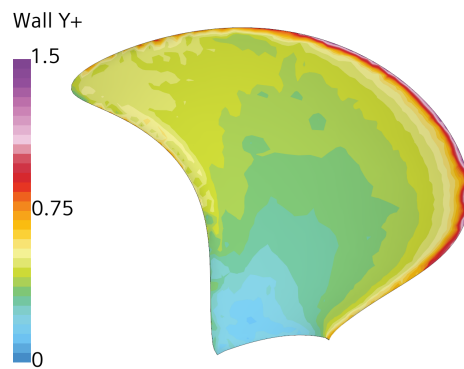


Figure A.13: Pressure side blade with y^+ illustration for a coarse mesh.

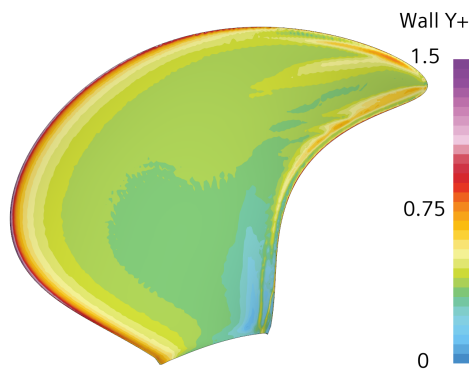


Figure A.14: Pressure side blade with y^+ illustration for a fine mesh.

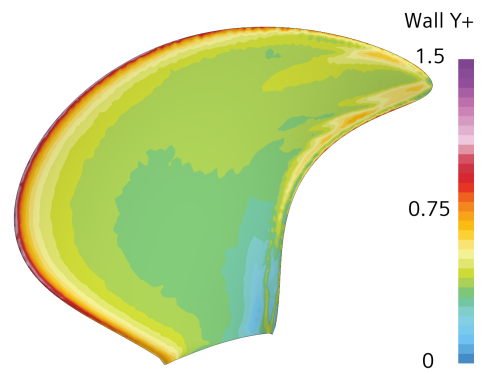


Figure A.15: Pressure side blade with y^+ illustration for a medium mesh.

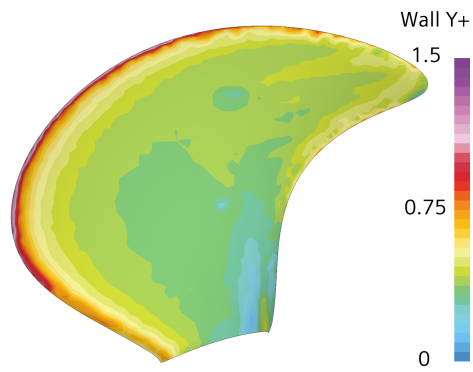


Figure A.16: Pressure side blade with y^+ illustration for a coarse mesh.

A.2 With Rudder

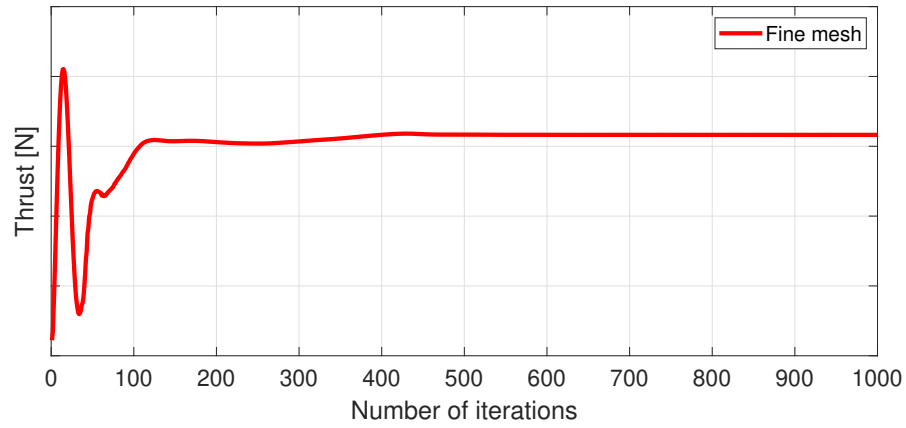


Figure A.17: Thrust progression from iteration 1 to 1000.

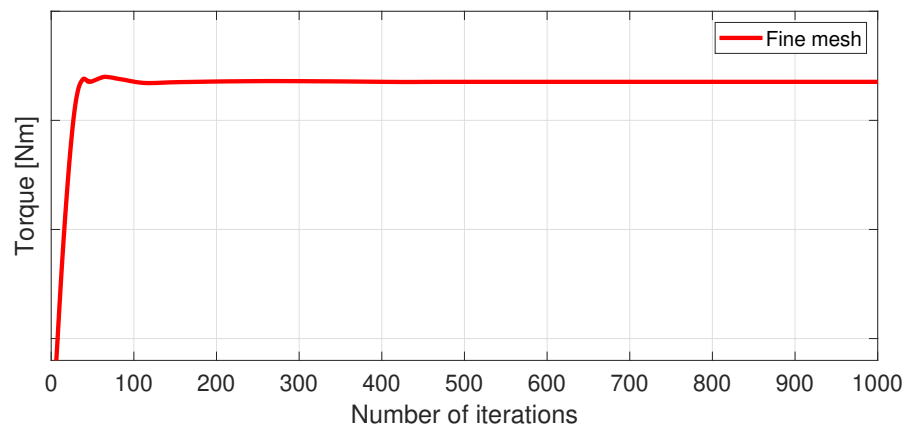


Figure A.18: Torque progression from iteration 1 to 1000.

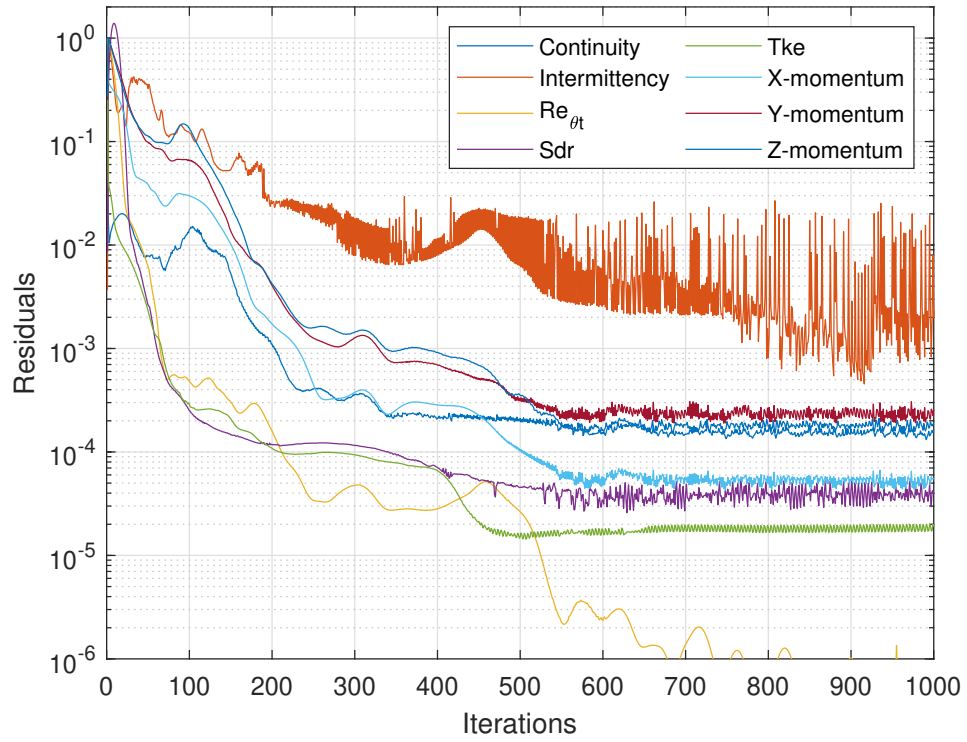


Figure A.19: Residual plot for the X-, Y- and Z-momentum, continuity, intermittency, momentum thickness Reynolds number, specific dissipation rate and turbulent kinetic energy.



Figure A.20: Mesh visualisation of the cell quality below the values of 0.3.



Figure A.21: Mesh visualisation of intermittency residual below the values of $-1.0 \cdot 10^{-5}$ and above $1.0 \cdot 10^{-5}$.



Figure A.22: Mesh visualisation of mass imbalance (continuity) residual below the values of $-1.0 \cdot 10^{-6}$ and above $1.0 \cdot 10^{-6}$.



Figure A.23: Mesh visualisation of X-, Y- and Z-momentum residuals below the values of $-1.0 \cdot 10^{-5}$ and above $1.0 \cdot 10^{-5}$.



Figure A.24: Mesh visualisation of the specific dissipation rate below the values of -0.01 and above 0.01 .



Figure A.25: Mesh visualisation of the turbulent kinetic energy below the values of $-1.0 \cdot 10^{-6}$ and above $1.0 \cdot 10^{-6}$.

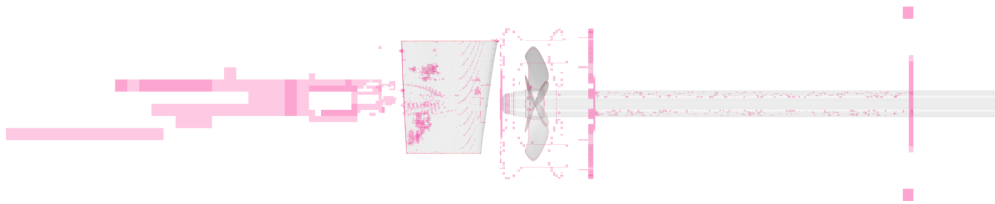


Figure A.26: Mesh visualisation of all the different residuals from the residual plot on figure A.19.

The figures A.20, A.21, A.22, A.23, A.24, A.25 and A.26 above were aids used in the refinement process with these being the final visualisations.

Appendix B

PBCF geometry

To visualise the difference between the PBCF geometries, the extremes and design case are presented here.

Chord Length

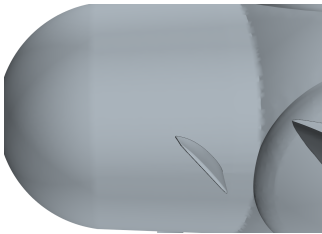


Figure B.1: Chord length of 3% c/D .

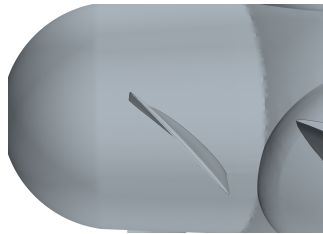


Figure B.2: Chord length of 6% c/D .

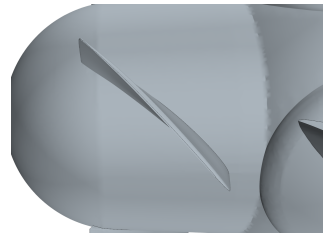


Figure B.3: Chord length of 9% c/D .

Height

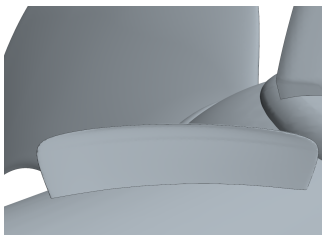


Figure B.4: PBCF height of 27% propeller radius.

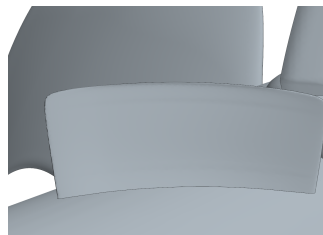


Figure B.5: PBCF height of 30% propeller radius.

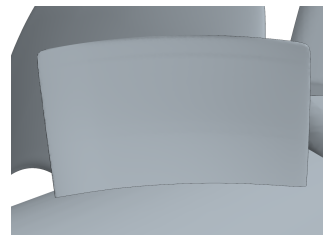
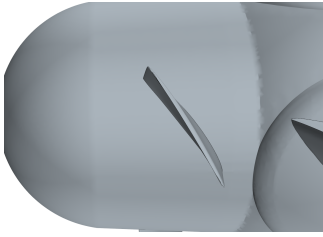
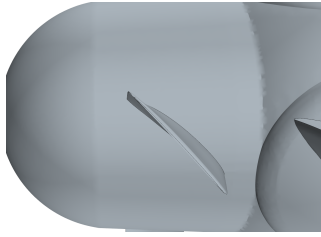
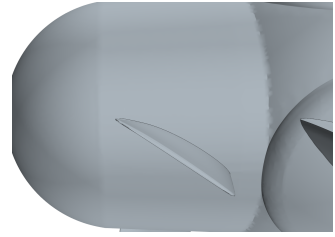
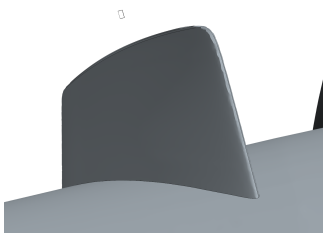
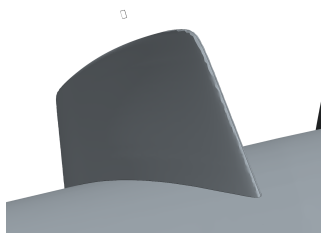
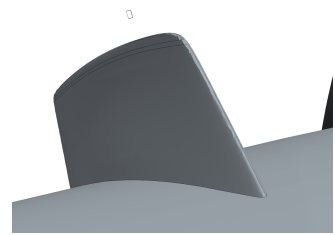


Figure B.6: PBCF height of 33% propeller radius.

Pitch**Figure B.7:** Pitch of 38° .**Figure B.8:** Pitch of 50° .**Figure B.9:** Pitch of 62° .**Rake****Figure B.10:** Rake of 0° .**Figure B.11:** Rake of 6° .**Figure B.12:** Rake of 12° .